# Laser-induced ultrasound for the detection of buried micro- and nano-structures

Vanessa Verrina

PhD Thesis, University of Amsterdam, April 2021

*Laser-induced ultrasound for the detection of buried micro- and nano-structures*

Vanessa Verrina

ISBN: 978-94-92323-51-4

Cover design: Mariella Spadafora

This thesis is printed on 100% recycled paper.




UNIVERSITEIT VAN AMSTERDAM



The work described in this thesis was carried out at the Advanced Research Centre for Nanolithography (ARCNL), a public-private partnership between the University of Amsterdam (UvA), the Vrije Universiteit Amsterdam (VU), the Netherlands Organisation for Scientific Research (NWO) and the semiconductor equipment manufacturer ASML.

# Laser-induced ultrasound for the detection of buried micro- and nano-structures

## Academisch Proefschrift

ter verkrijging van de graad van doctor

aan de Universiteit van Amsterdam

op gezag van de Rector Magnificus

prof. dr. ir. K.I.J. Maex

ten overstaan van een door het College voor Promoties

ingestelde commissie,

in het openbaar te verdedigen

op dinsdag 6 april 2021, te 15:00 uur

door

Vanessa Verrina

geboren te Cosenza, Italië

# Promotiecommissie

## Promotor

| | |
|---|---|
| prof. dr. P.C.M. Planken | Universiteit van Amsterdam |

## Co-Promotor

| | |
|---|---|
| dr. S.M. Witte | Vrije Universiteit Amsterdam |

## Overige leden

| | |
|---|---|
| prof. dr. J.W.M. Frenken | Universiteit van Amsterdam |
| prof. dr. A.F. Koenderink | Universiteit van Amsterdam |
| prof. dr. J. Gómez Rivas | Technische Universiteit Eindhoven |
| dr. N.J. van Druten | Universiteit van Amsterdam |
| dr. S.F. Pereira | TU Delft |

Faculteit der Natuurwetenschappen, Wiskunde en Informatica

# Publications

This thesis is based on the following publications:

1 V. Verrina, S. Edward, H. Zhang, A. Antoncecchi, S. Witte and P.C.M. Planken, Role of scattering by surface roughness in the photoacoustic detection of hidden micro-structures, Appl. Optics (2020)

Presented in Chapter **4**.

2 V. Verrina, S. Edward, H. Zhang, S. Witte and P.C.M. Planken, Photoacoustic detection of low duty cycle gratings through optically opaque layers, Appl. Phys. Lett. 117, 051104 (2020)

Presented in Chapter **5**.

3 V. Verrina and G. de Haan, and P.C.M. Planken, Enhanced detection of laser induced-acoustic waves by Surface Plasmon Polaritons, Manuscript in preparation (2020)

Presented in Chapter **6**.

The author contributed to the following publications:

1 S. Edward, H. Zhang, I. Setija, V. Verrina, A. Antoncecchi, S. Witte, and P. Planken, Detection of Hidden Gratings through Multilayer Nanostructures Using Light and Sound, Phys. Rev. Applied 14, 014015 (2020)

2 A. Antoncecchi, H. Zhang, S. Edward, V. Verrina, P. C. M. Planken, and S. Witte, High-resolution microscopy through optically opaque media using ultrafast photoacoustics, Opt. Express 28, 33937-33947 (2020)

# Contents

# 1 Introduction

Integrated circuits (ICs) are present in many electronic devices that we daily use, from computers to digital home appliances. An IC is a small wafer (or *chip*), made of semiconductor material, usually silicon (Si), that can hold from hundreds to billions of transistors, resistors, and capacitors. These extremely small electronic devices can perform calculations and store data. That is why their usage in all electronic equipment has revolutionised the field of electronics.

The semiconductor industry has been pushing the reduction of the size of the electronic components on a wafer since the mid-20th-century. By scaling down the elements of the circuits, more and more transistors could be packed on chips of the same size. Hence, smaller, faster an less expensive circuits can be obtained by integrating a large number of tiny transistors into a small chip.

The small size and low cost of ICs made it possible to make computers, mobile phones and other appliances that are now an essential part of modern society.

In 1965, Gordon Moore, founder of the company Intel, predicted that the number of transistors on a microchip would double every year [1]. Ten years later he changed his prediction stating that the number of transistors would double every two years [2], improving the chip's performance.

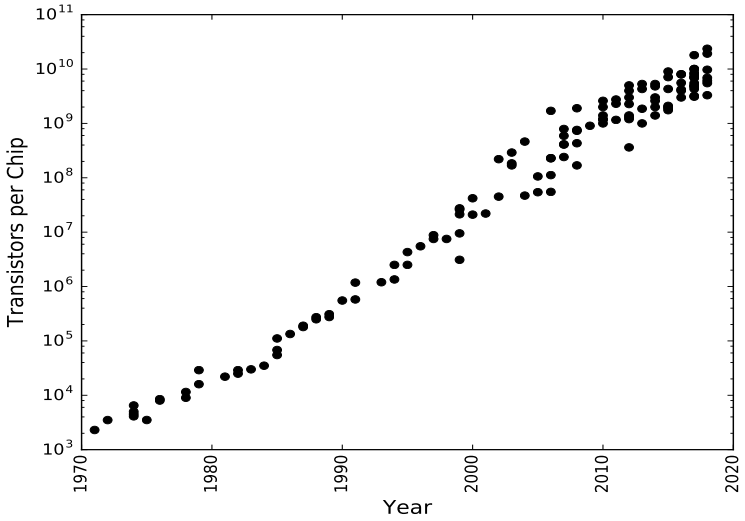


Figure 1.1: Count of the number of transistors per chip in the last 50 years for different processors. Each point represents the data of a particular company. The data are taken from [3].

Until now, Moore's prediction, known also as Moore's law, has been fulfilled, but increasing the numbers of elements on a microchip further is a challenge for the manufacturing industry.

The technique mostly used to imprint patterns on a silicon wafer is optical lithography [4, 5]. Optical lithography uses light to project the image of a mask onto a photosensitive material (photoresist) deposited on a substrate. Lithography is an important part of semiconductor manufacturing technology because it can fulfil the needs of the high volume production of microelectronic components. In particular, it makes it possible for the feature size to became smaller and smaller, increasing the density of transistors per unit area.

The typical lithography process (Fig. 1.2) starts with the deposition of a thin uniform layer of photoresist on the silicon substrate. The thin film is then exposed by illuminating it with a light pattern obtained by transmitting through or reflecting the light off a mask, also called a *reticle*. The mask contains the pattern of the structures that must be fabricated. Often, ultraviolet (UV) light is used as a light source. The optical beam "writes" the mask's pattern onto the resist, by changing the solubility of

the resist in the exposed area. In the next step, development, either the exposed part (positive tone resist) or the unexposed part (negative tone resist) is removed. In the last step, the pattern is transferred to the silicon wafer. There are three basic pattern transfer techniques: "wet" or "dry" etching, selective deposition and ion implantation [6–8]. Etching is one of the most common pattern transfer approaches. In Fig. 1.2 we show schematically the different steps of the lithographic process, where etching is used as pattern transfer technique.

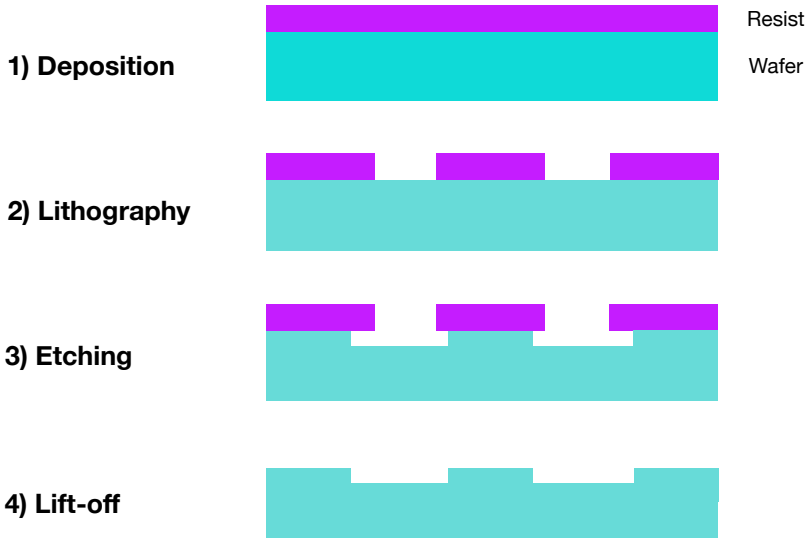


Figure 1.2: A simple schematic of a patterning process (Figure adapted from [9]). (1) Deposition of a uniform resist film on the wafer. (2) Lithography step to create a positive image of the pattern in the film. (3) Etch to transfer that pattern onto the wafer. (4) Lift-off to remove the resist layer.

The imaging performance of a lithography system is basically determined by the resolution or critical dimension (CD). CD is the smallest feature size the system can print on the photoresist. System resolution is determined by the Rayleigh criterion [10],

$$CD = \frac{k_1 \lambda}{NA}, \tag{1.1}$$

where $\lambda$ is the wavelength of the light used, NA is the numerical aperture of the system and $k_1$ is known as the process factor and includes all the process variables, such us photoresist, type of mask and its patterns. The process factor $k_1$ has reached its practical limit at $k_1 = 0.25$ [11]. According to Moore's law, CD shrinks by 30 % each generation. Improving resolution can therefore be done by using shorter light wavelengths, increasing the numerical aperture of the optical system and/or reducing $k_1$. The photolithography industry has been already working on reducing the light wavelength. It started with the 436 nm of a mercury vapour lamp, and went through 365 nm and 248 nm to today's deep ultraviolet (DUV) 193 nm [12]. Each step has brought significant advances in resolution. Moreover, for each wavelength, several steps were taken to reduce the numerical aperture as well. For example, the 193 nm systems were improved by *immersion lithography*. In this technique, the medium between the focusing lens and the wafer is a liquid, usually water. Water has a refractive index greater than one. Thus, immersion lithography allows to use lenses with numerical apertures greater than 1.0 ($\sim 1.3$) [13, 14].

By putting together all these parameters, a theoretical resolution limit of CD = 0.25 x 193 nm / 1.3 $\sim$ 37 nm can be achieved.

## 1.1 EUV Lithography

In order to make the continuation of Moore's law possible, a shorter wavelength must be used. This is where extreme ultraviolet (EUV) light comes into the picture. It has a wavelength of 13.5 nm and allows to print features about 14 times smaller than that of 193 nm, if we just consider the wavelength.

This wavelength requires engineering adjustments in different areas. First of all, as most materials absorb at this wavelength, traditional refractive optics cannot be used. Moreover, the processes need to happen in vacuum-based systems, and plasma sources have to be used to generate the EUV photons for lithography.

The state-of-the-art EUV emitting source used is a laser-produced tin (Sn) plasma. Sn droplets interact with high-intensity 10.6 µm wavelength pulses from a $CO_2$ laser [16]. The Sn atoms are ionised and a plasma is generated. The light produced contains wavelengths in a bandwidth around

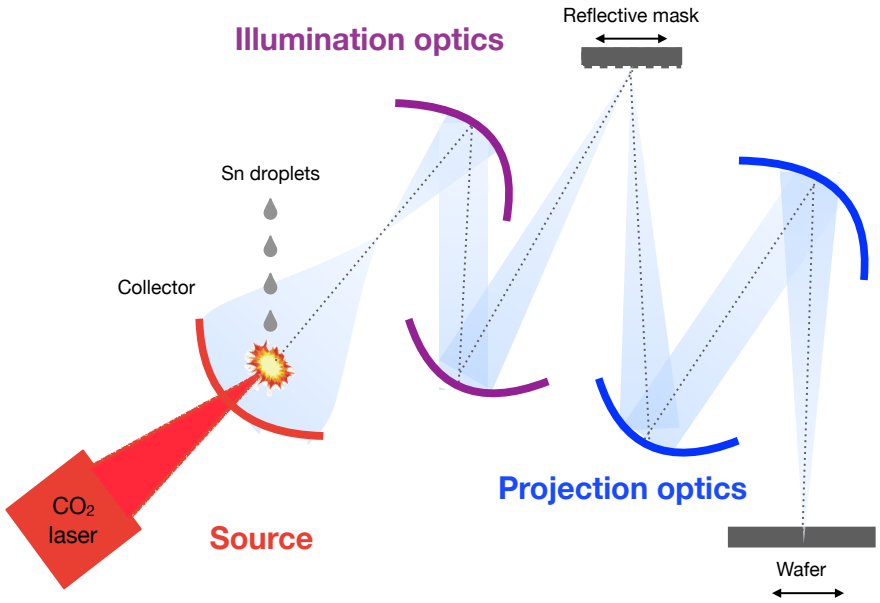


Figure 1.3: Simplified schematic of an EUV lithography machine. The source of EUV light is a plasma generated by a $CO_2$ laser hitting liquid Sn droplets. All the optics for collecting the light (collector), for sending the beam to the mask (illumination optics) and for transferring the patterned beam to the mask (projection optics) are made of Mo–Si multilayer mirrors, which can reflect up to 72 % of the EUV light [15].

13.5 nm.

To achieve a reflectivity of about 70 %, multilayer Mo-Si mirrors need to be used [17]. As shown in Fig. 1.3, the produced light is collected and reflected by numerous multilayer mirrors. After several reflections, this light illuminates a photomask. The reflected image of the EUV mask is projected onto a Si wafer coated with the photoresist, using projection optics.

Each of these steps, from plasma source to wafer stage, operates in a $H_2$ gas atmosphere. In fact, the lifetime of the EUV optics is shortened by debris from Sn droplets. In a $H_2$ gas atmosphere, debris can interact with the gas and is slowed or deflected, reducing their deposition on the optics [18].

## 1.2 Metrology

In a lithography machine, the wafer is placed on a stage at a particular position. During the numerous repetitive lithographic steps, the wafer is moved around and images are printed on the wafer in a step-and-scan procedure. The repeatability of the placement of the wafer on the starting position is of crucial importance. In fact, when a new resist pattern needs to be printed on top of the previous one, the lateral position of the wafer needs to be determined with sub-nanometer precision. The science used in the nanolithography industry for alignment purposes is called *metrology*. Metrology (from Greek μέτρον (to measure) + -λογία (suffix denoting the study of something)) is "the science of measurement, embracing both experimental and theoretical determinations at any level of uncertainty in any field of science and technology," as defined by the International Bureau of Weights and Measures (BIPM 2004).

In nanolithography metrology is used to verify both the quality of the mask pattern and the position of the wafer. In particular, to allow measurements of the wafer's position, many so-called *alignment markers* are printed on the wafer, by etching these structures in the Si itself. Many marker designs are possible but high precision gratings are commonly used because of their periodic nature. The period of the gratings is often in the range of 1-5 μm [19].

One of the techniques recently used for wafer alignment is laser-based

phase-grating alignment (PGA) [20]. In this technique a grating is illuminated with a laser and the diffracted beams are measured. A small translation of the wafer in the direction of the grating vector has little effect on the diffraction efficiency. It does, however, change the optical phase-difference between the $+n^{th}$ and $-n^{th}$ (n = 1, 2, 3,...) order diffracted beams, which can accurately be detected by interfering the two beams.

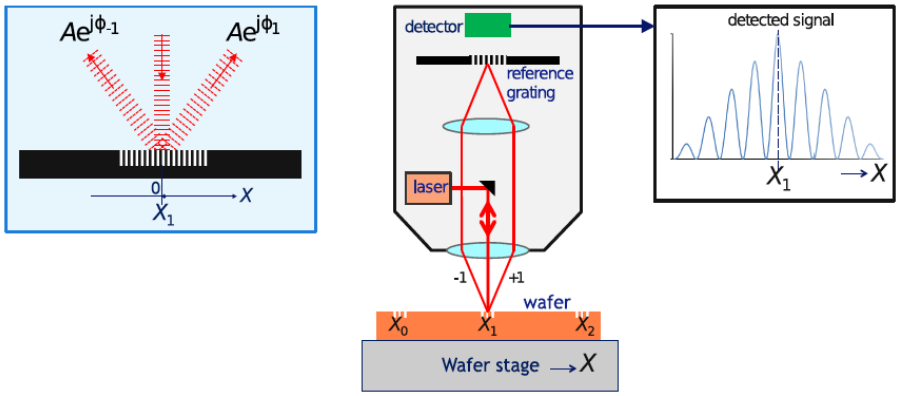


Figure 1.4: Sketch of a phase-grating alignment sensor (adapted from [21]). An alignment grating is illuminated with a laser beam. The $+1^{st}$ and $-1^{st}$ order interfere on a reference grating. The light transmitted by the reference grating is measured by a detector which detects the transmitted intensity while the alignment grating is being translated.

If we consider a grating of period $d$, when light is normally incident on the grating, the diffracted light has maxima at angles $\theta_m$, which satisfy the well-known *grating equation*

$$dsin\theta_m = m\lambda, \tag{1.2}$$

where $\theta_m$ is the angle between the diffracted beam and the grating's surface normal vector, and $m$ is an integer representing the diffracted order of interest. If a plane wave is incident at any arbitrary angle $\theta_i$, the grating equation becomes:

$$d(sin\theta_i - sin\theta_m) = m\lambda, \tag{1.3}$$

The information about the relative lateral position of the wafer is encoded in the phase of the diffracted beam. As shown in Fig. 1.4, the phase shift

is measured with 2-beam interference. In fact, a shift in position of the wafer, $\Delta x$, will cause a phase shift, $\Delta\phi$, of the diffracted light

$$\Delta\phi = 2m\pi\frac{\Delta x}{d}, \tag{1.4}$$

The phase shift is opposite for +m and -m order diffracted light. By measuring the phase shift of the diffracted light, it is possible to retrieve the new position of the wafer with sub-nanometer accuracy.

## 1.3 Going 3D: subsurface metrology

A different approach to increase the number of the elements on a chip is to build "three dimensional" chips. Recently, manufacturers decided to stack microcircuits on top of each other. In this way, it is possible to have more computational power in the same area [22]. An example is 3D NAND flash-memory, used in SSDs, or solid state drives. While planar NAND has only one layer of memory cells situated side by side, in 3D NAND the memory cells are stacked vertically in multiple layers (see Fig. 1.5). This means that, during the fabrication of the chips, the accuracy with which the wafer must be positioned is very high. As the dimensions of electronic devices get smaller, the required accuracy of a measurement increases. Moreover, as devices continue to shrink, new processes and new materials are introduced, resulting in additional challenges. For example, hardmask materials like amorphous carbon were introduced for improved pattern transfer [21]. But the real challenge comes when (partially) opaque materials are used to fabricate the multilayer architectures, so that light cannot penetrate them anymore, and the alignment markers are difficult to probe. In reality, alignment gratings are etched in areas where there are no circuits (*scribe lines*). Nevertheless, they get covered by all the materials used in the fabrication processes of the computer chips. Hence, methods need to be found that are capable of detecting micro- and nano-structures below the surface, underneath layers that may even be optically opaque. In addition, measurement methods should remain non-invasive, in the sense that they should not damage the sample or otherwise influence subsequent lithographic processing steps.

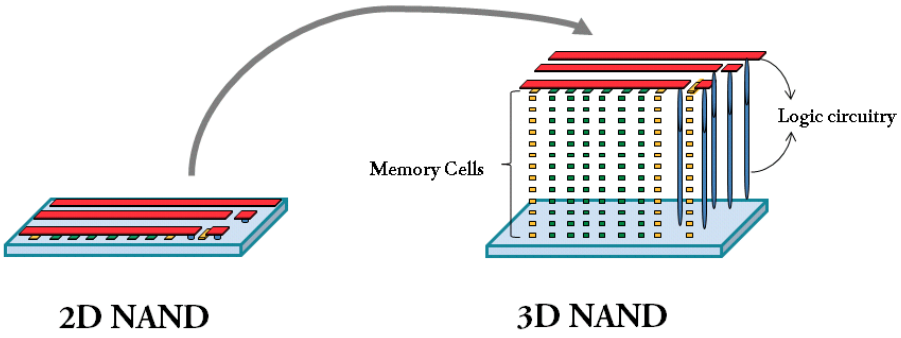


Figure 1.5: A simple schematic of a 3D NAND structure, obtained by stacking multiple planar 2D NAND. All types of flash-memory have two primary circuit components: the memory array that stores the data, and the logic circuitry that controls the flow of that data.

## 1.4 Laser-induced ultrasound to probe buried nanostructures

Fortunately, layers that are opaque to light are often transparent to sound. Therefore, a potentially interesting alternative to detect gratings buried underneath optically opaque layers is to use laser-induced ultrasound. This technique is based on the absorption of a picosecond or femtosecond laser pulse which leads to the creation of acoustic waves in the tens of GHz range [23–43]. Fundamentals of laser-induced acoustic waves have been studied extensively in the past decades [23–26, 30, 41, 44]. Numerous studies have led to a better understanding of the interaction between a femtosecond laser pulse and metal layers thicknesses in the nanometer range [45–50]. The ability of acoustic waves to propagate through layers that are not transparent to light has also led to many applications, such as high-resolution photoacoustic imaging [36–39] and material characterisation, providing information on layer thickness, sound velocity and interface properties [31–33, 51–54]. Moreover, spatial inhomogeneity of the illuminated surface can lead to excitation of shear waves and surface acoustic waves (SAWs) [27–

29]. The transducers used in conventional ultrasonics for the generation and detection of ultrasound can not reach these frequencies. Moreover, a contact-free method is often needed to prevent potential damage of the material. Ultrafast photo-acoustics is a time-domain technique with which material parameters such as thin layer thickness, sound velocity, and interface properties can be measured [31]. This method has many applications, both in the fields of science and industry. One of the more recent potential applications is subsurface metrology because ultrasound is able to penetrate many materials.

In semiconductor device manufacturing, for example, subsurface metrology is used to measure the shape and position of the wafers. Since nanometer accuracy is needed, grating-shaped alignment markers are etched into the wafer [21], as mentioned in section 1.2. In this thesis, we show how ultrashort laser-pulse induced ultrasonics can be used to detect buried gratings underneath opaque layers.

In Fig. 1.6 a sketch of the generation, propagation and detection of a laser-induced acoustic wave used to probe buried periodic nanostructures is shown. When a femtosecond pulse is focused onto the surface of an opaque metallic material, the optical energy is initially absorbed within the optical penetration depth by the electron gas. Depending on the material, the electron gas energy diffuses deeper into the material, while also losing energy to the lattice. As a result, the lattice temperature increases, causing an expansion of the material. An acoustic wave is then launched, which propagates deeper into the material. The acoustic wave is reflected back by the ridges of the gratings first, and by the valleys of the grating later. When the "acoustic replica" returns to the surface, it spatially periodically displaces the atoms at the surface and it modifies the optical properties of the material in a thin layer near the surface. These changes can be detected by a second laser pulse which is diffracted off this "acoustic" grating.

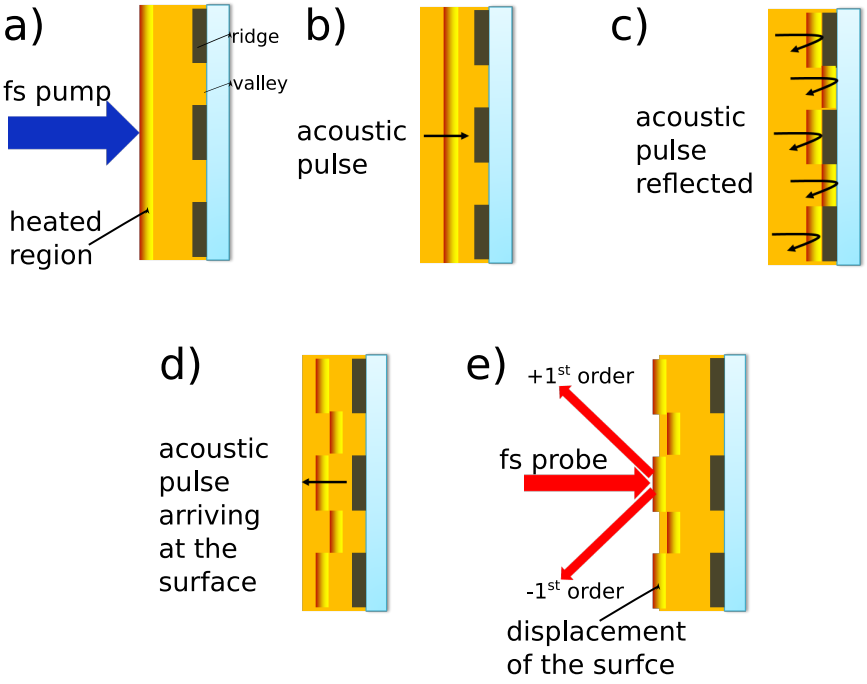


Figure 1.6: A sketch of the generation, propagation and detection of laser-induced acoustic waves used to detect buried gratings underneath an opaque layer. a) A fs laser pulse (pump) is focused onto the surface of an opaque material. The optical energy is absorbed within the penetration depth. b) An acoustic wave is launched which can travel deep into the material. c) The acoustic wave travelling into the layer will be reflected back from the interface. d) The reflected acoustic wave approaching the surface will have a spatial modulation which is a replica of the buried grating topography. e) The surface will be displaced by the arriving acoustic wave and optical properties of the material will also be modified. Either replica of the buried grating will diffract a second, delayed fs pulse (probe).

## 1.5 Contents of this thesis

This thesis mostly describes experiments aimed at understanding the generation and detection of these ultrahigh frequency sound waves for the detection of buried gratings.

In Chapter 2, the generation and detection of laser-induced acoustic waves is introduced. The generation of acoustic waves in metals is discussed by starting from the Two Temperature Model (TTM). The TTM allows us to model the laser energy absorption by the electron gas of the metal and the subsequent energy transfer to the lattice via electron-phonon coupling. The temperature increase of the lattice causes an expansion of the metal layer. When a grating is hidden below this layer, an acoustic replica of that grating will reach the surface of the sample. This spatially modulated acoustic wave is detected by diffraction of the probe beam. The detection is described using diffraction theory, both for low and high duty cycle gratings. Finally, a simple model of surface plasmon polaritons is described, as surface plasmon polaritons are shown to enhance the optical sensitivity to acoustic waves in gold.

In Chapter 3, all the experimental techniques used for the fabrication and characterisation of the samples used in this work are listed and explained. In particular, electron beam and UV lithography have been used to fabricate the gratings used in Chapter 4 and Chapter 5. Two different microscopy techniques were used, namely Scanning Electron Microscopy and Atomic Force Microscopy. Finally, the optical setups are introduced. A classical pump-probe scheme has been used to perform time-resolved measurements. Three different lasers were used: a low fluence Ti:sapphire laser, for the experiments described in Chapter 4 and Chapter 5; a high fluence Ti:sapphire laser for the experiments described in Chapter 4; and a low repetition rate Ti:sapphire laser with tunable probe pulse for the experiments described in Chapter 6.

In Chapter 4, we show how high-frequency laser-induced ultrasound can be used for detection of micro-gratings buried underneath optically opaque layers by using two different optical setups, namely a low fluence laser system and a high fluence laser system. Gratings with a 10 nm amplitude, buried underneath an opaque metal layer, were detected by observing diffraction from the spatially periodic replica reaching the surface/interface.

The acoustic wave generated at the surface propagates towards the grating and is reflected back. Here, the displacement created by the arrival of the acoustic wave creates a grating with an amplitude in the picometer range that can be detected by diffracting a time-delayed optical pulse off this grating. While measuring with the low fluence system, we find that both the shape and amplitude of the time-dependent diffracted signal are strongly influenced by the presence of a coherent background optical field created by scattering of the probe pulses by surface roughness. This field coherently adds up to the optical field diffracted by the acoustic-wave induced interface grating, amplifying the originally weak signal so that it becomes measurable. Our measurements show that, while using low fluence laser systems for photoacoustic experiments, scattering by interface roughness must be taken into account and can even be used to amplify the weak field diffracted off the grating-shaped acoustic wave.

In Chapter 5, we focus on the limits of the technique by studying what the narrowest grating lines are that can still be detected. We do this by keeping the grating period the same while decreasing the duty-cycle of the grating. We find that we can still detect buried optical gratings with linewidths as narrow as 75 nm using this technique. During our research, we found that both the shape and amplitude of the time-dependent diffracted signal are strongly influenced by the presence of a coherent background optical field created by scattering of the probe pulses by surface roughness. This field coherently adds up to the optical field diffracted by the acoustic-wave induced interface grating, amplifying the originally weak signal so that it becomes measurable. As a result the measured diffraction signal strength shows a linear dependence on grating duty-cycle rather than the expected quadratic one.

In Chapter 6, we study the detection of laser-induced acoustic waves on a plasmonic grating. In our experiments we use a gold grating fabricated on top of a $SiO_2$ substrate. Pump-probe measurements were performed on the grating, where the probe beam was tuned around the SPP resonance wavelength of 650 nm. Our results show that we are able to induce at least three different types of acoustic oscillations simultaneously on this structures, namely surface waves (SAWs), quasi-normal modes (NMs) and longitudinal acoustic waves (LWs). We observe an enhancement of the optical reflection changes due to the SAW at the SPP resonance, whilst the

optical response to the other two acoustic modes reaches a maximum on the slope of the SPP resonance.

# 2 Generation and detection of laser induced acoustic waves

In this Chapter we briefly introduce the physical mechanisms involved in the generation and detection of longitudinal acoustic waves by means of ultrashort laser pulses. Laser ultrasonics has been a subject of numerous studies [23–36, 38, 40–42, 55]. It is a widely used technique due to the many possible applications, in particular for studies of ultrafast phenomena and non-destructive characterisation of materials [31, 52–54]. Acoustic pulses of a few to hundreds of picoseconds duration, with frequencies in the GHz range, can be created using ultrashort optical pulses. When a pulsed laser beam, called *pump*, is focused onto the surface of an opaque solid, some of the optical energy is absorbed within a depth approximately equal to the optical absorption depth, and converted to heat. The production of heat results in an increase of the lattice temperature, which leads to an expansion of the lattice. The expansion launches an acoustic wave propagating into the material. Sub-surface structures or interfaces can reflect the acoustic wave back to the surface. There, the acoustic wave displaces the surface and-or changes the optical constants of the material. This can be detected by illuminating the sample with a second ultrashort pulse, called *probe*, focused onto the same spot on the sample. By changing the time delay between the two beams, the time-dependent changes in the amplitude and/or phase of the reflectivity of the probe light can be measured.

## 2.1 Generation of acoustic waves in metals

Ultrafast laser ultrasonics is often applied to thin metal films.
For a metal, the optical energy is absorbed by the electron gas within the optical penetration depth of the metal, which is typically on the order of a few tens of nanometers, in the first 200 fs.
The electrons around the Fermi level are excited to higher available states. After the electron gas thermalization, two phenomena occur: the electron gas energy diffuses deeper into the sample and it is transferred to the lattice, through electron-phonon interaction. This transfer typically happens on a time scale of less then 10 ps and the rate of the heat transfer to the lattice is determined by the electron-phonon coupling constant.
The response to ultrashort laser pulses of the electron gas and the lattice can be described by means of the Two Temperature Model (TTM).

### 2.1.1 The Two Temperature Model

The TTM [56, 57] assumes that there are two different subsystems, the electron gas and the lattice, each with a different time-dependent temperature, $T_e$ and $T_l$, respectively. Here, the electron gas is assumed to be thermalized at all times during and after the excitation.
The temporal and spatial evolution of $T_e$ and $T_l$ can be calculated by using two coupled partial differential equations, as first proposed by Anisimov et al. [58]. In one dimension, $z$, they can be written as [59],

$$C_e(T_e)\frac{\partial T_e}{\partial t} = \frac{\partial}{\partial z}\left(k_e\frac{\partial T_e}{\partial z}\right) - g(T_e - T_l) + S(z,t), \tag{2.1}$$

$$C_l(T_l)\frac{\partial T_l}{\partial t} = g(T_e - T_l), \tag{2.2}$$

where $C_e(T_e)$ and $C_l(T_l)$ are the electron and lattice heat capacities expressed in $\mathrm{Jm^{-3}K^{-1}}$, respectively. $k_e$ is the electron gas thermal conductivity, $g$ the electron-phonon coupling constant, and the source term $S(z,t)$ is the absorbed pump power density.
According to this model, the electron gas initially absorbs part of the optical energy, increasing the $T_e$. As the electron gas cools, the energy is

transferred to the lattice until the electron gas and the lattice are in equilibrium, meaning $T_e = T_l$. The stronger the electron-phonon constant, the faster the cooling.

For metals with a relatively small electron-phonon coupling constant, such as gold and silver, the electron gas energy has time to diffuse deep into the film ( $\approx 150$ nm [60]) as the electron gas releases its energy to the lattice. The electron gas cooling time in metals like gold and silver is less than 10 ps.
For films thinner than 150 nm, the layer thus heats up more or less homogeneously. This gives rise to an acoustic wave in the form of a periodically expanding and contracting layer in a direction perpendicular to the sample surface. The rapid expansion/contraction of the layer can be described as two counter propagating acoustic waves, each with a wavelength that is twice the layer thickness (corresponding to a frequency of tens of GHz).
For metals with a large electron-phonon coupling constant, such as platinum and nickel, only a thin layer heats up and electron energy diffuses only a few tens of nm. The electron gas rapidly cools to the lattice in less than 2 ps, with subsequent little energy diffusion. Here acoustic waves with much higher frequencies (greater than 100 GHz) can be generated.

## 2.2 Optical detection of acoustic waves

In a pump-probe scheme, a second, delayed probe beam is used to detect the pump-induced changes in the material. Two different possible mechanisms can influence the reflected probe field when in the presence of a pump-induced ultrasound wave. The first mechanism is due to the displacement of the surface of the sample. In general, when the high frequency acoustic wave reaches the surface it will displace the atoms. This gives rise to a change in the phase of the reflected probe pulse [35, 61]. The second mechanism is related to a local change in the optical constants of the material [62]. Changes in material density induced by the sound wave will lead to a local transient variation of the refractive index of the material. This mechanism is known as *strain-optic effect*, where the change of the material's permittivity is due to a mechanical strain [32, 63]. But the reflected probe electric field can be also affected by a change in temperature inside the material. This mechanism, known as *thermo-optic effect*, is due to a

change in refractive index in response to the temperature increase of the lattice. Strain- and thermo-optic effects can in principle influence both the intensity and the phase of the reflected probe beam.

### 2.2.1 Diffraction from "acoustic grating"

In our experiments, buried gratings with nanometer amplitudes buried underneath thin (75-500 nm) metal layers were employed. The returning acoustic wave whose wavefront has the topography of the buried grating imprinted on it, has a spatially periodic delay in the acoustic arrival time, or phase. For the metals we used (gold and nickel), the returning acoustic wave generates displacement of the atoms at the interface. For nickel, the strain-optic effect is also present. In order to detect the return of the laser-induced grating-shaped acoustic wave at the metal/glass interface, the energy of the probe beam diffracted off the resulting interface grating present at the interface was measured.

## 2.3 Diffraction theory: the Fraunhofer approximation

Diffraction from displacement gratings can be described by using Fraunhofer diffraction theory. Fraunhofer diffraction is an approximation valid when both the incident and the diffracted waves are effectively plane waves. This is true when the distance between the source and the diffracting aperture and the distance from the aperture to the receiving point are big enough for the curvature of the incident and diffracted wave to be neglected [64]. When either the source or the receiving point is close enough to the diffracting aperture, the curvature of the wave is significant and the Fresnel diffraction must be used [64]. In practice, the Fraunhofer approximation can be applied in the far field. In general, one can state that Fraunhofer diffraction occurs when

$$z > 2\frac{L^2}{\lambda}, \tag{2.3}$$

where $z$ is the observation distance, $L$ is the dimension of the aperture and

$\lambda$ is the incident wavelength. Under these conditions, the observed field strength can be found from a Fourier transform of the aperture distribution itself. In [64], Goodman derives the expression for the electric field $U$ in the far-field of an aperture source. For an aperture with aperture function $U(\xi, \eta, z = 0)$, the field $U(x, y, z)$ in the far-field of the aperture can be written as [64],

$$U(x, y, z) = \frac{e^{ikz} e^{i\frac{k}{2z}(x^2+y^2)}}{i\lambda z} \iint_{-\infty}^{\infty} U(\xi, \eta, z = 0) e^{-i2\pi(f_x \xi + f_y \eta)} d\xi d\eta. \quad (2.4)$$

This expression is the 2D spatial Fourier transform of the aperture distribution, evaluated at spatial frequencies $f_x = x/(\lambda z)$ and $f_y = y/(\lambda z)$.

### 2.3.1 Diffraction from thin sinusoidal phase grating

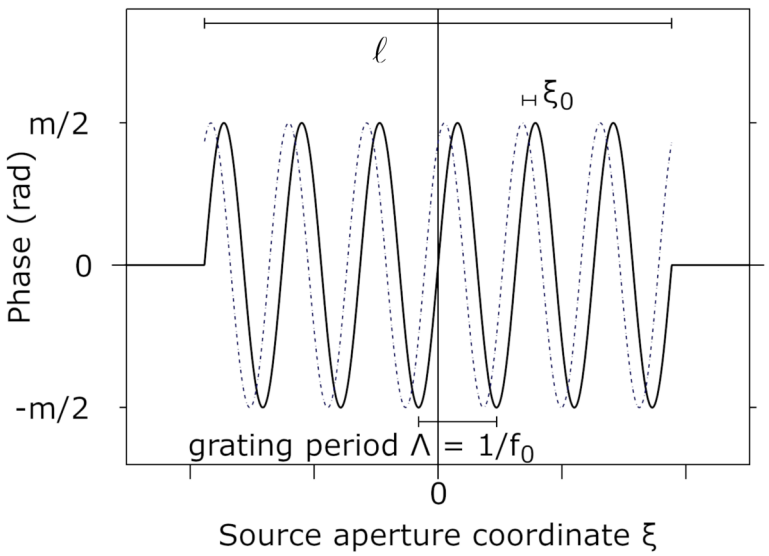


Figure 2.1: Example of a sine phase grating with grating period $\Lambda$ (spatial frequency $f_0 = 1/\Lambda$), amplitude $m/2$, and multiplied by a rect function $\text{rect}(\xi/\ell)$. The dashed line is a grating with the same rect function, but with the phase grating shifted by $-\xi_0$.

A transmission function $t_A$ can be defined, which is the ratio of the complex field immediately behind a screen to that of the field incident on the screen. If the incident field has amplitude 1 and is incident normally on the screen (so no phase variation across the aperture for the incident beam) then we can write: $t_A(\xi, \gamma) = U(\xi, \gamma, z = 0)$.
A thin sinusiodal phase grating, with dimensions $\ell$ in the $\xi$ and $\eta$-direction, can be defined by the amplitude transmission function

$$t_A(\xi, \gamma) = \exp\left[i\frac{m}{2}\sin(2\pi f_0(\xi + \xi_0))\right]\text{rect}\left(\frac{\xi}{\ell}\right)\text{rect}\left(\frac{\gamma}{\ell}\right), \tag{2.5}$$

where $f_0$ is the spatial frequency of the grating, and where $-\xi_0$ is the distance over which the grating has been displaced compared to the original position ($\xi_0$ =0). $m$ is the peak-to-valley variation of the phase.
To obtain the Fourier transform of equation (2.5), we simplify the function using the so-called Jacobi-Anger expansion [65],

$$\exp\left[i\frac{m}{2}\sin(2\pi f_0\xi)\right] = \sum_{q=-\infty}^{\infty} J_q\left(\frac{m}{2}\right)e^{i2\pi q f_0\xi}. \tag{2.6}$$

where $J_q$ is the Bessel function of the first kind, order $q$.
The Fourier transform of this is,

$$FT\left[\sum_{q=-\infty}^{\infty} J_q\left(\frac{m}{2}\right)e^{i2\pi q f_0\xi}\right] = \sum_{q=-\infty}^{\infty} J_q\left(\frac{m}{2}\right)\delta(f_x - qf_0, f_y). \tag{2.7}$$

and

$$FT\left[t_A\left(\xi, \gamma\right)\right] = \sum_{q=-\infty}^{\infty} J_q\left(\frac{m}{2}\right)\ell^2\left[\ell(f_x - qf_0)\right]\left[\ell f_y\right]\exp\left(i2\pi q f_0\xi_0\right). \tag{2.8}$$

The diffraction efficiency of the thin sinusoidal phase grating can be found by squaring the coefficients in Eq. 2.8. Thus, for the $q$-th order of this grating, the diffraction efficiency is

$$\eta_q = J_q^2(m/2), \tag{2.9}$$

where $m$ is the amplitude of the grating expressed as peak-to-peak variation of the phase.

**Diffraction from a displaced grating**

If we explicitly look at the terms $q$ =1 and $q$ =-1, we obtain:

$$\begin{aligned} U_{q=1}(x,y,z) =& \frac{e^{ikz}e^{i\frac{k}{2z}(x^2+y^2)}}{i\lambda z} J_1\left(\frac{m}{2}\right) \ell^2 \left[\ell(f_x - f_0)\right] \left[\ell f_y\right] \\ & \exp\left(i2\pi f_0 \xi_0\right) \\ U_{q=-1}(x,y,z) =& -\frac{e^{ikz}e^{i\frac{k}{2z}(x^2+y^2)}}{i\lambda z} J_1\left(\frac{m}{2}\right) \ell^2 \left[\ell(f_x + f_0)\right] \left[\ell f_y\right] \\ & \exp\left(-i2\pi f_0 \xi_0\right). \end{aligned} \tag{2.10}$$

The phase terms, $\exp(\pm i2\pi f_0 \xi_0)$, are opposite in phase as expected.
With a simple variable transformation ($\xi_0 = \acute{\xi}_0 + \Lambda/4$, with $\Lambda = 1/f_0$), we can turn the sine-wave grating into a cosine-wave grating. For $\acute{\xi}_0 = 0$, a non-displaced cosine grating is observed which gives, in fact, expressions for the field where the phases of the -$1^{st}$ and +$1^{st}$ order diffracted fields are the same, as expected.

### 2.3.2 Diffraction efficiency as a function of the duty-cycle of the grating

In Chapter 5, we describe experiments on photo-acoustic detection of low duty cycle ($\ll 50\%$) buried gratings. For this research, it is useful to have expressions describing the diffraction efficiency from such gratings.
To describe the dependence of the diffraction efficiency of a grating on its duty cycle and amplitude, Chang et al. [66] introduced a binary diffraction model. The model assumes a grating with a binary amplitude, which translates into a binary shift in the phase of the reflected light, when comparing light reflected off the ridges and the valleys of the grating. This grating can be described as an infinite train of rectangular pulses with a uniform width. The incident wavelength must be much smaller than the period of the grating ($S$) so that the scalar approximation can be applied.

According to the Fraunhofer diffraction theory, the far-field diffraction wavefront is the Fourier transform of the original wavefront.
The far-field wavefront function of a normally incident planar wavefront on top of a grating can be expressed as [66],

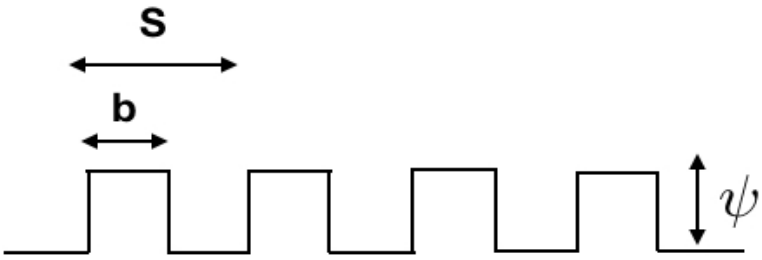


Figure 2.2: Complex wavefront of a binary grating, where $b$ is the linewidth and $S$ is the period of the grating (figure adapted from [66]).

$$U = \begin{cases} A_0 + [A_1\cos(\psi) - A_0]D + iA_1\sin(\psi)D, & m = 0 \\ [A_1\cos(\psi) - A_0]D(mD) + iA_1\sin(\psi)D(mD), & m = \pm1, \pm2, ..., \end{cases} \tag{2.11}$$

where $m$ is the diffraction order; $A_0$ and $A_1$ are the amplitudes of the reflectance of the peaks and the valleys of the grating, respectively; $\psi$ is the phase difference between the light reflected from the valleys and from the ridges of the grating; $D$ is the duty cycle of the grating expressed as the ratio $D = b/S$, with $S$ the period of the grating (see Fig. 2.2).

The diffraction efficiency $\eta$ is defined as the ratio between the intensity of the diffracted light $U$ and that of the incident light $U_0$:

$$\eta = \frac{|U|^2}{|U_0|^2}. \tag{2.12}$$

For nonzero diffraction orders, assuming the intensity of the incident light is one, one has:

$$\eta|_{m\neq0} = [A_0^2 + A_1^2 - 2A_0A_1\cos\psi]D^2\mathrm{sinc}^2(\mathrm{mD}). \tag{2.13}$$

For the samples used in our experiments, the same material was deposited

on both the valleys and the peaks of the grating. Thus, in our case, $A_0 = A_1 = A$ and Eq. 2.13 becomes:

$$\eta|_{m\neq 0} = 2A^2(1-\cos\psi)D^2\mathrm{sinc}^2(\mathrm{mD}). \tag{2.14}$$

In case of small duty cycles ($D << 0.5$), the diffraction efficiency can be approximated by,

$$\eta|_{m\neq 0} = 2A^2(1-\cos\psi)D^2. \tag{2.15}$$

For later use in this thesis, it is important to notice that this equation shows that the diffraction efficiency has a quadratic dependence on the duty cycle of the gratings.
Moreover, for small values of $\psi$, we can rewrite Eq. 2.15 as

$$\eta|_{m\neq 0} = 2A^2D^2\frac{\psi^2}{2}. \tag{2.16}$$

As $\psi$ is proportional to the amplitude of the grating, one can conclude that the diffraction efficiency scales quadratically with the amplitude of the grating as well.

## 2.4 Surface Plasmon Polaritons

Interaction between metals and electromagnetic waves can be described by the Drude model [67]. According to this simple model, the optical properties of a metal can be explained by looking at the metals as a collection of immobile positively charged ions on a lattice and a gas of free electrons which can move. At the interface between a metal and air, a mixture of electromagnetic waves and electron oscillations can exist that can propagate along the interface which are called Surface Plasmon Polaritons (SPPs) [68, 69]. The surface charge density oscillations associated with SPPs can give rise to optical near-fields which are spatially confined near the metal surface, as shown in Fig. 2.3(a). The strength of the electric field decreases exponentially in a direction perpendicular to the interface, both in the metal and in the dielectric (Fig. 2.3(b)).

One can consider SPPs as transverse waves propagating along a metal-dielectric interface and evanescently decaying in the direction perpendicular to it. Solving Maxwell's equations with the right boundary conditions, the dispersion relation of SPP can be derived as [70],

$$|k_{SPP}| = \frac{\omega}{c}\sqrt{\frac{\epsilon_1\epsilon_2}{\epsilon_1+\epsilon_2}}, \tag{2.17}$$

where $k_{SPP}$ is the SPP wave vector, parallel to the interface; $\epsilon_1$ and $\epsilon_2$ are the permittivities of the dielectric and the metal, respectively and for simplicity we assume that they are real; $\omega$ is the angular frequency; $c$ is the speed of light in vacuum.

### 2.4.1 Grating-coupling of SPP

The dispersion relation of a surface plasmon at a metal/dielectric interface is schematically shown in Fig. 2.3(c). The black dashed curve represents the dispersion relation in Eq. 2.17, where only the real part of the permittivity of the metal is taken into account. $\omega = ck_x$ represents the dispersion relation of light, propagating along the $x$-direction in air. At a given frequency of the incident light $\omega_0$, the length of wavevector $k_{SPP}$ of the plasmon is always greater than that of light in air, $k_0$. Thus, in order to excite a SPP using light we need to increase its wavevector. This is possible only in configurations where wavevector-matching between the incident light and

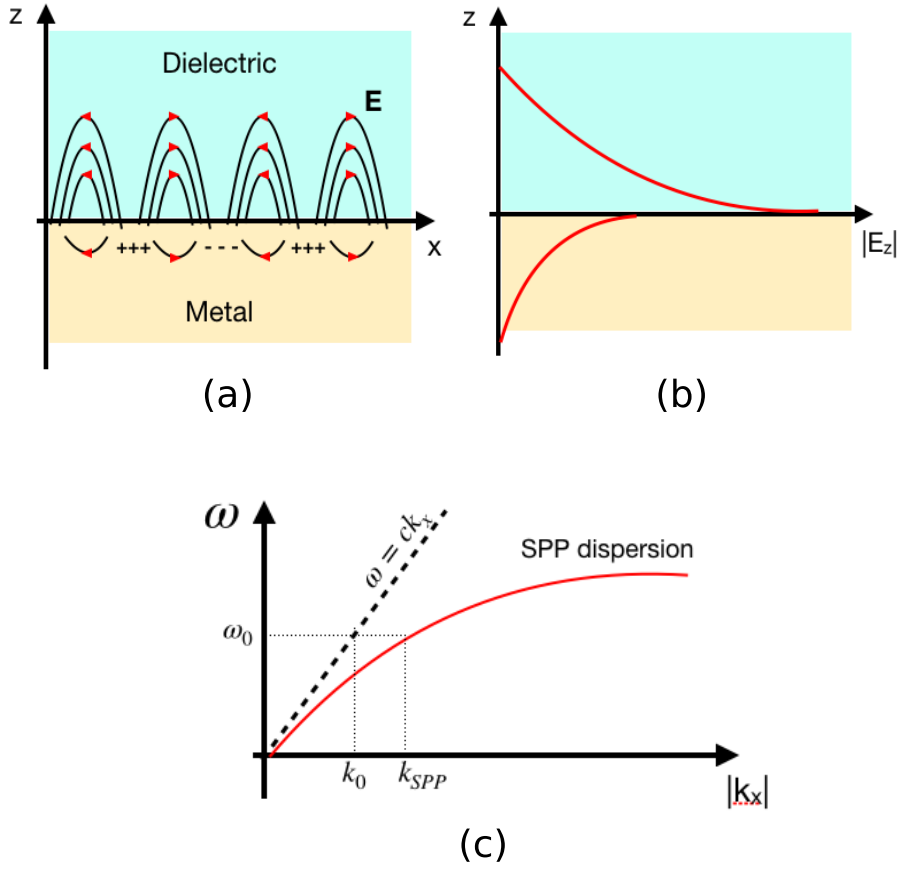


Figure 2.3: (a) Schematic of the SPP mode excited at the metal/dielectric interface. (b) The evanescent fields in the perpendicular direction decay exponentially both in the dielectric and in the metal. (c) The dispersion curve of a SPP mode. The mode clearly lies below the light line $\omega = ck_x$, which means that a momentum mismatch has to be overcome in order to couple light to an SPP mode.

SPP is provided. One of the methods to provide the required additional momentum is to generate the SPP at the interface of a medium with a refractive index greater than 1. For this, a glass prism can be used, either in the Otto [69, 71] or in the Kretschmann configuration [69, 72].

Another method to excite SPP is to "deform" the metal surface with a periodic corrugation, namely a grating [68, 73, 74]. A grating has a fixed wavevector $k_g$ that can be added (or subtracted) from the incident light wave-vector

$$k_g = \frac{2\pi}{D}, \tag{2.18}$$

where $D$ is the period of the grating.

Thus, the SPP-grating coupling can be expressed as [68]

$$k_0 \pm k_g = k_{SPP}, \tag{2.19}$$

where $k_0 = \frac{\omega}{c}\sin\theta$ is the wavevector of the incident light and $\theta$ is the angle of incidence with respect to the surface normal; $k_{SPP}$ is the wavevector of the surface plasmon.

Using 2.18, we obtain

$$\frac{\omega}{c}\sin\theta \pm N\frac{2\pi}{D} = k_{SPP}, \tag{2.20}$$

where $N = 1, 2, 3...$ and $k_{SPP}$ given by 2.17. As shown in Fig. 2.5, the SPP travels along the air/metal interface in the $x$-direction, either forward (b) or backward (a). In this thesis, $N = 1$.

We show in Fig. 2.5 a schematic of the coupling of SPPs using gratings. The red curves represent the dispersion relation of the SPP propagating along the metal surface in the +1 or -1 direction. Given a grating with wavevector $k_g$, we indicate with the blue lines the brillouin zones due to scattering by the grating, corresponding to $N = \pm 1$. The black, dashed line is the dispersion curve of the incident light. The grey lines represent the resultant dispersion when the grating vector is added/subtracted from the incident light. We can see how $k_g$ assist to satisfy the SPP excitation at two frequencies, $\omega_{-1}$ and $\omega_{+1}$. Considering an angle of incidence $\theta$, the direction of propagation of the SPP for the two cases is shown if Figs. 2.5 (b) and (c).

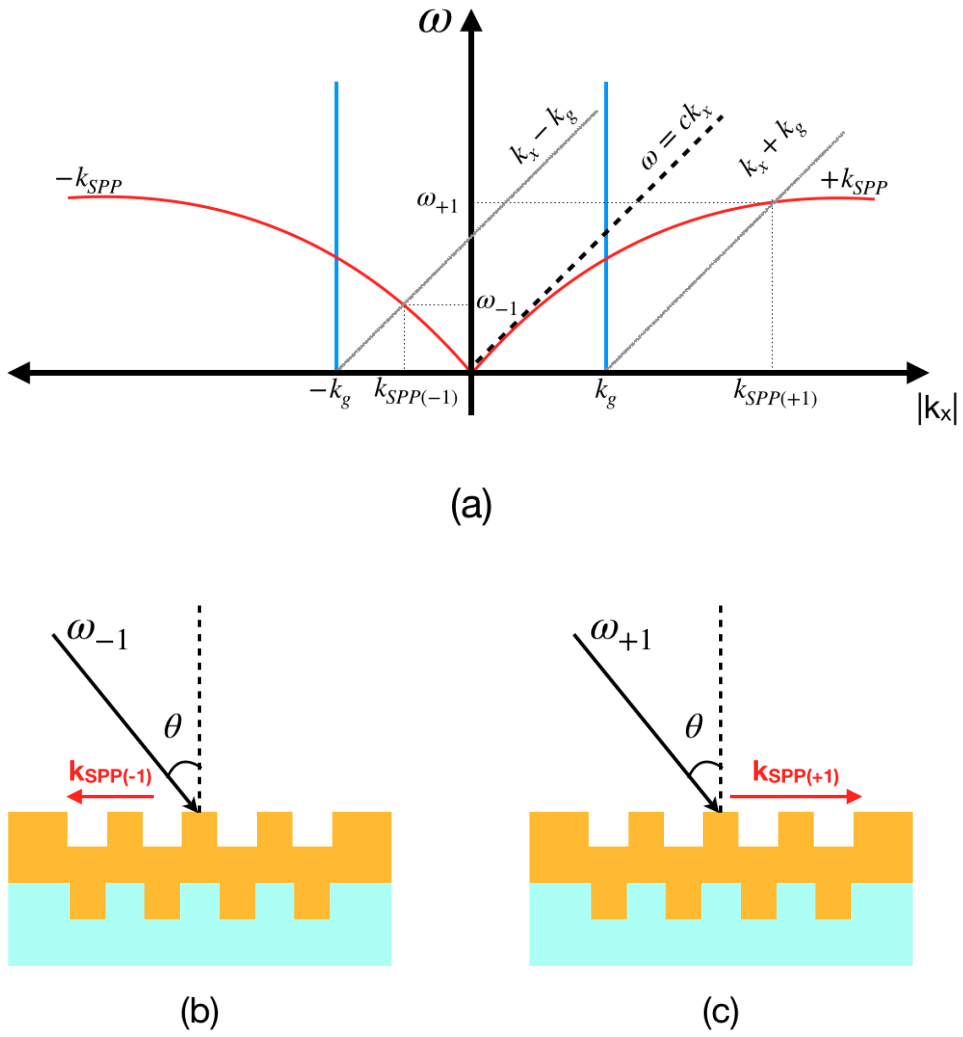


Figure 2.4

Figure 2.5: Schematic of the excitation of SPPs on a grating. In (a), the $x$-component of the incident light, $k_x$, is shown with the dashed black line. The scattering of light by the grating is represented by the grey lines, $k_x + k_g$ and $k_x - k_g$. SPPs are excited at frequencies where these lines intersect the SPP dispersion curves, $-k_{spp}$ and $+k_{spp}$. In (b) and (c) the direction of propagation of SPPs on a grating for the two incident light frequencies, $\omega_{-1}$ (a) and $\omega_{+1}$ (b) is shown.

# 3 Experimental Methods

This Chapter describes the experimental methods used for the fabrication and characterisation of the samples used in the measurements discussed in this thesis. They include preparation of the substrates, electron beam (e-beam) and UV lithography, subsequent metal evaporation, and microscopy techniques used to characterise the fabricated nanostructures. These samples are then used in time-resolved electron dynamics and photoacoustics measurements using pump-probe setups. This Chapter is in part based on and borrows from [75, 76].

## 3.1 Nanofabrication of the buried gratings

In most of the work described in this thesis, we focus on metal nano- and micro-gratings buried underneath layers of optically opaque materials. In principle, buried gratings can be made by etching them in Si followed by the deposition of a gold layer on top of the grating. In doing this, however, the gold surface topography will simply follow the grating topography and a full gold grating would be the result. In real semiconductor device manufacturing, deposition steps are often followed by polishing steps to remove this residual topography. Such a procedure is beyond the capabilities of our cleanroom facilities, and we therefore decided to make "buried" gratings in a different way. Our samples are fabricated by first depositing a

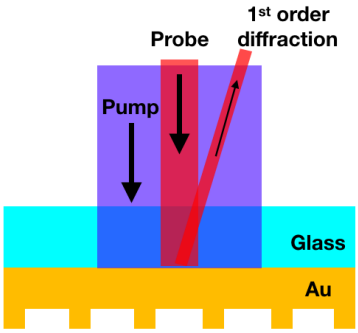


Figure 3.1: Pump-probe on buried grating.

flat gold layer on glass, followed by the fabrication of a grating, using e-beam lithography, on top of this layer. By now performing the pump-probe measurements from the glass side (Fig. 5.1 ) the gratings are optically invisible to the laser pulses and can be considered "buried". Most importantly, since at this interface the gold is essentially flat, we avoid any residual topography grating which could lead to a relatively strong constant optical diffraction. Note that at the glass/Au interface there will also be interface roughness. This roughness, however, will scatter light into all directions, whereas a grating, even when its amplitude is considerably smaller than the roughness, will diffract light into a few particular diffraction orders only.

### 3.1.1 Substrate preparation

The fabrication of our samples starts with the choice of the right substrate. We chose glass, because it is transparent to the wavelengths of our laser (400 and 800 nm) and cheap. All the buried gratings used in this work were fabricated on 175 µm thick glass substrates.

The first step is to clean the substrates. After a few minutes of sonication in water, they are dipped in a *base piranha* solution. It is a 5:1:1 mixture of water ($H_2O$), ammonium hydroxide ($NH_4OH$) and hydrogen peroxide ($H_2O_2$) at 75 °C, used to clean organic residues off substrates. Because the mixture is a strong oxidizing agent, it will remove most or-

ganic matter. After rinsing it in abundant distilled water, the substrates are dried and ready to be used.

The second step is to spincoat electron-beam sensitive resists onto the glass substrate. Spin coating is one of the most common techniques for applying thin films to substrates. One of the advantages of spin coating is its repeatability. Moreover, it can produce uniform films, from a few nanometres to a few microns in thickness, on a flat substrate, in a very short time. A small amount of resist is applied at the center of the substrate. The substrate is then rotated at high speed in order to homogeneously spread the coating material by centrifugal force. Rotation is continued while the fluid spins off the edges of the substrate, until the desired thickness of the film is achieved. The obtained thickness depends on the angular speed of spinning: the higher the speed, the thinner the film.

In this thesis we use a lift-off process using a bilayer of PMMA (poly methylmethacrylate) and copolymer MMA (8.5) (methyl methacrylate) as high-resolution positive-tone resists. Using the bilayer, an undercut profile is achieved after development. For the bottom layer we chose MMA, which has a lower molecular weight than PMMA. It will be the "sacrificial" layer. In fact, by exposing both layers with the same dose in the e-beam lithographic machine, MMA will became more soluble than PMMA and, during the development step, it will dissolve faster. So the pattern written in the PMMA will give the real size of the nanostructure, while the MMA layer is there only to achieve the undercut. The MMA/PMMA bilayers are usually used in electron-beam lithography for lift-off of metallic structures. For good lift-off an undercut resist profile is needed. In this way the coating of the sidewall of the resist when metal is evaporated is minimised. A good estimation in order to have undercut is that the lower layer of resist should be twice the thickness of the metal we want to deposit.

### 3.1.2 Electron-beam Lithography

Electron-beam lithography (EBL) is a powerful technique for creating nanostructures that are too small to be fabricated with conventional photolithography. State of the art EBL systems can achieve resolutions of a few nanometres. However, the main limitation of EBL is exposure speed, because it takes a long time to write high resolution patterns. Electron beam

lithography operation is based on the same principles as SEM and TEM. In EBL, a finely focused electron beam with a Gaussian profile is used to expose electron-sensitive resist in a desired pattern. The technique works by moving the highly focused electron beam over a sample to write out the designed pattern. In our case, since we are writing long lines (2 mm), we chose a different operation mode in which the beam is fixed and the stage is moving at a speed $< 1$ mm/s. In this work, EBL was performed using the Raith Voyager at the Amsterdam NanoLab (AMOLF). The system was operated at 50 kV with different expose doses, depending on the size of the grating lines. We used 600 $\mu C/cm^2$ for the 1 µm and 500 nm lines and 700 $\mu C/cm^2$ for the 250, 125 and 75 nm lines. The writing time was 2 hours for a 2x2 $mm^2$ grating. During the development step, the exposed sample is immersed in Pentyl acetate ($C_7H_{14}O_2$) which can dissolve both MMA and PMMA, for 90 seconds. To achieve a successful lift-off, it is extremely important to clean the area on which the metal will be deposited from any residual MMA. For this reason, the sample is subsequently rinsed in Methyl Isobutyl Ketone (MIBK):Isopropyl Alcohol (IPA) = 9:1 and later in IPA for a few seconds.

### 3.1.3 UV Lithography

The samples used in Chapter 4 were fabricated by using UV Lithography (UVL). This technique uses UV light to write patterns onto a photoresist. UVL allows to achieve pattern resolutions <1 µm and to write areas as big as 6 inches. There are different techniques for transferring the pattern onto the photoresist. The most common technique uses a photomask. A UV photomask is made from a transparent material, typically fused silica, in which the pattern is engraved. The substrate is then exposed through the photomask to a UV light source. The resist, S1805, was spin-coated onto the substrate for approximately 45 seconds at 2000 rpm. The resist-coated sample was then exposed with UV light through the mask containing the grating pattern for 2-3 seconds. The exposure wavelength is 385 nm, and the system operated at 25 mW of optical power. The resist is then developed in Ma-D 533-S, for approximately 30 seconds.

Since the lines of our gratings are as wide as 6 µm, the EBL resolution is not needed for patterning this kind of structures. Moreover, by using

UVL the patterning time is reduced so that bigger areas can be written in less time. In this work, UV lithography was performed by using the Suss MABA6 Mask aligner in the Amsterdam NanoLab (AMOLF).

### 3.1.4 Evaporation and lift-off

Thermal evaporation is a thin-film physical vapour deposition (PVD) technique that is commonly used in nanofabrication.
Fig. 3.2 shows the schematic of the thermal evaporation process. Ther-

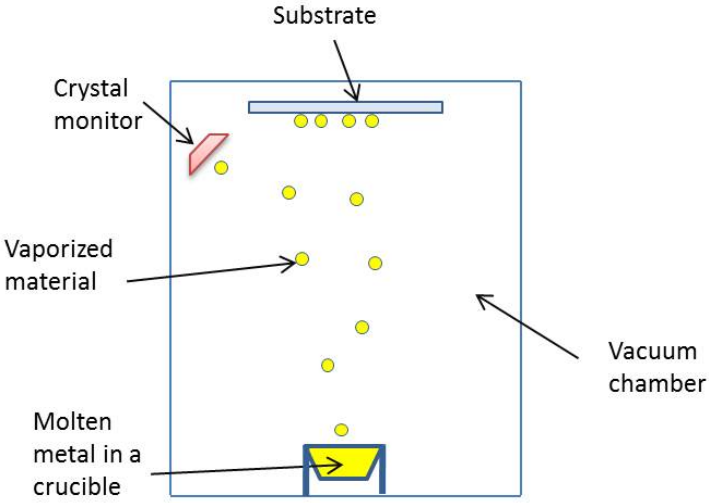


Figure 3.2: Schematic of thermal evaporation.

mal Evaporation is done by heating a solid material inside a high vacuum chamber, reaching a temperature which produces some vapour pressure. The material is placed in "boats", which are tungsten or molybdenum crucibles, some distance below the sample target. A current heats the boat and the metal inside of it, to the metal's melting point. The metal vapour rises towards the substrates which are held upside-down at the top of the chamber. High vacuum conditions with a pressure range of $10^{-6}$ to $10^{-7}$ mbar are required for metal particles to travel directly to the substrate without colliding with any residual background gases. Typical deposition rates for evaporation are 0.1 nm/s to 1 nm/s, which is relatively low compared to other thin film deposition techniques. The method is not expensive, and it

is versatile as a variety of metals can be used as target. In this work, we used thermal evaporation for the deposition of gold layers.
For materials with a higher melting point, such as nickel, Electron-Beam Physical Vapor Deposition (EBPVD) was used. It is a form of physical vapour deposition in which the source material is targeted under high vacuum conditions with a high-energy electron beam which is able to achieve rapid melting and evaporation of the target materials. The target atoms then coat the substrate on which we want to deposit the thin metal layer. With EBPVD significantly higher deposition rates can be reached [77].
After metal deposition, since we are using positive tone resists, we need to lift-off the patterned resist left on the substrate. Lift-off refers to the process of washing away the resist leaving behind the metal film only in the patterned area. We chose as solvent Anisole ($C_7H_8O$). The sample is immersed in the solvent, together with a stir bar, and placed on a magnetic hot plate at 60 °C for 30 - 40 minutes. As soon as the resist layer is removed (lift-off), the sample is cleaned in IPA and dried.

### 3.1.5 Scanning Electron Microscopy

After fabrication, the quality of the samples and the size of the nanostructures were checked by using different microscopy tools. One of them is Scanning Electron Microscopy (SEM). The electron microscope was developed to image structures smaller then the visible wavelengths of light used in the optical microscopes. In fact, high energy electrons have much shorter wavelengths, enabling nanometer resolution. SEM can create images by scanning an electron beam on a surface. Electrons are produced at the top of the chamber and accelerated downward. A system of lenses and apertures directs and focuses the beam onto the surface. When the electron beam hits the surface of the sample, it penetrates up to a few microns, depending on the accelerating voltage and the density of the sample. During the contact, scattered electrons, including secondary and back-scattered electrons as well as X-rays can be released from the surface of the sample. The scatter patterns give us information on size, shape, texture and composition of the sample. A variety of detectors are used to attract the different types of scattered electrons, such as In-Lens, In-Column, and Everhart–Thornley Detector Systems [78]. They convert the collected signals

into images. For conventional imaging in the SEM, specimens must be electrically conductive, at least at the surface, and electrically grounded to prevent the accumulation of electrostatic charge. In this work, SEM analysis was performed by using the FEI Verios 460 in the Amsterdam NanoLab (AMOLF). In our analysis, we used both secondary and back-scattered electrons.
In Fig. 3.3 we show an example of two SEM measurements of Au gratings.

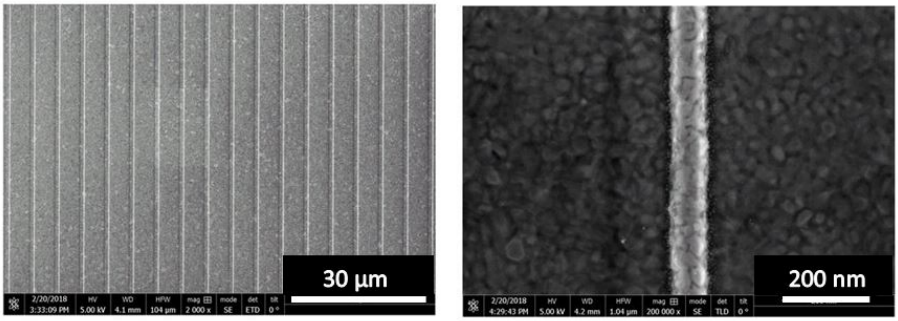


Figure 3.3: (a) SEM measurement of a 6 µm period, 40 nm amplitude and 1 µm linewidth Au grating. This is an overview of the array. (b) SEM measurements on a single line for the 6 µm period, 40 nm amplitude and 75 nm linewidth Au grating. Both gratings were fabricated on a 90 nm thick Au layer deposited on the glass substrate.

### 3.1.6 Atomic Force Microscopy

In order to measure the topography and the roughness of our samples, atomic force microscopy (AFM) measurements were performed.

AFM is a high-resolution scanning probe microscopy tool which can measure material properties, such as height, surface roughness, and friction, with a mechanical cantilever. An AFM images the topography of a sample surface by scanning the cantilever on a sample surface. As the tip approaches the surface, attractive or repulsive forces between the surface and the tip will deflect the cantilever towards or away from the surface, respectively.
In the *contact mode*, the tip which scans the sample is in close contact

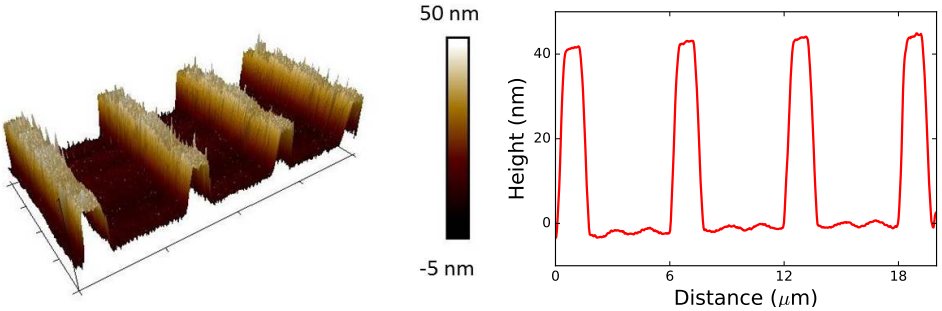


(a) (b)

Figure 3.4: (a) 3D AFM image of a 6 µm period, 40 nm amplitude and 1 µm linewidth Ni grating. (b) The height profile of the grating.

with the surface. The force on the tip is repulsive. In contact mode AFM the deflection of the cantilever is sensed and compared in a DC feedback amplifier to some desired value of deflection.
When tip contact might alter the sample, the *non-contact mode* can be used. In this mode the tip is 50 - 150 Angstrom above the sample surface. Attractive Van der Waals forces acting between the tip and the sample are detected, and topographic images are constructed by scanning the tip above the surface.
In both cases, a laser beam is reflected off the flat top part of the cantilever. The direction of the reflected beam will change at any cantilever deflection. A position-sensitive photodiode can be used to track these changes. The tip-sample force ($F$) is given by Hooke's law [79]:

$$F = -k\delta_c \tag{3.1}$$

where $k$ is the spring constant (stiffness) of the cantilever and $\delta_c$ is the cantilever deflection. The force is constantly measured during the scan and by using a feedback loop to control the force or the height of the tip above the surface, the AFM can generate an accurate topographic map of the surface. An example of an AFM measurement on a low duty cycle Ni grating, fabricated on a 200 nm thick Ni layer, is shown in Fig. 3.4 .

## 3.2 Optical setups

Generation and detection of acoustic waves in metal layers by using a pump-probe setup have been already performed in the past [see 23, 24, 33, 80–83, for example]. The general principle of a time-resolved measurement is shown in Fig. 3.5. A more energetic laser pulse, called the *pump*, hits the sample, changing some material properties. A second, weaker pulse, called the *probe*, arrives on the sample, on the same position, after an adjustable time delay. By observing the transmission/reflection of the probe as a function of the time delay, it is possible to obtain information on the processes initiated by the pump pulses. The probe signal is typically averaged over many pulses, so that a fast photodetector is not required. The temporal resolution is fundamentally limited only by the pulse duration of pump and probe pulses.

The experiments described in this thesis were performed in three different optical setups.

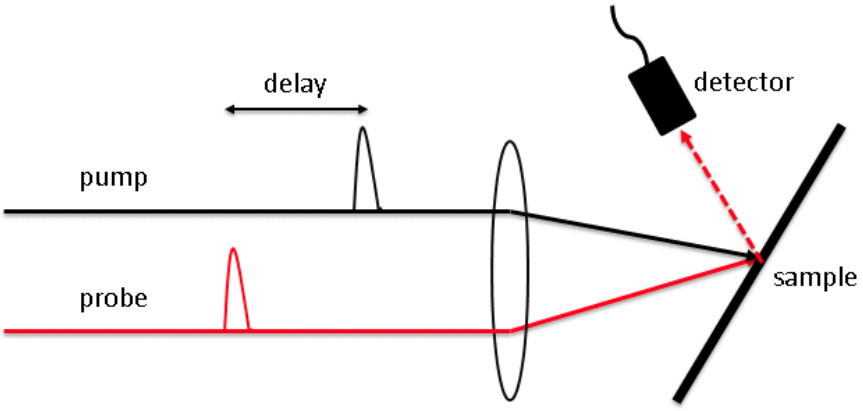


Figure 3.5: Schematic of a pump-probe setup.

### 3.2.1 High Repetition Rate Setup

Part of our experiments were performed using the pump-probe setup schematically shown in Fig. 3.6.

The laser is a Ti:Sapphire oscillator (Femtolasers XL500) generating 70 fs pulses at a repetition rate of 5.1 MHz, centered at a wavelength of 800 nm. The laser output is split into two using a 90/10 beamsplitter. The stronger beam passes through a mechanical chopper which modulates the beam at 6 kHz and is subsequently frequency doubled in a 200 µm $\beta$-barium borate (BBO) crystal to generate 400 nm pump pulses. The other, 800 nm beam is used as the probe. The time delay between pump and probe is varied by changing the optical path length with a mechanical delay stage on which two mirrors are mounted in a retro-reflecting geometry. The two beams recombine on a dichroic mirror in a collinear geometry and are then focused onto the same spot on the sample by a 100 mm focal length lens. The first-order diffracted probe beam is measured by a Si photodiode and the photodiode signal is sent to a lock-in amplifier that uses a 6 kHz reference signal from the mechanical chopper.

The pump beam has a spot size of 50 µm diameter on the sample and a pulse energy from 8 to 20 nJ, depending on the experiment. The probe has a spot size of 40 µm diameter and its pulse energy is kept constant at about 12 nJ. Note that for a pump-probe experiment, the power in the probe is unusually high, even higher than the pump power. The reason for this is that in this experiment we want to detect the buried grating through diffraction by the acoustic replica. Anticipating weak signals, every attempt was made to enhance the signal, including using a very strong probe pulse. However, the reflectivity of the metals used in this work at 800 nm is much higher than at 400 nm, so the influence of a higher probe fluence on the generated acoustic wave by the pump is expected to be small. The sample is mounted on a motorised translation stage which provides motion on three dimensions with a precision of 0.1 µm.

### 3.2.2 Low Repetition Rate Setup

The other setup follows a pump-probe scheme as well but with a different laser system (see Fig. 3.7). A Ti:sapphire multi-pass amplifier is used, which generates 30 fs pulses with a repetition rate of 1 kHz and with a wavelength centered at 800 nm. The output is split in two parts by a 95/5 beamsplitter. The stronger part is frequency doubled with a 100 µm thick BBO crystal to generate 400 nm pump pulses. The pump pulses are

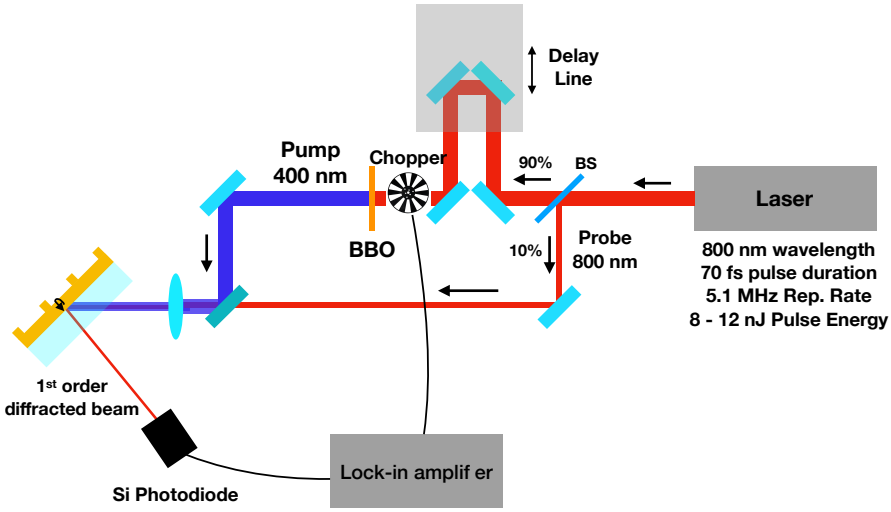


Figure 3.6: Schematic of the experimental setup. The output from a 5.1 MHz repetition rate Ti:sapphire laser oscillator with a central wavelength of 800 nm is split into two parts. One beam is frequency doubled to a wavelength of 400 nm by a BBO crystal and modulated by a mechanical chopper at 6 kHz. This beam constitutes the pump beam. The other beam with a central wavelength of 800 nm is the probe beam. The two beams are focused onto the sample on the same spot. The pump-induced first-order diffracted probe beam is measured by a silicon photodiode.

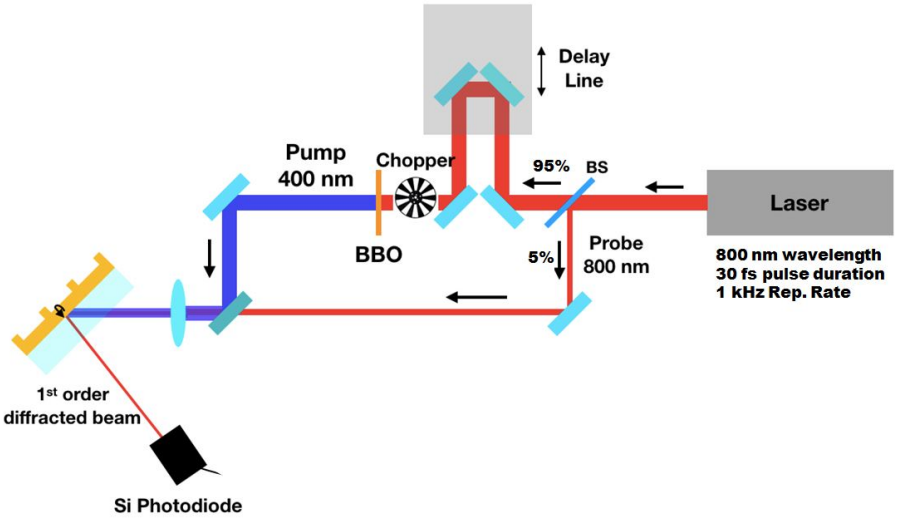


Figure 3.7: Schematic of the low repetition rate setup. The output from a 1 kHz repetition rate Ti:sapphire multi-pass amplifier with a central wavelength of 800 nm is split into two parts. One beam is frequency doubled to a wavelength of 400 nm by a BBO crystal and modulated by a mechanical chopper at 500 Hz. This beam constitutes the pump beam. The other beam with a central wavelength of 800 nm is the probe beam. The two beams are focused onto the sample on the same spot. The pump-induced first-order diffracted probe beam is measured by a silicon photodiode.

then modulated at 500 Hz by a mechanical chopper. The pump diameter is about 500 µm pulse energy ranges from 6 µJ to 8 µJ depending on the sample. The probe diameter is 250 µm and the probe pulse energy is kept constant at 2 µJ. The detection scheme is kept the same as the previous setup but, since no lock-in amplifier is used in this case, the signal recorded when the chopper is blocking the pump is subtracted from the signal when the pump beam is transmitted.

### 3.2.3 Tunable Probe Setup

For the experiments described in Chapter 6, a tunable probe setup was employed. A schematic of this setup is shown in Fig. 3.8. The pump-probe setup is built around a Ti:sapphire amplifier (Astrella, Coherent), which generates 35 fs pulses with a repetition rate of 1 kHz and a central wavelength of 800 nm. 90 % of the output of the laser is sent into a High Energy Travelling-wave Optical Parametric Amplifier (HE-TOPAS), a commercial device produced by Light Conversion. This device is able to make the output of the laser tunable, through a second order nonlinear process. The HE-TOPAS converts the wavelength of the laser from 800 nm to a tunable range of 1150 to 2400 nm. It is frequency doubled with a 100 µm thick BBO crystal and pulses with a wavelength in the range of 600-700 nm are used as probe pulses. The remaining 10 % of the laser output is used as pump beam, after frequency doubling in a BBO crystal to generate 400 nm pump pulses. The pump pulses are modulated at a frequency of 500 Hz with a mechanical chopper synchronised to the 1 KHz repetition rate of the laser. The time delay between the pump and probe beams is obtained by sending the pump to a mechanical translation stage on which two mirrors are mounted in a retroreflecting geometry, to change the optical path length. The pump beam has a spot size of 400 µm and a pulse energy of 6 µJ, after the chopper. The probe beam has a spot size of 80 µm and a pulse energy of $\approx 0.3$ µJ. As for the Low Repetition Rate Setup, the pump signal recorded when the beam is blocked by the chopper is subtracted from the signal when the pump beam is transmitted. The sample is mounted on a rotational stage on top of a translation stage, which can translate the sample in the x,y, and z direction.

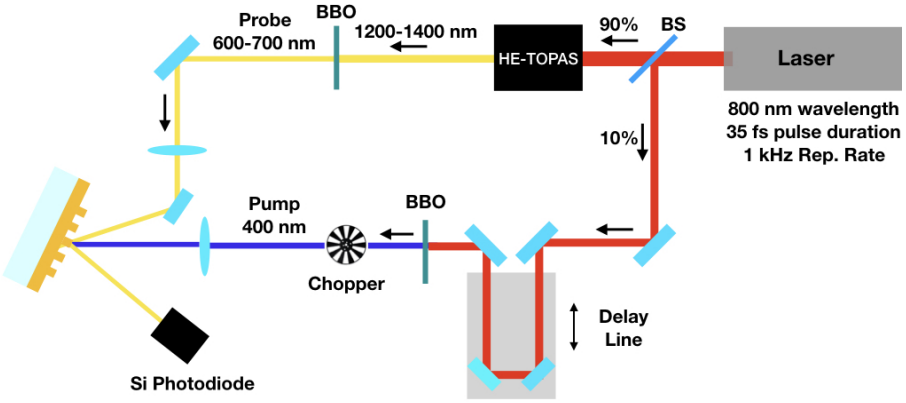


Figure 3.8: Schematic of the tunable probe setup. The output from a 1 kHz repetition rate Ti:sapphire amplifier with a central wavelength of 800 nm is split into two parts. One beam is frequency doubled to a wavelength of 400 nm by a BBO crystal and modulated by a mechanical chopper at 500 Hz. This beam constitutes the pump beam. The other beam is sent into a HE-TOPAS to generate a pulse tunable from 1200 to 1400 nm. The output is frequency doubled by a BBO crystal to generate pulses with a wavelength from 600 to 700 nm. This beam constitutes the probe beam. The two beams are focused onto the sample on the same spot. The specular reflected beam is measured by a silicon photodiode.

# 4 Role of scattering by surface roughness in the photoacoustic detection of hidden micro-structures ⋆

In this Chapter, we present an experimental study in which we compare two different pump-probe setups to generate and detect high-frequency laser-induced ultrasound for the detection of gratings buried underneath optically opaque metal layers. One system is built around a high fluence, low repetition rate femtosecond laser (1 kHz) and the other around a low fluence, high repetition rate femtosecond laser (5.1 MHz). We find that the signal diffracted by the acoustic replica of the grating as a function of pump-probe time delay is very different for the two setups used. We attribute this difference to the presence of a constant background field due to optical scattering by interface roughness. In the low fluence setup the optical field diffracted by the acoustic replica is significantly weaker than the background optical field, with which it can destructively or constructively interfere. For the right phase difference between the optical fields, this can lead to a significant enhancement or attenuation of the weak field diffracted off the grating-shaped acoustic waves. For the high fluence system, the situation is reversed because the field diffracted off the acoustic wave-induced grating

⋆This chapter has been published in a slightly modified form as Appl. Opt. 59, 9499-9509 (2020).

is significantly larger than the background optical field. Our measurements show that optical scattering by interface roughness must be taken into account to properly explain experiments on laser-induced ultrasound performed with high repetition rate lasers systems and can be used to enhance signal strength.

## 4.1 Introduction

We recently showed that laser-induced ultrasound can be employed for the detection of micro- and nano- structures buried underneath metal layers [84]. With this technique, we were able to detect gratings underneath optically opaque layers and dielectric multi-layers, even after propagation of the acoustic wave through as many as 2x20 dielectric layers.

Here, we show how light scattered by interface/surface roughness can influence the shape and amplitude of the time dependent diffracted signal in ultrafast photoacoustics experiments to detect micro-gratings buried underneath opaque layers. As we found that the pump-pulse fluence is an important parameter in our experiments we used two different lasers with accompanying setups, one for low-fluence experiments (LFE), the other for high-fluence experiments (HFE). For our experiments, 6 µm period, 50 % duty cycle gold (Au) gratings were fabricated on top of a single metal layer deposited on glass. A 400 nm wavelength pump pulse generates ultrahigh-frequency longitudinal acoustic waves near the glass/metal interface which travel deeper into the Au and reflect off the grating. The topography of the grating is thus encoded on the phase of the acoustic wave and is detected at the glass/metal interface by diffraction of a 800 nm wavelength probe pulse. Surprisingly, we find that the signals measured in the two setups look very different, even though experiments were performed on the same sample. For example, despite the fact that in both cases the timing of the acoustic peaks is more or less the same, the signals measured in the HFE are all positive, while the signals measured in the LFE periodically drop below the background level. We show that these and other observations can be explained by the presence of a coherent optical field caused by scattering due to interface roughness which interferes with the optical field diffracted off the acoustic wave-induced gratings. For the right optical phase difference, the relatively strong background field can enhance

(coherently amplify) the weak field diffracted by the acoustic wave-induced grating. Our experiments are in excellent agreement with numerical simulations which can predict the exact shape of the signals measured both in the HFE and in the LFE. Our results show the importance of interface/surface roughness in understanding the results obtained using a low fluence, high repetition rate femtosecond laser for ultrafast photo-acoustic detection of nano-structures buried below optically opaque layers.

## 4.2 Sample fabrication and optical setups

Samples were made by first depositing a flat metallic layer on a glass substrate, followed by fabrication of a grating on top of the metallic layer. By performing the pump-probe measurement from the glass side, the grating is optically invisible to both the pump and the probe pulses and can be considered "buried". This can be seen in the inset of Fig. 4.1. All the samples were made on chemically cleaned 176 µm thick glass substrates. The gold (Au) layers were deposited by thermal evaporation. All gratings employed in the experiments were fabricated using UV lithography. Each grating has a period of 6 µm, a 50 % duty cycle and an amplitude of 10 nm. The three samples employed in this work only differ in the thickness of the flat Au layer, (85, 141 and 522 nm).

Our experiments were performed in a pump-probe setup shown in Fig. 4.1. Two different setups were used, employing a low fluence laser system and a high fluence laser system. We define the fluence of the laser system as the ratio between the pulse energy and the focal spot of the beam. The first setup is built around a low fluence Ti:Sapphire laser which generates 70 fs pulses at a high repetition rate of 5.1 MHz. Here the pump beam has a diameter of 50 µm on the sample and a pulse energy ranging from 8 nJ to 15 nJ, depending on the experiment. The probe has a diameter of 40 µm on the sample and its pulse energy was kept constant at approximately 12 nJ. The pulse energies generated by this system are relatively low and we will refer to experiments performed with this laser as low-fluence experiments, or LFE.

The second is built around a high fluence, amplified Ti:Sapphire laser which generates 30 fs pulses at a low repetition rate of 1 kHz. Here, the pump diameter is approximately 500 µm and pump pulse energies range

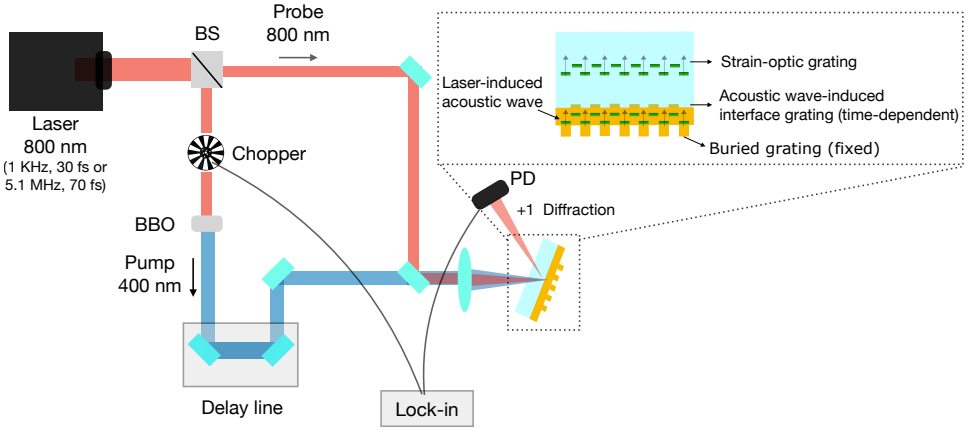


Figure 4.1: Schematic of the two experimental setups. In both setups, a pump-probe scheme was employed. The output from a 1 kHz or 5.1 MHz repetition rate Ti:sapphire laser with a central wavelength of 800 nm is split into two parts. One beam (pump) is frequency doubled to a wavelength of 400 nm by a BBO crystal and modulated by a mechanical chopper at 6 kHz. The other beam (probe) has a central wavelength of 800 nm. The pump-induced first-order diffracted probe beam is measured by a silicon photodiode. The photodiode has a bandwidth of 50 kHz. For the LFE, the photodiode signal is sent to a lock-in amplifier, which uses a reference signal from the chopper. We show in the inset a schematic of the sample. We pump and probe from the glass side. Thus, the measured total diffracted signal is due to diffraction off the interface grating and off the strain-optic gratings in glass.

from 6 µJ to 8 µJ depending on the sample. The probe has a diameter of 250 µm on the sample and the probe pulse energy was kept constant at 2 µJ. The pulse energies generated by this system are higher and we will refer to experiments performed with this laser as high-fluence experiments, or HFE.

In both setups, the 800 nm wavelength output is split in two parts. The stronger arm is frequency-doubled to generate 400 nm wavelength pulses and is used as pump beam. The weaker arm is time-delayed using an optical delay line formed by a retroreflecting pair of mirrors mounted on a mechanical translation stage, and is used as probe beam.

We would like to point out that in wafer alignment applications, the pump fluence is often maximized to values just below the damage thresh-

old to maximize the strength of the diffraction signal. In principle, both high and low fluences can be obtained with one laser, by simply changing the focal diameter of the beam. However, there are two reasons why we nonetheless have used two different laser systems in these experiments. The first is that the highest fluence that we can obtain with the low-fluence, high-repetition-rate system is limited by thermal damage, preventing us from reaching the fluence levels reached in the HFE. The second is that, whereas it is tempting to think that the HFE is better than the LFE because it can generate stronger acoustic waves, the sensitivity with which these waves can be detected is limited compared to what is possible in the LFE. The reason for this is that in the LFE the much higher repetition rate of the laser (5.1 MHz) allows for laser amplitude modulation at frequencies (we use 6 kHz) where lock-in amplification of the electronic signal from the photodiode detector can significantly enhance the detection sensitivity. In the end, for wafer alignment applications in the semiconductor manufacturing industry, sensitivity is of paramount importance. However, even without additional contributions to the detected light, such as light scattering by surface roughness, it would be nontrivial to predict a priori which system is best for alignment applications. As we will show below, light scattering by surface roughness can occur, it interferes with the light diffracted by acoustic-wave-induced gratings, and the extent to which it thus influences the time-dependent shape of the photoacoustic signals depends on the pump fluence.

Finally, we note that in both HFE and LFE, it is expected that the frequency of the generated sound waves neither depends on the fluence, nor on the repetition rate of the laser. The shape and, thus, the frequency contents of the sound wave is primarily determined by the diffusion depth of the electron-energy, which is the same for both LFE and HFE.

## 4.3 Experimental results

In Figs. 4.2(a) and 4.3(a) (green curves, top panels) we plot the diffracted probe beam signal as a function of the pump-probe delay, measured for the Au grating fabricated on a 85 nm thick Au layer for the LFE and HFE, respectively. In both setups, the signal is first composed of a sharp peak at zero delay. This peak is the result of a grating in the electron temperature

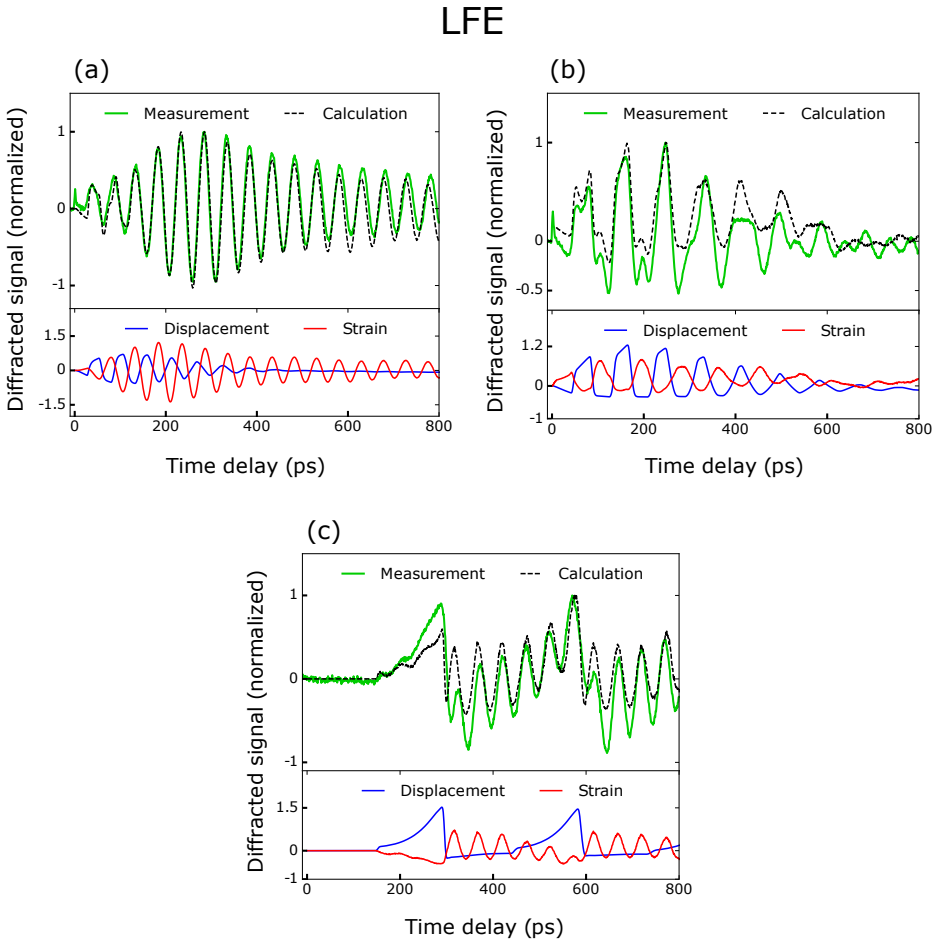


Figure 4.2: Diffracted probe beam signal measured for the 50 % duty-cycle, 10 nm amplitude Au gratings in the LFE. Top panels: experimental results (green curves) and calculated total signal (dashed black curves). Bottom panels: numerical calculations of the diffracted signals taking into account *only* surface displacement at the glass/Au interface (blue curves) or *only* diffraction from the acoustic waves in glass (red curves). We show the results for: Au grating fabricated on a (a) 85 nm Au layer, (b) a 141 nm Au layer and (c) a 522 nm Au layer.

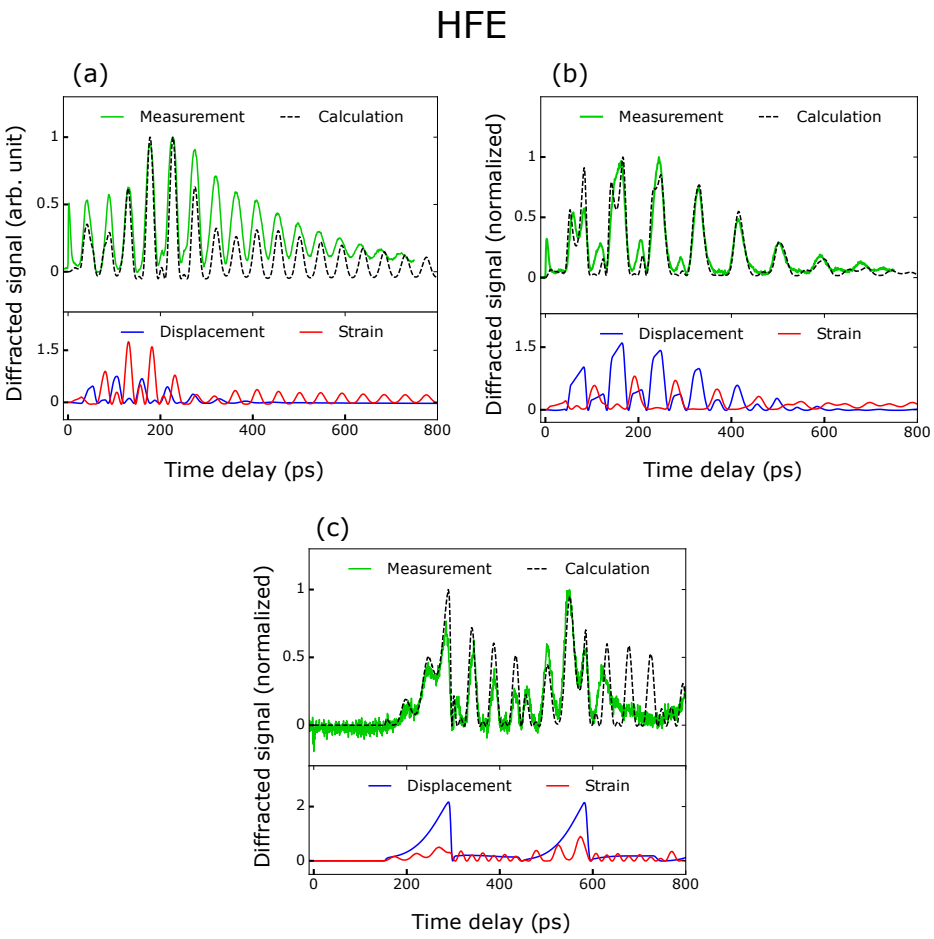


Figure 4.3: Same as Fig. 4.2 but measured in the HFE.

near the glass/Au interface which leads to diffraction of the probe beam and has been measured before [85]. A few tens of picoseconds later, an oscillatory signal with a period of $50 \pm 2$ ps is observed. The oscillation appears to last several hundreds of picoseconds for the measurements performed with the LFE (green curve in Fig. 4.2(a)) measurement, while it decays faster for the HFE (green curve in Fig. 4.3(a)). A first observation is that the signal shapes measured in the two setups are remarkably different in spite of the fact that both signals were obtained by measuring on the same sample. In particular, we observe "negative" values for the diffracted signal measured in the LFE.

In Figs. 4.2(b) and 4.3(b) (green curves, top panels) we show the measurements for the 50 % duty-cycle grating fabricated on a 141 nm thick Au layer. As before, a small hot electron dynamics peak at zero time delay is observed. Here, the strength of the electron dynamics signal is smaller than for the grating fabricated on a 85 nm Au layer, since the electron gas temperature grating is weaker for thicker Au layers [85]. A few tens of picoseconds later, an oscillatory signal with a period of $80 \pm 2$ ps is seen. Compared to the previous measurements, the oscillation appears to decay faster in both the LFE and HFE. Here too, we observe "negative" values for the diffracted signal for the LFE (green curve in Fig. 4.2(b)).

In Figs. 4.2(c) and 4.3(c) (green curves, top panels) we show the measurements for the 50 % duty-cycle grating fabricated on a 522 nm thick Au layer. Here, the electronic peak around delay zero is not detected. For the first 170 ps no diffracted signal is observed. After this, a diffracted signal can be seen, which rises to a maximum at a delay of $285 \pm 2$ ps. A second peak is seen around $570 \pm 2$ ps time delay. A faster oscillating signal is superimposed on top of the acoustic echoes with a period of about $50 \pm 2$ ps. As before, we observe "negative" values for the diffracted signal for the LFE (green curve in Fig. 4.2(c)).

A somewhat unexpected observation we made during the experiments in the LFE on the 522 nm Au sample, is that the amplitude of the measured signal varies when measuring on different spots on the same sample. Moreover, the signal can even change sign, as if multiplied by $\approx$ -1. We will explain this in more detail in section 4.5. This behaviour is absent for the measurements taken in the HFE, where intensity variations were seen of only 10-20 %.

In a series of measurements, we recorded the diffracted signal at different positions above the buried grating fabricated on the 522 nm thick Au layer. The thickest sample was chosen here to avoid any effects which could arise from direct optical diffraction from the buried grating. Taking the 13 nm penetration depth of the 800 nm light into account, and in view of the small signals that we measure, this cannot a priori be excluded for the thinnest 85 nm thick sample. We first measured the diffracted signal on one particular spot, which we consider the "zero position" ($x_0$) (Fig. 4.4(a), top panel). When the sample is horizontally translated, in the direction perpendicular to the grating's lines, by 50 µm (Fig. 4.4(a), bottom panel), corresponding to the diameter of the probe beam, or more, the measured signal can change sign compared to the measurement at the previous position. A similar observation is made when we move the sample 50 µm in the vertical direction, parallel to the grating lines, as shown in Figs. 4.4(b).

We note, however, that the signals plotted in Figs. 4.4(a) and (b) were chosen precisely because in these cases, when the sample was moved, the signals flipped sign. To investigate whether these changes were random or not, we also performed a scan of the sample by recording the diffracted signal while moving the sample in steps of 50 µm, in both horizontal and vertical directions. In Fig. 4.5(a) we plot the strength of the first diffraction peak (corresponding to a time delay of 285 ps) as a function of the position on the sample. The red dots represent the horizontal scan, where the first data point correspond to the "zero position" ($x_0$). The blue dots represent the vertical scan, where the first data point correspond to the position $y_0$. The path followed during the scan is shown with the coloured arrows in the inset (Fig. 4.5(b)). We can clearly see from this plot that the sign and amplitude of the signal seems to vary quite randomly.

When scanning in the area corresponding to the intersection between the horizontal and the vertical scans, a stronger variation in the intensity of the diffracted signal is detected. This increase is most likely due to the presence of dust particles trapped between the Au layer and the glass substrate, as observed with a microscope camera. The dust particles give rise to an increased amount of scattered light [86]. As we will discuss below, the results for the LFE can only be explained by taking the optical interference between the field diffracted by the acoustic wave-induced interface grating, the strain-optic grating propagating in glass and an *additional* background

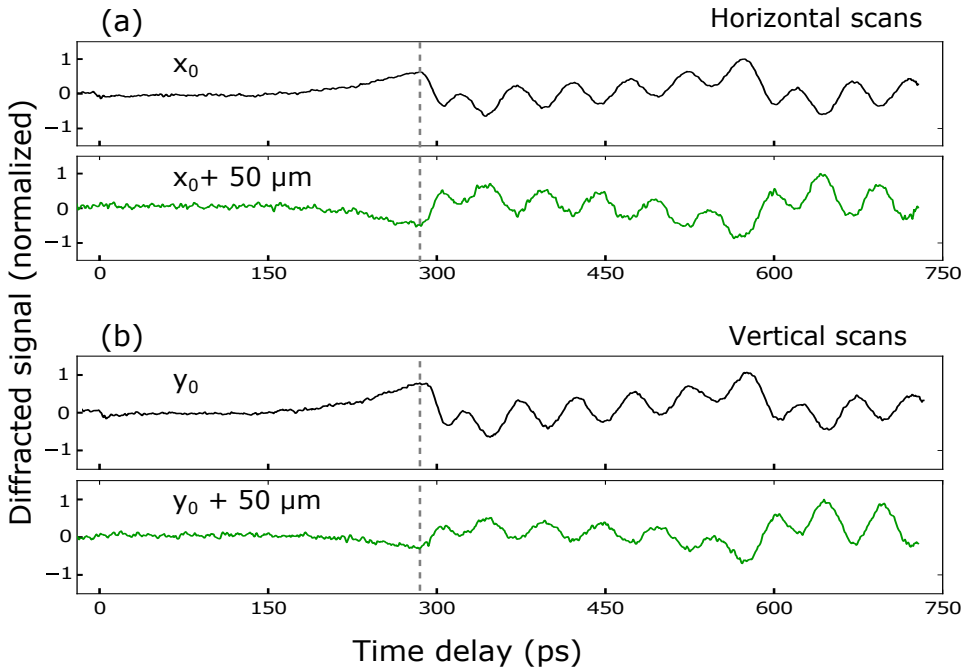


Figure 4.4: Diffracted signal recorded at different positions above the buried grating fabricated on the 522 nm thick Au layer. (a) Shows the two extreme cases, where a flip in sign is observed during the horizontal scan of the sample. (b) Shows the same for the vertical scan.

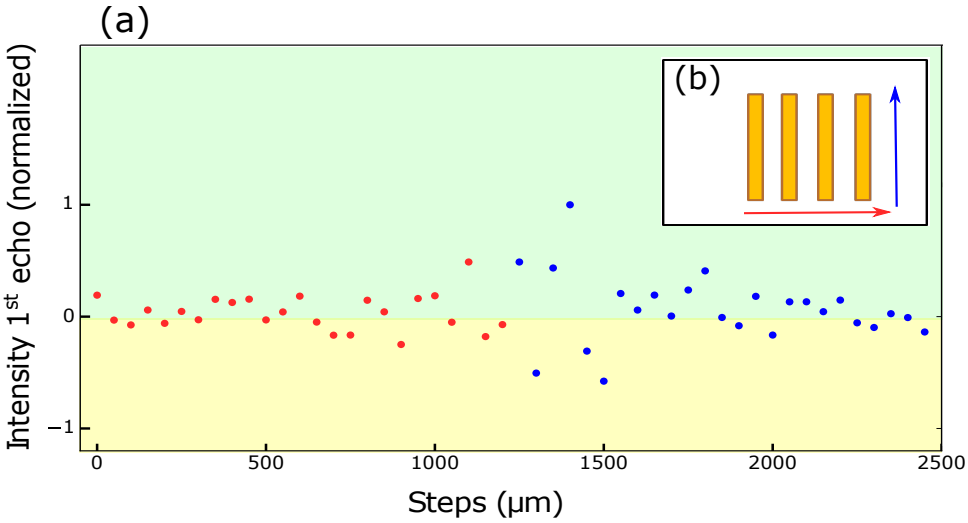


Figure 4.5: (a) Intensity of the first echo (corresponding to a time delay of 285 ps) as a function of the position on the sample. The red dots represent the horizontal scan and the blue dots the vertical scan. The yellow area contains the negative values, while the green one contains the positive values. The path followed during the scan is schematically shown with the coloured arrows in the inset (b).

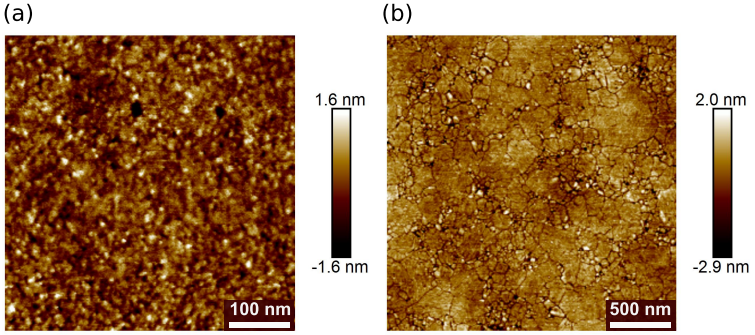


Figure 4.6: (a) AFM measurement on the glass side of the interface glass/Au. The roughness is 0.45 nm (RMS value). (b) AFM measurement on the Au side of the interface glass/Au. The roughness is 0.60 nm (RMS value). When deposited on a smooth substrate, the Au tend to follow the topography of the substrate. Therefore, the measured roughness values for glass and Au are in reasonable agreement.

field into account. The most likely source of this field is optical scattering by the roughness of the metal film at the glass/Au interface.

Reflection of light from rough surfaces has been used in the past for characterisation of surface topography [87–90]. Scattering from surfaces with a root-mean-square roughness amplitude in the range of a few nm, was measured before [89]. In order to measure the roughness of the Au layer at the glass/metal interface, the Au layer was peeled from the glass substrate by using standard tape in order to obtain a *free standing* Au surface. In this way, we were able to measure roughness on both the Au side and the glass side of the interface. It is well known that thin Au films have a weak adhesion to inert and commonly used glass substrates [91]. Therefore, by applying a piece of tape onto the sample, it was easy to completely peel the Au layer from the substrate. An Atomic Force Microscopy (AFM) measurement of this layer was then performed. For comparison, an AFM measurement was also performed on the glass surface. In Fig. 4.6(a) and (b) we show the AFM results for the two surfaces. We measure a RMS roughness value, $R_q$, with values of $R_q = 0.60$ nm for Au and of $R_q = 0.45$ nm for the glass substrate. The two values are in reasonable agreement. Basically, the roughness of the substrate translates into a similar roughness for the deposited metal layer, although the two surfaces look different. In fact, the evaporated Au has a polycrystalline nature, while the glass is an amorphous material. The RMS amplitude roughness of the interface is small and thus gives rise to a weak background field only. However, the amplitude of this field is within an order of magnitude of the amplitude of the field diffracted by the acoustic-wave-induced grating as we will show later. This means that interference between the two fields can have a significant effect on the amplitude and shape of the time-dependent diffraction signals.

## 4.4 Results of the numerical calculations

To better understand our measurements, numerical calculations were performed. The 2D numerical model we used was developed by H. Zhang et al. [92]. It takes into account all the steps involved in a typical photoacoustic experiment, such as generation, propagation and detection of the acoustic waves. As for the detection part, diffraction of light off the acous-

tic wave-induced interface grating at the glass/metal interface, and off the acoustic grating propagating inside the glass (strain-optic scattering [93]) were both taken into account. In separate photo-acoustic experiment on simple, flat gold layers, material parameters were extracted by fitting the model to the measurements. The same parameter values were then used to fit the model to the measurements shown in Figs. 4.2 and 4.3. The fitting procedure used to extract the material parameters for the single flat gold layers is extensively described in [92]. In the LFE case, a relatively strong constant optical field is added to the diffracted fields off the acoustic gratings before the calculation of the diffraction efficiency, representing the background field present in our experiments.

In Figs. 4.2 and 4.3 (black dashed curves), we plot the diffracted signals, calculated for the 10 nm Au gratings on a 85, 141 and 522 nm thick Au layer measured in both the LFE and the HFE, respectively. Parameters were manually adjusted until the best fit between the measurements and the calculations was obtained and kept constant for both the setups.

In Figs. 4.2(a) and 4.3(a), the calculations show long-lasting oscillating signals with a period of about 50 ps for the grating fabricated on the 85 nm thick Au layer. The calculations are in good agreement with the experimental results. In the bottom panels of Figs. 4.2(a) and 4.3(a), we plot the calculated diffracted signal from only the displacement at the glass/Au interface (blue curve) and from only the strain-optic grating propagating inside the glass (red curve). The latter effect can be viewed as diffraction from spatially periodic changes in the material density induced by the propagating, spatially periodic sound wave. This leads to a spatially periodic, propagating, transient variation of the refractive index of the glass. Such a propagating, spatially periodic refractive index constitutes a grating from which the probe can diffract. The calculated curves clearly show that the signal is dominated by the latter contribution.

In Figs. 4.2(b) and 4.3(b) (black dashed curves), we plot the diffracted signals, calculated for the grating on the 141 nm thick Au layer. The calculations also show oscillating signals with a period of approximately 80 ps, in good agreement with the measured signals. There is some mismatch between the measured and calculated diffraction signal strength, especially for longer delays. In the bottom panels of Figs. 4.2(b) and 4.3(b), we plot again the calculated diffracted signals from *only* surface displacement

(blue curve), and from *only* the strain-optic grating propagating inside the glass (red curve). In contrast to the calculations shown for the 85 nm thick Au layer, here we find that the displacement of the atoms at the glass/Au interface provides the strongest contribution to the measured signals.

In Figs. 4.2(c) and 4.3(c) (black dashed curves), we plot the diffracted signals, calculated for the 522 nm thick Au layer. The calculations show oscillating signals with a period of approximately 285 ps, in good agreement with the measured signals. In the bottom panels of Figs. 4.2(c) and 4.3(c), we plot again the calculated diffracted signals from only the acoustic wave-induced interface grating (blue curve), and from only the strain-optic grating propagating inside the glass (red curve). Note that for this sample, the bigger spacing between the two echoes allows us to identify both contributions in the measurements more easily. The strain-optic contribution appears as a faster oscillating signal superimposed on top of the acoustic wave-induced interface displacement signal. To simulate the signals measured, a relatively strong constant optical field was added along the first order diffraction direction, representing the background field present in our experiments. For consistency, the value of the background field was kept the same for the two systems. It has a constant value, corresponding to an intensity on the detector, $I_D$, which is a fraction of the intensity incident on the sample, $I_{INC}$. Here we have $I_D/I_{INC} = 5 \times 10^{-9}$, for all three samples.

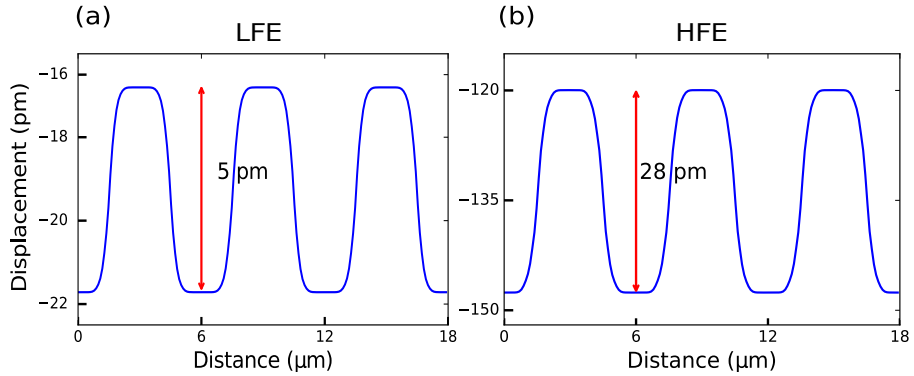


Figure 4.7: Displacement at the glass/Au interface for the 522 nm sample, calculated at a delay of 285 ps, as a function of the position along the direction perpendicular to the grating lines in the (a) LFE and (b) HFE.

To estimate typical surface displacement amplitudes near the glass/Au

interface, we plot in Fig. 4.7 the calculated displacement of the interface for the 10 nm grating fabricated on a 522 nm thick Au layer, calculated at a pump-probe delay of 285 ps delay, corresponding to the arrival time of the first echo (indicated by the grey dashed line in Fig. 4.4(a) and (b)). 285 ps is the time at which the diffracted signal due to the displacement is found to be the largest in the calculations. At this time delay, the acoustic wave has completed one round trip inside the 522 nm Au, and the grating-shaped displacement at the glass-Au interface has the same phase as the buried grating. Here, three unit cells are shown, where one unit cell has a width of 6 µm. Fig. 4.7(a) shows the interface displacement profile calculated using the LFE parameters and Fig. 4.7(b) the HFE parameters. In both figures, the displacement profile is superimposed on the expansion of the whole Au layer due to heating, which explains the negative offset in the displacement values. However, only the grating-shaped interface displacement profile contributes to the diffraction efficiency. We obtain a peak-to-valley amplitude of the acoustic wave-induced interface grating value of 5 pm for the LFE. For the HFE, where the pump fluence is more than five times bigger then the LFE, the peak-to-valley amplitude of the acoustic wave-induced grating at the interface glass/Au is 28 pm.

## 4.5 Discussion

### 4.5.1 Acoustic wave generation in Au

Time-resolved measurements of transient reflectivities on thin Au layers as a function of layer thickness have been described before [59, 60, 94]. The thickness of the Au layer, however, also plays a role in the acoustic wave generation mechanism. While for the thinner Au layers (85 and 141 nm), the whole layer is rapidly and homogeneously heated up, for the thicker Au layer (522 nm) this is no longer the case. Instead, the acoustic wave generated within a finite depth of about 200 - 300 nm from the interface will propagate into the material until it reaches the buried grating at the Au/air interface. Here, the acoustic wave is reflected back with a delay between the part reflected off the valleys and the ridges of the grating. As a result, the acoustic wavefront becomes spatially modulated. The arrival time of the first echo corresponds roughly to the round-trip time in the 522

nm thick Au layer. It can be calculated as $T = 2l/v$, where $l$ is the layer thickness and $v$ is the speed of sound in the metal. Assuming a longitudinal velocity of 3.2 km/s [53], the round-trip time is expected to be $\approx$ 303 ps. Finally, once the reflected acoustic wave reaches the glass/Au interface, it displaces the Au atoms in a spatially periodic manner. We can detect this grating by diffraction of a probe pulse.

As we can see from the simulations shown in Figs. 4.2 and 4.3 (bottom panels) the total diffracted signal predominantly consists of two different contributions. The blue curves represent the diffracted probe beam from the acoustic wave-induced interface grating at the glass/Au interface. The red curves, instead, represent optical diffraction from the strain-optic wave that has partially entered the glass and continues to propagate [44, 92, 93, 95–97]. The total oscillatory signal is due to the interference between the different contributions to the diffracted signal. These include, for example, the background optical field, the probe beam diffracting off the strain-optic grating propagating in the glass, and the transmitted probe beam reflecting back at the glass/metal interface and diffracting again from the strain-optic gratings in glass. As was pointed out in [97], the latter is also often referred to as Brillouin scattering. The period of this oscillation is given by $T = \lambda/(2nvcos\theta)$ [93]. Here, $\lambda$ is the probe wavelength, $n$ is the refractive index of the glass at this wavelength, $v$ is the speed of sound in glass, and $\theta$ is the angle of incidence, measured inside the glass. For glass, $v \approx 5.7$ km/s and $n = 1.5$. In our experiments, $\theta$=14.5° inside the glass for the LFE and $\theta$=2.0° in the HFE. We then obtain an oscillation period of 50.4 ps for the measurements in the LFE and of 46.7 ps for the measurements taken in the HFE. This period is close to the period of the acoustic oscillations for the grating fabricated on 85 nm Au of $50 \pm 2$ ps for the LFE (see Fig. 4.2(a)) and of $46 \pm 2$ ps for the HFE (see Fig. 4.3(a)). The contribution from the strain-optic effect in the glass is weaker for the measurements on the 141 nm and 522 nm thick Au layers (see Figs. 4.2 and 4.3, (b) to (c)). For the grating fabricated on 522 nm thick Au, the contribution due to the strain-optic effect is a more clearly visible lower amplitude oscillation superimposed on the slower acoustic wave-induced displacement diffraction peaks (see Figs. 4.2(c) and 4.3(c)).

### 4.5.2 "Negative" diffracted signals: background optical fields

The clearest difference between measurements taken in the HFE and in the LFE is that in the first case the measured diffracted signal is all positive, while in the latter it drops below the background level seen at negative delays. This can only be explained if we can assume that *another*, coherent scattered optical field is present, which interferes with the field diffracted by the acoustic wave. Heterodyning of a weak optical field is a widely used technique to improve the sensitivity to small signals. It is achieved by applying on the same photodetector an additional optical field of higher amplitude. The interference between the two fields leads to amplification of the weak field. The source of the second stronger field can be the same laser source [43], a second laser beam [98] but also light scattered from reflecting interfaces of the sample [44, 97].

The optical phase difference between the two diffracted fields will determine the extent to which the interference is constructive/destructive. For illustrative purposes only, we will assume that the acoustic wave gives rise to only *one* diffracted field at a time. Denoting the additional background diffracted optical electric field $E_b e^{i(\omega t - \vec{k}\cdot\vec{r})}$, the field diffracted by the acoustic wave $E_{ac} e^{i(\omega t - \vec{k}\cdot\vec{r} + \phi)}$, and the sum of the two fields $E_{tot} = E_b e^{i(\omega t - \vec{k}\cdot\vec{r})} + E_{ac} e^{i(\omega t - \vec{k}\cdot\vec{r} + \phi)}$, we can write for the total optical power $S$ incident on the Si detector,

$$S \propto |E_{tot}|^2 = E_b^2 + E_{ac}^2 + 2E_b E_{ac} \cos(\phi), \tag{4.1}$$

where $\phi$ is a pump-probe delay-dependent difference in phase between the two fields, and where we have suppressed the time dependence of the amplitudes. It is important to realise that in the LFE the pump pulse train is modulated with a mechanical chopper. Lock-in detection ensures that probe signal components on the detector which are *not* modulated by the pump beam will be removed by the lock-in amplifier. This means that, in principle, only terms containing $E_{ac}$ in Eq. (4.1) are observed in our measurements. When the background optical field amplitude $E_b$ is constant and has an amplitude much bigger than the field diffracted by the acoustic wave $E_{ac}$ ($E_b \gg E_{ac}$), the $E_b^2$ term in Eq. (4.1) serves as a constant background signal level around which the $2E_b E_{ac} \cos(\phi)$ term oscillates when $\phi$ periodically changes. Lock-in detection ensures that $E_b^2$ is not directly

observed and that when the coherent sum of the two fields drops below the background field strength, this is seen as a negative signal.

The above description of the effect of the background optical electric field gives a plausible physical explanation for the observation that the diffracted signals drop below the level seen for negative delays. However, it ignores the fact that, as we explained in section 4.5.1, every time the acoustic wave reaches the glass/metal interface, part of the wave is periodically transmitted into the glass where each acoustic wave also gives rise to an additional time-dependent diffraction signal. This means that in reality, the field $E_{ac}$ is composed of several contributions, $E_{ac_k}e^{i\phi_k}$ (k=1,2,..), each with a different amplitude $E_{ac_k}$ and a time-dependent phase difference $\phi_k$ with respect to the background field $E_b$. Fortunately, using the full numerical model to describe the generation, propagation and optical detection of the acoustic waves, all these waves are automatically taken into account, as mentioned before.

The optical phase difference between the two diffracted fields will determine whether the interference is constructive or destructive. Destructive interference leads to less light on the detector which, after lock-in amplification, manifests itself as a negative signal. There are several possible sources of background light in our experiments, which we will discuss next, schematically represented in Fig. 4.8.

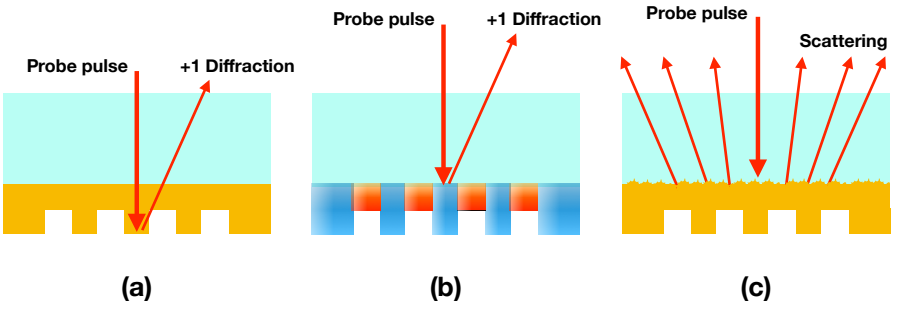


Figure 4.8: Schematic representation of the possible sources of background light in our experiments. (a) Direct optical diffraction from the buried grating. (b) Optical diffraction from thermal grating. (c) Scattering by interface roughness.

A. *Direct optical diffraction from the buried grating.*

In principle, for thin layers of Au (thickness < 100 nm), probe light could still penetrate the layer and diffract off the buried grating (see Fig. 4.8A). This diffracted light travels back again through the layer producing a background field on the detector. This may seem surprising in view of the penetration depth of 800 nm light in Au (approx. 13 nm [59]). For such a penetration depth, after traversing the Au layer twice, the signal attenuation would lead to only a weak diffracted signal. For the 141 nm and especially for the 522 nm samples, direct optical diffraction off the buried gratings becomes vanishingly small and is thus unlikely to be the source of the background field. Moreover, direct optical diffraction is unlikely to be the cause of the background field. Fig. 4.5(a) clearly shows the random nature of the sign and amplitude of the diffracted signals when the sample is scanned in the $x$ and $y$ directions. This randomness is caused by a random difference between the phase of light diffracted by the acoustic wave-induced grating and the background optical field. As the light directly diffracted off the buried grating would always have the same phase as the acoustic wave-induced interface grating, the optical phase difference between the light diffracted by both gratings would not change.

B. *Optical diffraction from thermal grating.*

When the pump pulse energy is deposited into the material, a thermal grating can be created due to the presence of the buried grating, which gives rise to a periodic variation in Au thickness. As shown in Fig. 4.8B, the areas above the valleys of the grating, where the total metal thickness is the lowest, will reach a higher lattice temperature. The areas above the ridges of the grating will have a lower lattice temperature. The initial amplitude of this temperature grating at the interface, $\Delta T$, is thus determined by the difference between the temperatures above the valleys and the ridges of the grating. Heating of the layer leads to changes in the complex dielectric function of the metal. A grating in the temperature thus leads to a grating in the dielectric function. From this grating, a probe pulse can be diffracted. In the LFE, the high repetition rate of the system may lead to a cumulative effect so that, when the next probe pulse arrives

at the interface, the energy deposited in the metal layer by the previous pump pulse has not yet completely dissipated into the substrate and/or has not been completely washed out by lateral heat diffusion. Thus, a weak quasi-static thermal grating could be present at the interface which will diffract the probe pulse. However, also diffraction by a thermal grating is unlikely to be the cause of the background field, as a thermal grating would always have the same phase as the acoustic wave-induced interface grating and would thus not give rise to the strong, random position dependence seen in our measurement. This is supported by our observation that the background field is also clearly present for the gratings on thicker Au layers (522 nm). For this layer, the thickness difference above the valleys and the ridges of the 10 nm amplitude grating becomes relatively small and is thus less likely to lead to a thermal grating. We note that the absence of a thermal grating in our experiments may be a consequence of the modestly high repetition rate of our LFE of 5.1 MHz. Often, mode locked lasers have a repetition rate of 75 to 100 MHz, which would make thermal gratings more likely as there is less time for the heat to diffuse into the substrate during the time between two laser pulses.

C. *Scattering by interface roughness.*

The sign change of the measured diffracted signals as a function of the position of the probe beam onto the sample (see Section 4.3) can only be explained in relation to the nature of the glass/Au interface. The Au layers on which our gratings are fabricated were deposited by thermal evaporation. This technique generates poly-crystalline Au layers with a more or less random distribution of Au crystal sizes and orientations [99]. This means that, as shown in Fig. 4.6 and discussed in section 4.3, the glass/metal interface has a certain roughness of $R_q = 0.60$ nm, which is about two order of magnitude larger than the amplitude of the acoustic wave-induced interface grating. Rough surfaces, however, scatter light into all directions (see Fig. 4.8C), whereas a grating, even when its amplitude is considerably smaller than the roughness, diffracts and thus confines light into a few particular diffraction orders only. Nevertheless, a significant background signal was observed in our setup. The light scattered from the surface will have a random phase [100]. Moreover, since roughness has a random character,

the scattered light will have a different phase when the interface is illuminated at different positions. This is why our probe beam can detect these phase changes only when the sample is translated over a sufficiently large distance to "see" a statistically different area of the sample. The difference in phase between the two optical fields varies in a random fashion when the beam illuminates different areas, and thus so does the interference between the fields scattered by these two sources.

### 4.5.3 Comparison between LFE and HFE

Now that we understand why the signals measured in the LFE and in the HFE are different, a comparison between the results obtained in the two different setups can be made. We assume the background scattered field amplitude to be time-independent in both setups. Suppose that $\eta_s$ is the efficiency with which the surface roughness scatters the incident probe light onto the detector. The efficiency $\eta_{gr}$, with which the acoustic wave-induced grating diffracts the incident probe light, depends on the square of the amplitude $u$ of the grating which, in turn, scales linearly with the pump fluence $F_{pu}$,

$$\eta_{gr} \propto u^2 = CF_{pu}^2, \tag{4.2}$$

with $C$ a constant of proportionality. The ratio of the two can be written as,

$$\frac{\eta_{gr}}{\eta_s} = \frac{CF_{pu}^2}{\eta_s}. \tag{4.3}$$

Since $\eta_s$ is independent of the pump fluence, this equation clearly shows that the ratio of the light diffracted by the grating and the light scattered by the surface roughness, scales with the square of the pump fluence. Thus, for increasing pump fluence diffraction by the grating increases relative to scattering by surface roughness.

The difference in the calculated acoustic grating amplitude for the 522 nm sample in the LFE and in the HFE (shown in Fig. 4.7) can be estimated by comparing the fluence of the pump beams for the two different setups. The fluence used for this particular sample is approximately $7 \pm 1$ J/m$^2$ in the LFE and $35 \pm 3$ J/m$^2$ in the HFE, giving a ratio of about 5. The ratio

between the amplitudes of the acoustic wave calculated for the HFE and in the LFE is $\approx 5.6$, close to the ratio between the two fluences. Taking Eq. 4.5.3 into account, the latter number leads to a diffraction efficiency (ignoring the background optical field) of $\eta_{HFE} \approx 31\eta_{LFE}$. Using the expression for the diffraction efficiency of a binary grating [66], we calculate the diffraction efficiencies of acoustic wave-induced gratings at the interfaces of the three samples used in this work to be in the order of $\approx 10^{-7}$ for the HFE and $\approx 10^{-9}$ for the LFE. Thus, we can conclude that the background signal (surface roughness scattering efficiency of $5\text{x}10^{-9}$) strongly shapes the measured signals in the LFE, while it can be neglected in the HFE.

In general, it is difficult to predict which system is better for the detection of buried gratings using laser-induced ultrasound. High fluence, low-repetition rate lasers are capable of generating strong ultrasound pulses, but have relatively high pulse-to-pulse intensity fluctuations which leads to fluctuating signals and lower detection sensitivity. In addition, high fluences can more easily lead to optical damage when focusing the beam tightly onto the samples, which has to be avoided at all cost. Low fluence systems have smaller pulse-to-pulse fluctuations and the pulse train can be modulated, facilitating the use of lock-in detection schemes that enhance detection sensitivity. This may offset signal reduction due to the relatively low peak power of the pulse. However, these arguments implicitly assume that in both cases the detected signals are not significantly affected by the change in repetition rate and fluence, and that changing either only has an effect on signal strength. Our results show that this assumption no longer holds. This is due to the presence of light scattering by interface roughness which scales differently with laser power than the photoacoustic signal.

Despite the fact that in the HFE it is possible to generate stronger acoustic gratings at the glass/metal interface, from an application point of view the LFE may be a better candidate for the detection of periodic micro-structures buried underneath optically opaque materials. One of the advantages of using the LFE is that, due to the higher repetition rate of the laser, a good signal-to-noise ratio is achievable in less time. In our case, measuring with the LFE allowed us to reduce the acquisition time compared to the HFE. The presence of a strong static background field can attenuate the signal but can also, for the right optical phase difference between the diffracted and scattered fields, amplify the weak acoustic wave-

induced optical signals, making it easier to detect the hidden structures.

## 4.6 Summary

We have shown that different femtosecond laser systems can be used to generate ultrahigh frequency acoustic waves for the detection of periodic microstructures buried underneath optically opaque layers. In our experiments, diffraction from the "acoustic replica" of the gratings at the glass/metal interface has been measured. We observe that the shapes of the signals measured in the LFE and in the HFE are remarkably different despite the fact that the signals were obtained by measuring on the same sample. This observation can be explained by the presence of a coherent background optical field due to scattering from the interface roughness at the glass/Au interface. In the LFE, this background optical field is significantly stronger than the strength of the optical field diffracted by the acoustic wave. Interference between the two changes the shape of the diffracted signal as a function of the pump-probe time delay and can cause the signal to drop below the level observed at negative delays when the interference is destructive. In spite of the smaller amplitude of the acoustic grating induced with the LFE, the high repetition rate of the laser system allows us to improve the signal-to-noise ratio, reducing the acquisition time.

# 5 Photoacoustic detection of low duty cycle gratings through optically opaque layers ⋆

In this Chapter we report on the use of ultra-high frequency photo-acoustics to detect gratings with line widths as narrow as 75 nm, buried underneath optically opaque metal layers. In our experiments we use gratings fabricated on top of a metal layer on glass and we optically pump and probe the sample from the glass side. Our results show that buried gratings can be detected by observing diffraction from the spatially periodic acoustic replica of the buried grating at the glass/metal interface and from replicas of the acoustic wave inside the glass substrate. Surprisingly, the measured diffraction signals drop below the signal levels present for negative delays and show a linear dependence on grating duty cycle rather than the expected quadratic one. We find that this is due to the presence of a coherent background optical field which interferes with, and coherently amplifies the weaker fields diffracted off the grating-shaped acoustic waves. Our measurements show that ultra-high frequency photo-acoustics is a promising technique for detection of sub-wavelength periodic nanostructures.

⋆This chapter has been published in a slightly modified form as Appl. Phys. Lett. 117, 051104 (2020)

## 5.1 Introduction

We have showed how laser-induced ultrasound with frequencies of tens to hundreds of GHz can be used to detect gratings buried below optically opaque layers. The gratings, however, all had fairly large linewidths of 3 µm. Little is known about the ability of the technique to detect buried gratings with much narrower linewidths. In principle, ultra-high frequency acoustic waves can have wavelengths in the tens to hundreds of nanometer range, considerably shorter than the wavelengths of visible light, and should thus also be sensitive to the presence of very narrow grating lines.

Here, we show that ultrafast photo-acoustics can be used to detect low-duty cycle gratings, buried underneath an opaque layer, with duty cycles as low as 1.3 %, corresponding to a linewidth of 75 nm. For our experiments 6 µm period metal gratings with different duty cycles were fabricated on top of a single metal layer deposited on glass. Viewed from the glass side, the grating is essentially invisible and can be considered "buried". Ultrahigh-frequency sound waves, generated by a 400 nm pump pulse near the glass/metal interface, reflect off the buried grating and are detected at the same interface by diffraction of a 800 nm probe pulse. Surprisingly, we observe that the measured diffracted signals periodically drop below the background signal level and that the dependence of the diffracted signal strength on duty cycle shows a near-linear, rather than the expected quadratic dependence. We show that both these observations can be explained by the presence of a coherent background scattered/diffracted optical field which interferes with the optical fields diffracted off the acoustic-wave-induced grating. Our experiments are in excellent agreement with numerical simulations that take the generation, propagation, diffraction and optical detection of the acoustic waves into account. The results illustrate the potential of ultrafast photo-acoustics to detect nanostructures buried below optically opaque layers for the semiconductor device manufacturing industry.

## 5.2 Experimental setup and samples fabrication

Our experiments were performed using the pump-probe setup schematically shown in Fig. 3.6 in Chapter 3.

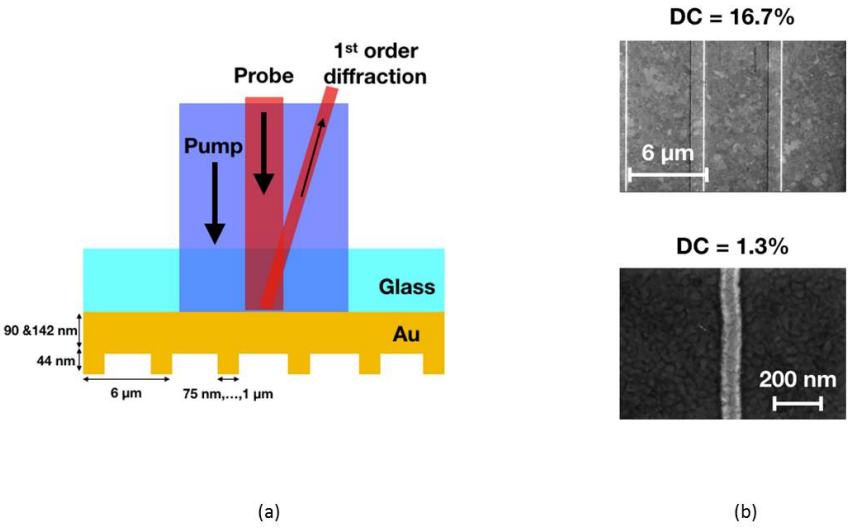


Figure 5.1: (a) Schematic of the sample geometry. A 400 nm pump pulse illuminates a Au layer from the glass side. A 800 nm probe pulse is diffracted from the "acoustic replica" of the buried grating at the glass/Au interface. (b) SEM images of the 16.7 % and 1.3 % duty cycle gratings, corresponding to 1 µm and 75 nm linewidths, respectively.

Our samples are fabricated by first depositing a flat gold (Au) layer on glass, followed by the fabrication of a grating, using e-beam lithography, on top of this layer. By now performing the pump-probe measurements from the glass side (Fig. 5.1(a)) the gratings are optically invisible to the laser pulses and can be considered "buried". Most importantly, since at this interface the Au is essentially flat, we avoid any residual topography grating which could lead to a relatively strong constant optical diffraction.

Two sets of five different Au gratings were fabricated, one set on a 90 nm thick flat Au layer, the the other on a 142 nm thick flat Au layer. All five gratings in a set have an amplitude of 44 nm, a period of 6 µm, but different duty cycles of 1.3 %, 2.1 %, 4.2 %, 8.3 % and 16.7 %, corresponding to ridge line widths of 75 nm, 125 nm, 250 nm, 500 nm and 1 µm, respectively. Scanning Electron Microscope (SEM) images of two gratings with linewidths of 1 µm and 75 nm are shown in Fig. 5.1(b). For comparison, we also fabricated a nickel (Ni) grating on a 200 nm thick flat Ni layer. The amplitude of this grating is 40 nm, the period is 6 µm and the duty cycle is 8.3 %, corresponding to a 500 nm linewidth.

## 5.3 Numerical calculations

In order to confirm that our interpretation of the measurements is correct, we also performed extensive calculations of the diffracted signal. For this, we use the numerical model developed by Hao Zhang et al. [92]. This is a 2D numerical model which contains all the steps involved in a typical photo-acoustic experiment, such as generation, propagation and detection of the acoustic waves. It also includes relaxational acoustic damping. In the model, equations are solved by the 2D Finite Difference Time-Domain (FDTD) method. The calculated diffraction signal is compared with the pump-probe experimental results. The temporal and spatial evolution of the lattice temperature is obtained using the well-known two-temperature model [56–59, 94], which acts as a source term in the equation of motion for the sound propagation. The model also includes diffraction of light off the displacement grating at the glass/metal interface, and off the acoustic grating propagating inside the glass by considering the strain-optic effect. In our case, a relatively strong constant optical field is also added to all diffracted fields, representing the background field present in our experi-

ments. The background field is presumably caused by light scattering due to interface roughness. This field is taken to be approximately two orders of magnitude stronger than the optical fields diffracted by the acoustic waves.

## 5.4 Results

In Fig. 5.2, we plot the first-order diffracted probe signal as a function of the delay between pump and probe pulses for the five Au gratings fabricated on a 90 nm thick Au layer. While performing these measurements, a significant variation of the diffracted signal strength was observed as a function of position on top of the buried grating. This variation is caused by interference with an optical field resulting from scattering by interface roughness. The phase of this scattered field is random, resulting in a variation of the signal with position. Therefore, for every sample, care was taken to choose a position on the sample where the signal is maximum. However, we point out that due to the statistical nature of the phase of the randomly scattered light, there is some uncertainty whether such a chosen maximum is an absolute maximum rather than a local maximum.

The signals shown in Fig. 5.2 are composed of a small sharp peak at zero delay for the 1 µm, 500 nm and 250 nm linewidth gratings. We were not able to resolve this peak for the 125 nm and 75 nm linewidth samples because of the reduced signal-to-noise ratio. This peak is the result of a grating in the electron temperature near the interface which leads to diffraction of the probe beam [85]. A few tens of picoseconds later, an oscillatory signal with a period of $50 \pm 2$ ps becomes apparent, lasting several hundreds of picoseconds. The amplitude of the oscillation decreases with the duty cycle of the gratings but, remarkably, a signal is still observed for the 1.3 % duty cycle grating where the lines are only 75 nm wide.

A surprising observation is that the diffracted signal drops below the signal level measured for negative time delays. The reason for this is that a background optical field, presumably caused by scattering of the probe electric field by surface roughness, is also present. As we will argue below, the probe electric field diffracted by the acoustic grating can destructively/constructively interfere with this background electric field, giving rise to an effective increase or decrease of the signal on the photodiode.

For comparison, we also performed measurements on a buried grating

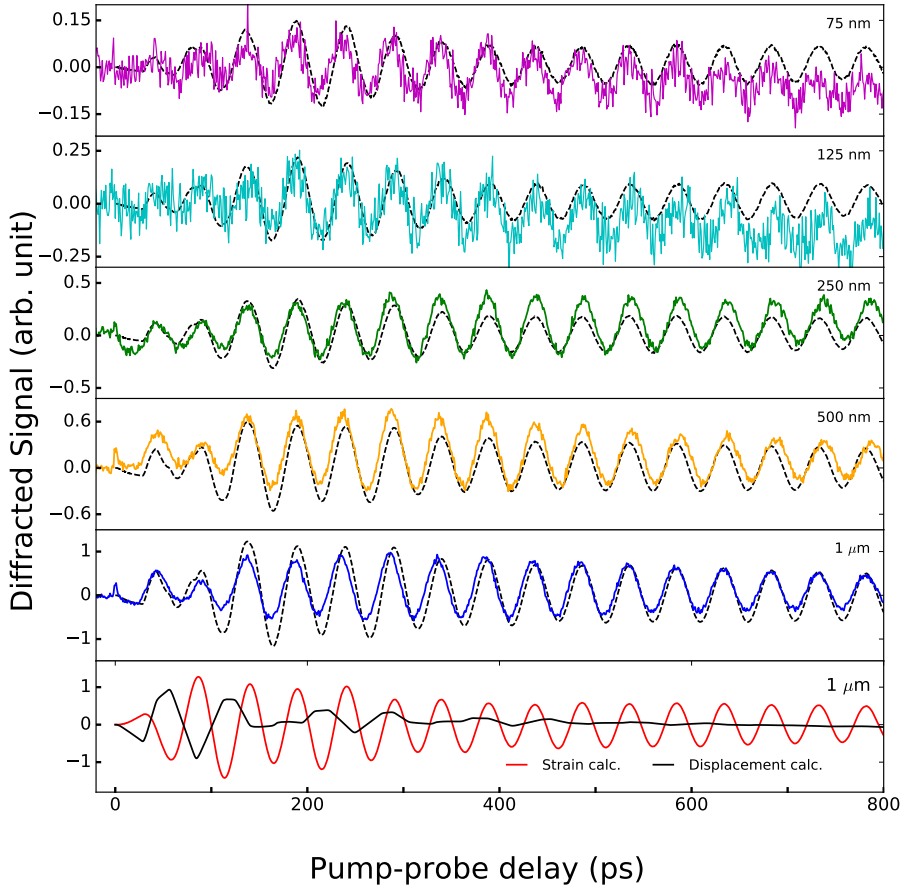


Figure 5.2: The measured first-order diffracted probe signal as a function of pump-probe time delay for the five Au gratings fabricated on a 90 nm thick Au layer. The linewidths of the gratings vary from 75 nm to 1 µm. The period of all gratings is 6 µm and the amplitude is 44 nm. The dashed curves are the numerically calculated diffraction signals as a function of pump-probe delay. In the bottom panel numerical calculations of the diffracted signals as a function of pump-probe time delay are shown taking *only* surface displacement at the glass/Au interface into account (black line) or *only* diffraction off the acoustic waves in glass (red line).

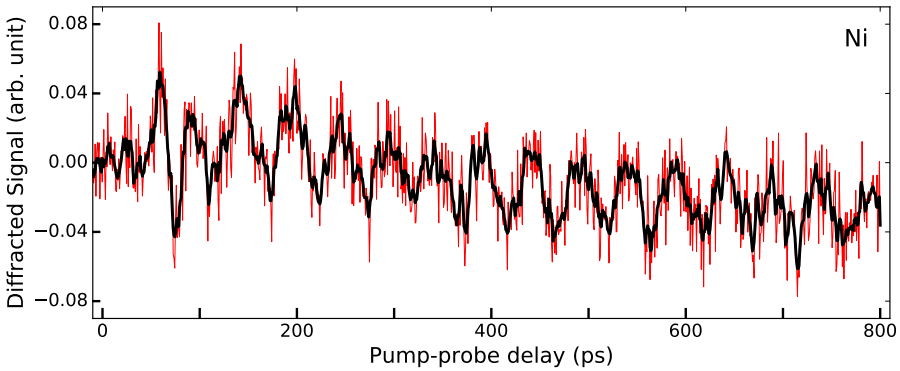


Figure 5.3: Measured first-order diffracted signal as a function of the pump-probe time delay between pump and probe for a 6 µm period, 40 nm amplitude and 500 nm linewidth Ni grating, fabricated on a 200 nm thick Ni layer (red curve). The black curve is a smoothed version of the red curve.

made of a different metal. We choose Ni for the layer and the grating because it has an electron-phonon coupling constant $g$ more than an order of magnitude larger than that of Au [59]. In Fig. 5.3 we plot the diffracted signal as a function of the pump-probe delay for the Ni grating, which has period of 6 µm and a linewidth of 500 nm. As the more noisy nature of the measurement suggests, the signal was significant smaller than the signal measured for the buried Au grating with the same 500 nm linewidth. For the Ni sample, around delay zero no diffraction peak due to a grating in the electron temperature was observed. Starting at a delay of about 60 ps, an oscillating signal with a period of about $50 \pm 2$ ps appears that has some resemblance to the signal obtained for the buried Au gratings. However, here, the first oscillation has a somewhat different, sharper, appearance than the subsequent oscillations compared to the signals shown for Au. Note that, here too, we observe that the diffracted signal drops below the signal level for negative delays.

In order to check if the thickness of the Au layer influences the measurements, we also measured on a similar set of gratings fabricated on a thicker Au layer of 142 nm. In Fig. 5.4 we plot the diffracted signal measured as a function of the pump-probe delay for the five different gratings (linewidths of 1 µm, 500 nm, 250 nm, 125 nm and 75 nm). In contrast to the measurements performed on the gratings on the 90 nm thick Au layer, here

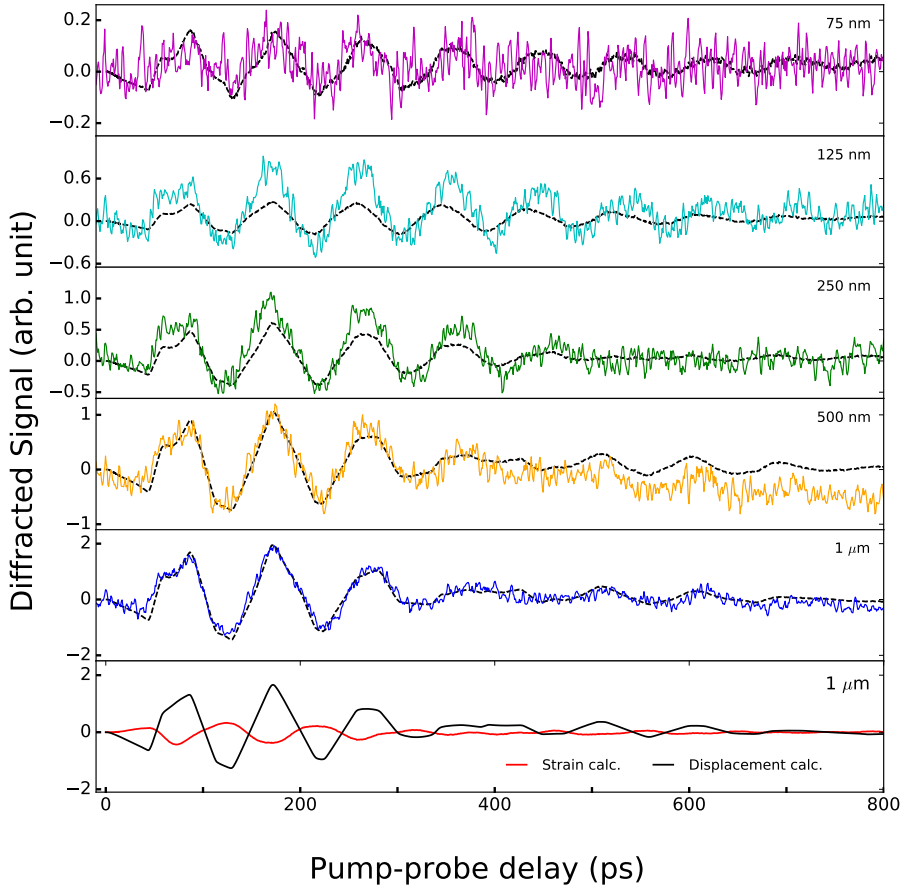


Figure 5.4: The measured first-order diffracted probe signal as a function of pump-probe time delay for the five Au gratings fabricated on a 142 nm thick Au layer. The linewidths of the gratings vary from 75 nm to 1 µm. The period of all gratings is 6 µm and the amplitude is 44 nm. The coloured curves are the measurements and the dashed curves are the numerically calculated diffraction signals as a function of pump-probe delay. In the bottom panel numerical calculations of the diffracted signals as a function of pump-probe time delay are shown taking *only* surface displacement at the glass/Au interface into account (black line) or *only* diffraction off the acoustic waves in glass (red line).

we observe a longer oscillation period of about $89 \pm 3$ ps, and a somewhat faster signal decay. Around zero delay, hints of a diffraction peak caused by an electron temperature grating are visible but the smaller signal-to-noise ratio does not allow us to state this with certainty. We note that a weaker diffraction signal due to heating of the electron gas is expected here, since the electron gas temperature grating is weaker for a thicker Au layer [85].

As we can observe in the measurements, the diffracted signal strength decreases with the duty cycle. To quantify this trend, we plot in Fig. 5.5(a) and (b) the peak-to-peak amplitude of the first acoustic reflection as a function of the duty cycle of the five gratings deposited on 90 nm Au layer and on 142 nm respectively. The data have been normalised by dividing all diffracted signals by the value for the 16.7 %duty cycle (1 µm linewidth) sample. As Chang et al. showed, for nonzero diffraction orders, the diffraction efficiency of a binary grating should be proportional to the square of the duty cycle, for low values of the duty cycle [66]. Surprisingly, in our experiment we find that the signal does not scale quadratically with the duty cycle. We observe a dependence that is closer to a linear dependence, indicated by the dashed line.

### 5.4.1 Results of the numerical calculations

In Fig. 5.2 (black dashed curves), we plot the diffracted signals, calculated for a 44 nm Au grating on a 90 nm thick Au layer where the grating lines are 1 µm, 500 nm, 250 nm, 125 nm and 75 nm wide. Calculations were first carried out for the samples with the 1 µm linewidth as these provided the strongest signals. Parameters were manually adjusted until the best fit between the measurements and the calculations was obtained for the first diffraction peak. Then, without changing parameter values, calculations were performed for the lower duty cycle gratings as well. In all calculations shown, the signal levels for negative delay caused by the presence of the background field were subtracted from the calculations. This is done to mimic the suppression of signals by the lock-in that are not modulated by the pump beam. After this subtraction, all curves were normalised by dividing them by the maximum value calculated for the 16.7 % duty cycle grating (1 µm linewidth). The calculations show oscillatory long-lasting signals with a period of about 50 ps for all gratings. The amplitudes of the

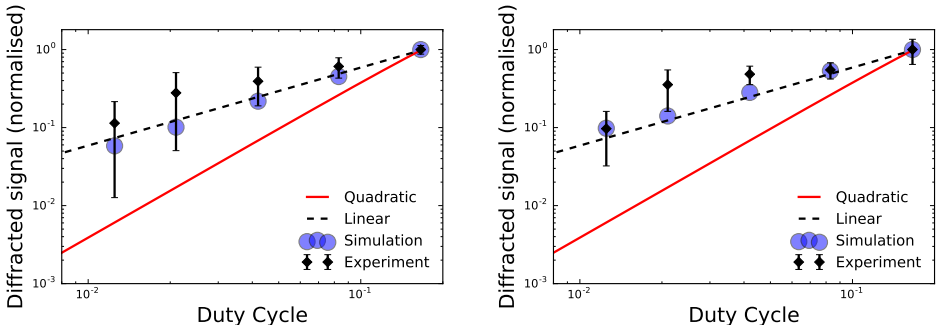


(a) (b)

Figure 5.5: (a) Normalised diffracted signal, taken here as the amplitude of the first positive diffraction peak, as function of duty cycle (expressed as a ratio), measured (black dots) and numerically calculated (blue dots) for a 44 nm Au grating on a 90 nm Au layer on glass. (b) Normalised diffracted signal as function of duty cycle, measured (black dots) and numerically calculated (blue dots) for a 44 nm Au grating on a 142 nm Au layer on glass. The dashed line represents a linear dependence, the red line a quadratic one. The plots are in double logarithmic scale. Here the duty cycle of the grating is expressed as the ratio between the linewidth and the period of the gratings.

signals decrease with the duty cycle of the gratings and all calculations are in good agreement with the experimental results. In the bottom panel of Fig. 5.2, we plot the calculated diffracted signal from *only* the Au surface displacement at the interface glass/Au (black curve) and from *only* the acoustic grating propagating inside the glass (strain, red curve), for the 1 µm linewidth sample. Here too, the same constant background field as used in the full calculations is assumed to be present. The calculated curves clearly show that the signal is dominated by the strain contribution.

In Fig. 5.4 (black dashed curves), we plot the diffracted signals, calculated for the 142 nm thick Au layer. The calculations show oscillating signals with the same shape as the measured signals. However, whereas there is a good agreement between the calculated amplitudes for the 1 µm, 500 nm, and 75 nm linewidth gratings, the calculated amplitudes are smaller than the measured ones for the 125 nm and 250 nm linewidth samples. We currently do not know what the origin of this discrepancy is. In the bottom panel of Fig. 5.4, we plot the calculated diffracted signals from *only* surface displacement (black curve), and from *only* the acoustic grating propagating inside the glass (red curve) for the 1 µm linewidth sample. Again the same constant background field as used in the full calculations is assumed to be present. In contrast to the calculations shown for the 90 nm thick Au layer, here we find that the displacement of the atoms at the glass/Au interface provides the strongest contribution to the measured signals. This difference is most likely caused by the fact that for the 90 nm thick Au layer, grating-shaped acoustic waves are partially transmitted into the glass with a periodicity that nearly matches the oscillation period $T$ associated with diffraction off the acoustic gratings in glass. This is not the case for the 142 nm thick layer due to the longer acoustic round-trip time in the layer.

## 5.5 Discussion

Our experimental results have some salient features that we wish to address below, such as the observation that the diffracted signal drops below the background level and the dependence of the strength of the diffracted signal on grating duty cycle.

### 5.5.1 "Negative" diffraction signals: Effect of background fields

A peculiar feature of our experiments is that we observe diffraction signals that drop below the background levels. As already explained in Chapter 4, we can assume that *another*, coherent scattered optical field is present, and this field can interfere with the field diffracted by the acoustic wave. The origin of this background field is scattering by interface roughness present near the glass/metal interface. The optical phase difference between the two diffracted fields will determine the extent to which the interference is constructive/destructive.

The above description of the effect of the background optical electric field gives a plausible physical explanation for the observation that the diffracted signals drop below the level seen for negative delays. However, it ignores the fact that, as we will explain in section 5.5.3, every time the sound wave reaches the glass/metal interface, part of the wave is periodically transmitted into the glass where each acoustic wave also gives rise to an additional time-dependent diffraction signal. This means that in reality, the field $E_{ac}$ is composed of several contributions, $E_{ac_k}e^{i\phi_k}$ (k=1,2,..) each with a time-dependent phase difference $\phi_k$ with respect to the background field $E_b$. Fortunately, using a full numerical model to describe the generation, propagation and optical detection of the acoustic waves, all these waves are automatically taking into account as we will show in section 5.4.1.

### 5.5.2 Acoustic waves in Ni and Au

To better understand the experimental results, we first have to explain how high frequency ($\sim$ 10 - 100 GHz) sound waves are generated in these metals. In Ni, the optical absorption depth of light with a wavelength of 400 nm is about 12 nm [59]. The absorption of the pump pulse by the electron gas in this layer leads to a rapid rise of the electron gas temperature. In principle, the electron gas energy can diffuse out of the penetration depth region, deeper into the metal [60]. However, in Ni the electron-phonon coupling constant is large, $g = 36 \times 10^{16}$ $Wm^{-3}K^{-1}$ [101]. This gives rise to rapid cooling of the electron gas and associated heating of the lattice, before the deposited energy has had the time to diffuse much deeper into the metal. Rapid heating and subsequent expansion of the lattice launches

a sound wave that propagates inside the metal. The buried grating reflects the acoustic wave back to the glass/Ni interface.

Due to the shape of the buried grating (see Fig. 5.1(a)), the sound wave takes longer to return when it reflects off the ridges of the grating compared to when it reflects off the valleys. As a result, the acoustic wavefront becomes spatially modulated. When the acoustic wave reaches the glass/Ni interface, it displaces the atoms in a spatially periodic manner with an amplitude of a few tens of picometers. We can detect this "acoustic replica" of the buried grating by diffraction of a probe pulse. For a 200 nm thick Ni layer, the round-trip time of the acoustic wave can be calculated as $T = 2l/v$, where $l$ is the layer thickness and $v$ is the speed of sound in the metal. Assuming a longitudinal velocity of 6.04 km/s [102], the round-trip time is expected to be 66.2 ps. In our Ni measurement shown in Fig. 5.3, however, the period of the oscillatory signal is about $50 \pm 2$ ps. Therefore, although it is tempting to attribute the oscillations observed after the first echo (Fig. 5.3) to the sound wave packet bouncing back and forth inside the Ni layer, there is a different explanation for these oscillations, as we will show in the next section.

For Au gratings on Au layers, the generation of acoustic waves occurs in a similar fashion. However, Au has a much smaller electron-phonon coupling constant [59, 94] than Ni. Whereas the penetration depth of 400 nm light in Au is only slightly larger than in Ni (about 16 nm), the electron gas energy in Au rapidly diffuses deeper into the metal before the electron gas has had the time to significantly cool through heating of the lattice. In fact, when a single thin layer (less than 150 nm) of Au is illuminated by an ultrashort pulse, the whole layer is rapidly and more or less homogeneously heated up. Rapid heating of the lattice leads to an oscillatory expansion and contraction of the layer in a direction perpendicular to the surface. Because of the "softness" of the glass, the atoms at the glass/Au interface have some freedom to move in a direction perpendicular to the interface. This means such an expansion/contraction of the lattice can be seen as a standing wave formed by the addition of two counter propagating acoustic waves, each having a wavelength corresponding to twice the thickness of the metal. Writing $u_1(t)$ and $u_2(t)$ for the time-dependent displacements of Au surface above the ridges and the valleys of the grating respectively, an acoustic grating and, thus, diffraction would be present only when $\Delta u(t) =$

$u_1(t) - u_2(t) \neq 0$. The rise of the first peak of the oscillation we observe in our measurements then corresponds to a growing value of $|\Delta u(t)|$. Note that $\Delta u(t)$ can change from positive to negative values and vice versa, which will lead to periodic inversions of the grating and thus to $\pi$ phase shifts of the diffracted fields.

### 5.5.3 Propagation of acoustic waves in glass

Surprisingly, for the Au gratings on 90 nm Au on glass, the oscillations initially seem to grow in amplitude somewhat before slowly decaying for longer time delays. The period of these oscillations is around $50 \pm 2$ ps and is similar to the oscillation period observed for Ni in Fig. 5.2(b). In fact, the prolonged ringing of the Au layer is due to the so-called Brillouin scattering [44, 93]. Each time the acoustic wave in the metal reaches the glass/metal interface, part of the grating-shaped acoustic wave can penetrate the glass substrate. In the glass, the acoustic grating modifies the optical refractive-index and thus forms a refractive-index grating from which the probe pulse can diffract. When the first acoustic reflection off the buried grating has reached the interface, it is partially transmitted into the glass where it continues to propagate away from the interface. When the probe pulse is incident on this "acoustic grating", it will diffract into the direction of the Si detector. However, part of the probe beam will continue to propagate to the glass/metal interface and reflect back. Due to the propagation of the probe beam to the interface and back, a phase difference between the two diffracted beams is created. This leads to constructive/destructive interference and thus to a signal that oscillates with the distance between the acoustic wave grating in the glass and the glass/metal interface. The period of this oscillation is given by $T = \lambda / (2nvcos\theta)$ [103]. Here, $\lambda$ is the probe wavelength, $n$ is the refractive index of the glass at this wavelength, $v$ is the speed of sound in glass, and $\theta$ is the angle of incidence, measured inside the glass. For glass, $v \sim 5.24$ km/s [95], $n = 1.5$ and in our experiment $\theta$=14.5°. We then obtain an oscillation period of 52.6 ps. This period is close to the period seen in the diffracted signals for the gratings on 90 nm Au and on 200 nm Ni. A striking difference between the time-dependent diffraction for the gratings on the 90 nm layer and the 142 nm thick Au layers is that for the latter, the $\sim$ 50 ps period oscillatory signal caused

by diffraction from the strain grating propagating in glass is more or less absent in the measurements. This strongly suggests that for the 142 nm thick layer, the contribution to the diffraction of the acoustic wave in glass is smaller than the contribution from the acoustic wave-induced atomic displacement at the glass/Au interface. This is supported by numerical calculations of the diffracted signals.

### 5.5.4 Diffraction efficiency as a function of the duty cycle

Now that we understand our experimental data and we are able to interpret them, we can also understand why the diffraction signal does not scale quadratically with the duty cycle of the gratings. The diffraction efficiency of a diffracted order is a value which expresses the capability of the grating to diffract light in that order. It is defined as the ratio between the power of the diffracted light beam to that of the incident beam. As already shown by Chang et al. [66], for nonzero diffraction orders (m≠0) the diffraction efficiency for a binary grating can be written as

$$\eta|_{m\neq 0} = 2A^2(1-\cos\psi)D^2\mathrm{sinc}^2(mD), \tag{5.1}$$

where A corresponds to the amplitude of the reflectance of the metal of the grating (A = 0 for no reflection, A = 1 for perfect reflection). $\psi$ represents the phase difference between light reflected from the valleys and the peaks of the grating. D is the duty cycle of the grating, here expressed as the ratio between the linewidth and the period of the gratings. For small values of D, the efficiency of the first diffracted order ($m$=1) can be approximated by,

$$\eta \approx 2A^2(1-\cos\psi)D^2. \tag{5.2}$$

Eq. (5.2) clearly shows that the diffraction efficiency should have a quadratic dependence on the duty cycle of the grating. In Figs. 5.5(a) and (b), this quadratic dependence is illustrated by the red line. However the measured diffracted signal strength versus duty cycle is closer to a linear than a quadratic dependence. This can be understood by first realising that $E_{ac}^2 \propto \eta$. From Eq. 5.2 we obtain $E_{ac}^2 \propto \eta \propto D^2$ and thus $E_{ac} \propto D$. Due to the presence of the background diffracted field, the $\phi$-dependent oscillatory part of the total optical power discussed in section 5.5.1 is not proportional to $E_{ac}^2$, but to the cross-term, $2E_bE_{ac}\cos(\phi) \propto D$ and it dominates the

measured signal because $E_b \gg E_{ac}$. In other words, due to the background diffracted field $E_b$, the diffracted signal measured by the photo-diode and filtered by the lock-in amplifier should scale *linearly* with duty cycle, in agreement with our measurements. We note, however, that Eq. 5.2 is valid for binary (square wave) gratings only. According to diffraction theory, when the size of an object becomes comparable or smaller than the wavelength of the wave, diffraction becomes significant [64]. The acoustic wave that diffracts off the narrow lines has spread out by the time it reaches the interface and the grating can no longer be considered a binary grating. Thus, in our experiments, for grating lines on the order of or smaller than the acoustic wavelength, which is 180 nm for the 90 nm Au layer and 282 nm for the 142 nm Au layer, the acoustic gratings at the interface glass/metal should not be square-wave-like replicas of the buried ones anymore for the thinnest grating lines. As a result, for the lowest duty cycle samples, it is not directly obvious that this linear trend should still hold. However, full numerical calculations that take acoustic diffraction into account also show that the diffracted signal versus duty cycle remains close to a linear dependence, as shown by blue dots in Fig. 5.5. The calculated interface displacement profiles (not shown here) deviate somewhat from the ideal binary shape due acoustic diffraction, especially for the lowest duty cycle gratings. However, these changes have little effect on the diffracted signal strength.

It is interesting to get an estimate of the amplitudes of the glass/Au interface displacement gratings and of the corresponding first-order diffraction efficiencies of these gratings, assuming no background field would be present and ignoring deviations from the shape of a perfect binary grating. From the numerical calculations, we find that the estimated peak-to-valley amplitude of the gratings fabricated on the 90 nm thick Au layer ranges from 14.1 pm for the 75 nm linewidth sample, to 52.6 pm for the 1 µm linewidth sample. Using Eq. (5.2) this gives us estimated diffraction efficiencies $\eta$ from $\sim 1.72 \times 10^{-11}$ to $\sim 4.07 \times 10^{-8}$ respectively. For the 142 nm thick Au sample, the amplitude of the interface displacement gratings is slightly smaller, ranging from 8.6 to 33.5 pm for the 75 nm and 1 µm linewidth samples respectively. Again using Eq. (5.2), we estimate that this corresponds to diffraction efficiencies of $\sim 6.4 \times 10^{-12}$ and $\sim 1.7 \times 10^{-8}$. These calculated diffraction efficiencies are quite small and would be chal-

lenging to measure, especially for the 75 nm linewidth samples. Fortunately, we are still able to detect the buried gratings due to the presence of the scattered background optical field, which coherently amplifies the optical signal diffracted by the acoustic wave.

## 5.6 Summary

We have shown that ultrahigh-frequency sound waves, generated with femtosecond laser pulses, can be used to detect gratings buried underneath optically opaque layers. In our experiments these sound waves are reflected off the buried grating and acquire a spatially periodic acoustic phase. When these acoustic waves reach the glass/metal interface they displace the atoms at the interface thereby forming a grating that can be detected by diffraction of a delayed probe pulse. By varying the duty cycle of the gratings we have shown that gratings with linewidths as narrow as 75 nm can be detected. We find that the diffracted signals are composed of contributions from the grating-shaped acoustic waves in the metal and from diffraction caused by the strain grating travelling in glass. Our results show a surprising decrease in the measured diffracted signal to values below the level seen for negative delays. We attribute this to the presence of a coherent background optical field that interferes with the optical fields diffracted by the acoustic waves in the metal and the glass, and thus also enhances the diffracted signals. As a result, the predicted diffracted signal strength as a function of duty cycle changes from a quadratic dependence to a linear dependence. The results illustrate the potential of ultrafast photoacoustics to detect gratings with narrow lines buried below optically opaque layers.

# 6 Enhanced detection of laser induced-acoustic waves by surface plasmon polaritons

In this Chapter we present a wavelength-dependent study on the detection of laser-induced acoustic waves on a plasmonic grating. In our experiments we use gold gratings fabricated on top of a $SiO_2$ substrate. This grating has a Surface Plasmon Polariton (SPP) resonance at 650 nm. Pump-probe measurements were performed on the grating, where the probe beam was tuned around the SPP resonance wavelength. Our results show that we are able to induce at least three different types of acoustic oscillations simultaneously, namely surface acoustic waves (SAWs), quasi-normal modes (NMs) and longitudinal acoustic waves (LWs). As a consequence, density variations caused by the acoustic waves lead to an electron density change which can shift the SPP resonance of the grating. We also observe an enhancement of the SAW signal at the SPP resonance, whilst the other two modes reach a maximum on the slopes of the SPP resonance. Our results show that SPPs can be used to enhance the reflection changes caused by laser-induced acoustic waves.

## 6.1 Introduction

Laser-induced acoustic waves can be detected by measuring changes in optical properties, such as reflection or transmission [25] or diffraction from laser-induced acoustic gratings [75, 76, 84, 104]. Changes in optical reflection caused by acoustic waves are usually very small. Despite the attempt to increase the signal-to-noise ratio by using lock-in detection, as we have shown in Chapter 5, the first-order diffraction efficiencies of the glass/Au interface displacement gratings range between $10^{-12}$ and $10^{-7}$. In this Chapter, we focus on a method to enhance photoacoustic signal strength. Surface Plasmon Polaritons (SPPs) may give us an opportunity to achieve this. SPPs have proven to be a powerful tool to study the acoustic response of metallic nanoparticles and thin films [105–112]. Usually, the plasmonic enhancement of an acoustic signal is caused by a shift of the SPP resonance due to acoustic wave-induced shift of the dielectric function. This occurs for example, in metallic nano-particles where the electron density changes due to the "breathing" of the metallic nanoparticle in response to the rapid heating of the lattice [111, 113, 114]. This change in electron density can result in a change of the plasma frequency and thus the dielectric function. Numerical calculations on signal strength enhancement using a plasmonic grating have been performed before [106, 115]. They show that, under plasmonic resonance conditions, the optical response of an acoustic cavity or grating to an acoustic wave can increase by an order of magnitude. The photoacoustic response of metallic periodic arrays of stripes attached to the surface of a substrate and illuminated by an ultrashort laser has been studied in the past [116–118]. When an illuminated surface has such spatial inhomogeneities, shear waves and surface acoustic waves (SAWs) can be excited, or guided modes such as Lamb waves [118–124]. Depending on which combination of metal and substrate is chosen, other acoustic modes can be excited as well. These acoustic modes are known as flexural and longitudinal modes of the grating lines, also called "normal modes" [52, 116, 125]. However, the acoustic signals measured in the past were quite weak, giving optical reflection changes with a magnitude of $\Delta R/R \approx 10^{-4}$.

Here, we show a wavelength-dependence study on the detection of laser-induced acoustic waves on a plasmonic grating. For our experiments, 440 nm period, 71 % duty cycle, 47 nm amplitude gold (Au) gratings were

fabricated on top of a $SiO_2$ substrate. A 400 nm wavelength pulse was used as a pump. Optical reflection changes of a second, delayed probe pulse with a wavelength tunable from 600 to 700 nm around the plasmonic resonance at 650 nm, were measured. Our results show that we can induce at least three different types of oscillations simultaneously, namely SAWs, quasi-normal modes (NMs) and longitudinal acoustic waves (LWs). An enhancement of the optical reflection changes due to SAWs at the SPP resonance is observed, whilst optical reflection changes due to the other two acoustic modes reach a maximum on the slopes of the SPP resonance wavelength. In addition, we find a phase shift of the optical reflection changes induced by the three measured acoustic oscillations as a function of the probe wavelength. The NM and LW signal oscillations show a $\pi$ phase shift in the range of 600-700 nm, going from below to above the SPP resonance wavelength of 650 nm. Using a simulated typical value for the lattice expansion, we were able to calculate a reflection change induced by the shift of the SPP resonance as a function of the electron density. This acoustically induced shift in the SPP resonance results in reflection changes which match our data well, and also explains the phase shift we measure for the optical reflection changes induced by the LW and NM. For the optical reflection changes due to SAW, the phase shift is less well understood. Our results show that plasmonic structures can be employed for enhancing photoacoustic detection signals by measuring optical reflection changes on and around the SPP resonance.

## 6.2 Samples preparation and optical setup

The grating substrate used in this work was made by nanoPHAB B.V. (Eindhoven, NL). It consists of a 200 nm thick $SiO_2$ layer on a Si substrate. The grating pattern is etched into the $SiO_2$ layer (see Fig. 6.1(a)). Then, Au layers were deposited onto the grating surface in the AMOLF NanoLab. These metal films where deposited by thermal evaporation in a vacuum chamber, as described in 3.1.4, at an evaporation rate of 1 Å/s. Three different thicknesses were used for the Au layers, namely 100, 136 and 177 nm (see Fig. 6.1(b)). After metal deposition, the period of the grating is 440 nm and the amplitude 47 nm. The duty cycle of the Au grating is approximately 71 %. Surface characterisation of the gratings was done

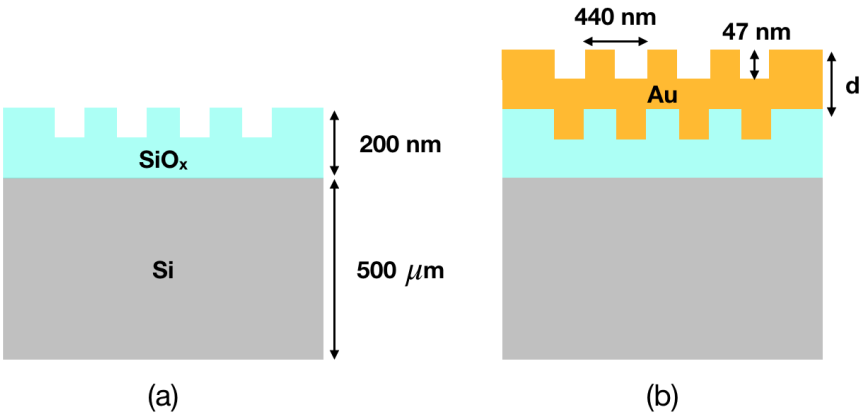


Figure 6.1: Schematic representation of the grating sample used in the work described in this chapter, before (a) and after (b) metal deposition. The Au layers have a thickness of d = 100, 136 and 177 nm. The period of the grating is 440 nm and the amplitude 47 nm. The duty cycle of the grating is ≈ 71 %.

using both SEM and AFM. Fig. 6.2 shows a SEM measurement of the grating etched in $SiO_2$, before Au deposition. Before deposition, the grating has a period of 440 nm and a duty cycle of 58 %. After metal deposition, the width of the grating lines increases. Consequently, the duty cycle of the grating increased to ≈ 71 %. In Fig. 6.3 an example of an AFM measurement on the grating after metal deposition is shown. AFM imaging is necessary to measure the amplitude and the period of the gratings. We can see from Fig. 6.4 that all four gratings used in this work have a similar height profile (amplitude ≈ 47 nm) and period (≈ 440 nm).

The optical setup used in this work is described in more detail in 3.2.3. It is built around an amplified Ti:Sapphire laser which generates 35 fs laser pulses with a repetition rate of 1 kHz and a central wavelength of 800 nm. The scheme used is a classical pump-probe scheme. The 800 nm wavelength output is split into two parts. The stronger arm is frequency-doubled to generate 400 nm wavelength pulses and is used as a pump beam. The weaker arm is time-delayed using an optical delay line formed by a retroreflecting pair of mirrors mounted on a mechanical translation stage, and is used as a probe beam. The probe can be tuned from 600 to 700 nm. Here, the pump diameter is approximately 400 µm and the pump pulse

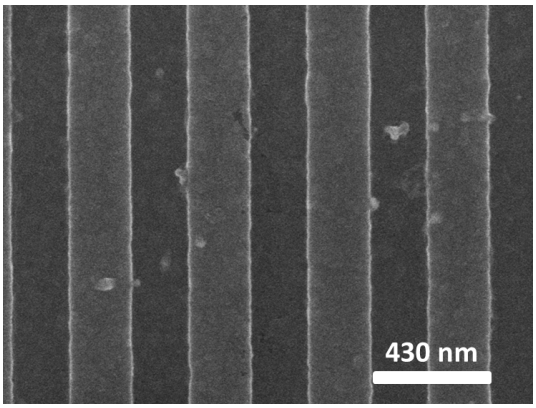


Figure 6.2: SEM image of the grating etched in the $SiO_2$ layer.

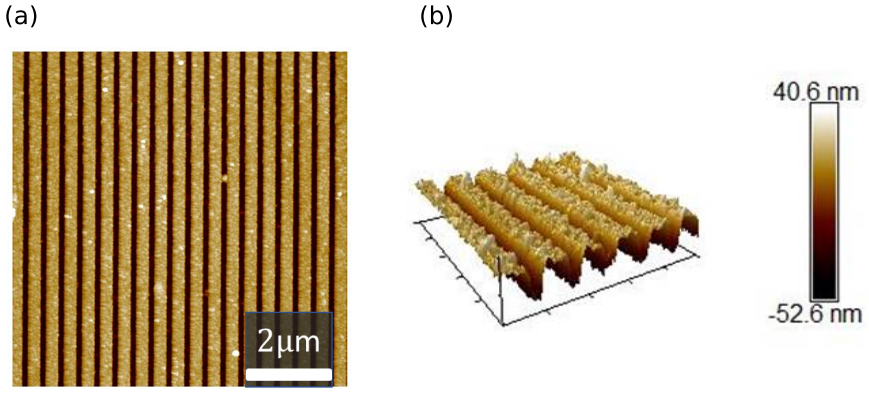


Figure 6.3: AFM image of the grating after the deposition of 177 nm of Au, shown in 2D (a) and in pseudo-3D (b). The periodicity of the grating is 440 nm and the amplitude is 47 nm.

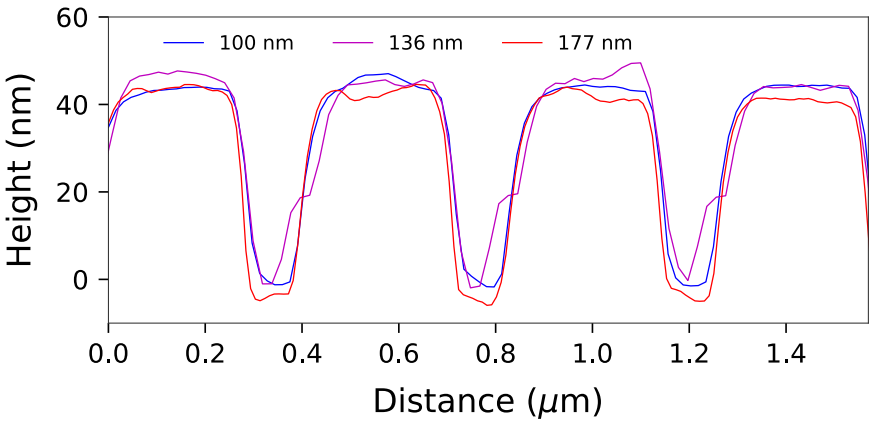


Figure 6.4: Height profiles of the three gratings used in this work.

energy is 6 µJ. The probe has a diameter of 80 µm on the sample and the probe pulse energy is kept constant at 0.3 µJ.

## 6.3 SPP excitation on grating

As explained in Section 2.4.1, SPPs do not normally couple to free-space propagating electromagnetic waves. In the presence of a grating, SPPs can be excited when the appropriate phasematching condition is fulfilled [73]. Phasematching is obtained when the wave vector of the external field projected on the grating combined with the grating wave vector matches the wave vector of the SPP. By choosing the right grating wave vector and frequency of the incident light, it is possible to determine the direction of propagation of the SPP. In our case, the SPP propagates in the opposite direction with respect to the $x$-component of the incident field (see Fig. 6.5). This can be expressed as,

$$k_g - k_x^{inc} = k_{SPP} \tag{6.1}$$

where $k_x^{inc} = \frac{\omega}{c}\sin\theta$, $k_g = \frac{2\pi}{D}$ and $k_{SPP} = \frac{\omega}{c}\sqrt{\frac{\epsilon_1\epsilon_2}{\epsilon_1+\epsilon_2}}$. Here $\omega$ is the frequency of the incident light and $\theta$ is the angle of incidence defined as the angle with respect to the surface normal. $D$ is the period of the grating. $\epsilon_1$ and $\epsilon_2$ are the permettivities of the dielectric and the metal, respectively

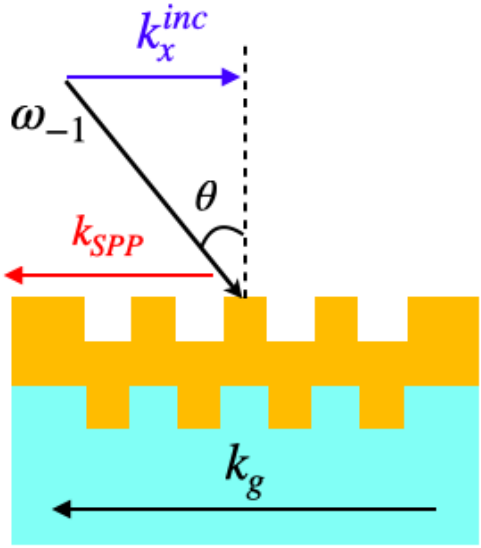


Figure 6.5: Schematic of SPP propagating in the opposite direction with respect to the x-component of the incident field.

and for simplicity we assume that they are real. Thus, Eq. 6.1 becomes

$$\frac{2\pi}{D} - \frac{\omega}{c}\sin\theta = \frac{\omega}{c}\sqrt{\frac{\epsilon_1\epsilon_2}{\epsilon_1+\epsilon_2}}, \tag{6.2}$$

At the air/metal interface, $\epsilon_2 \gg \epsilon_1$ and, thus, $\sqrt{\frac{\epsilon_1\epsilon_2}{\epsilon_1+\epsilon_2}} \approx 1$. We can rewrite Eq. 6.2 as

$$\frac{2\pi}{D} - \frac{\omega}{c}\sin\theta \approx \frac{\omega}{c}. \tag{6.3}$$

Eq. 6.3 can be finally expressed as a function of the incident angle $\theta$ as

$$\theta = \arcsin\left(\frac{\lambda}{D} - 1\right). \tag{6.4}$$

Now, knowing the period of the grating and the wavelength of the incident light, the right angle needs to be chosen in order to excite a SPP on the grating.

In our experiments, we choose the grating with the period of 440 nm to be resonant at 650 nm. In that case, the angle of incidence must be around

28°.

## 6.4 Experimental Results

The first step is to experimentally determine the angle of incidence at which the plasmonic resonance is excited for an incident wavelength of 650 nm on the 440 nm period grating.

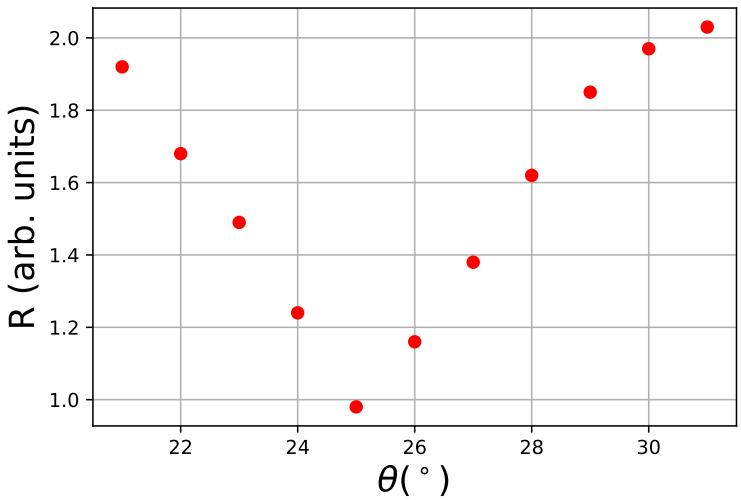


Figure 6.6: Reflection of the 650 nm probe light from the 100 nm thick Au grating as a function of the angle of incidence.

The reflection of the 650 nm probe beam was measured as a function of the incident angle. When a SPP is excited, the reflection of the incident light has a minimum. As we show in Fig. 6.6, the minimum in reflection appears at $25 \pm 1°$. The difference with the predicted value of 28° may be related to the values of $\epsilon_2$ used in the calculation and/or by small errors in the measurement of the angle of incidence. It is also known that the SPP resonance wavelength changes with the grating amplitude, which is not contained by Eq. 6.9. Thus, the angle of incidence of the probe beam was fixed at around 25° for the experiments. For the pump beam, the angle of incidence was kept constant, at around 15°, for all the experiments described below. The 400 nm wavelength pump beam does not excite SPPs.

In Fig. 6.7 we plot the measured pump-induced probe reflection changes

as a function of time delay between pump and probe. The probe wavelength was tuned in a range around the plasmonic resonance wavelength, namely from 600 to 700 nm. Here, we show the results for the grating covered by a 100 nm thick Au layer.

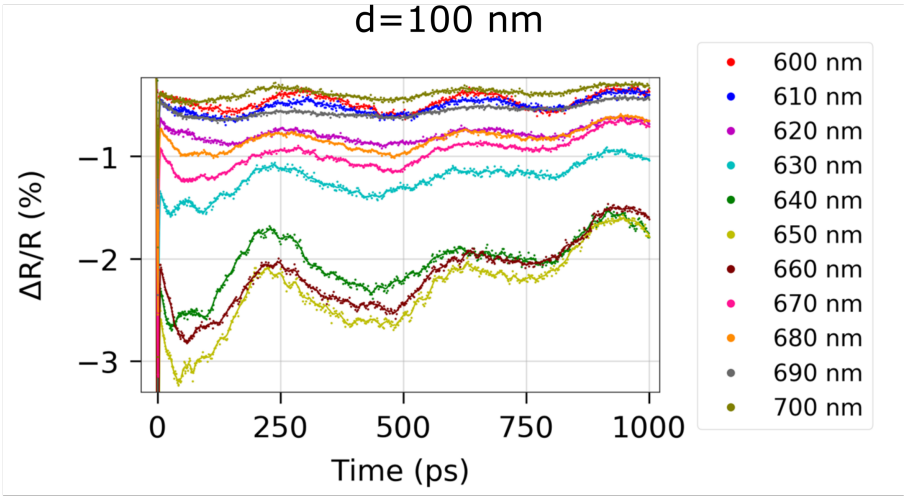


Figure 6.7: Probe reflection change as a function of the pump-probe time delay, measured on the 100 nm thick Au grating for 11 different wavelengths.

At the plasmonic resonance ($\lambda = 650$ nm, yellow-green curve) we observe the maximum reflection change. At delay t = 0, when the pump and the probe overlap in time, a sharp decrease in reflection $\Delta R/R_0$ is observed, related to the heating of the electron gas [85]. On this time scale, the signal is dominated by the electron dynamics. In fact, the probe photon energy range we use is between 1.7 and 2 eV, thus below the interband transition threshold for Au. In this range, Hohlfeld et al. calculated that for increasing electron temperature, $T_e$, the reflection decreases [126]. In our case, not only $T_e$ increases but also interband transitions are possible due to the perturbations caused by the presence of the pump beam. Therefore, the calculations by Hohlfeld are probably not the whole story. During the next couple of ps, when the electron gas releases its energy to the lattice, the abrupt decrease is followed by a smooth increase. The signal returns to its unperturbed state on a time scale $\gg 1$ ns.

For time scales longer than 10 ps, a damped oscillatory signal becomes

apparent with a periodicity of $350 \pm 20$ ps, corresponding to a frequency of $\approx 2.8$ GHz. This is most likely the result of a surface acoustic wave

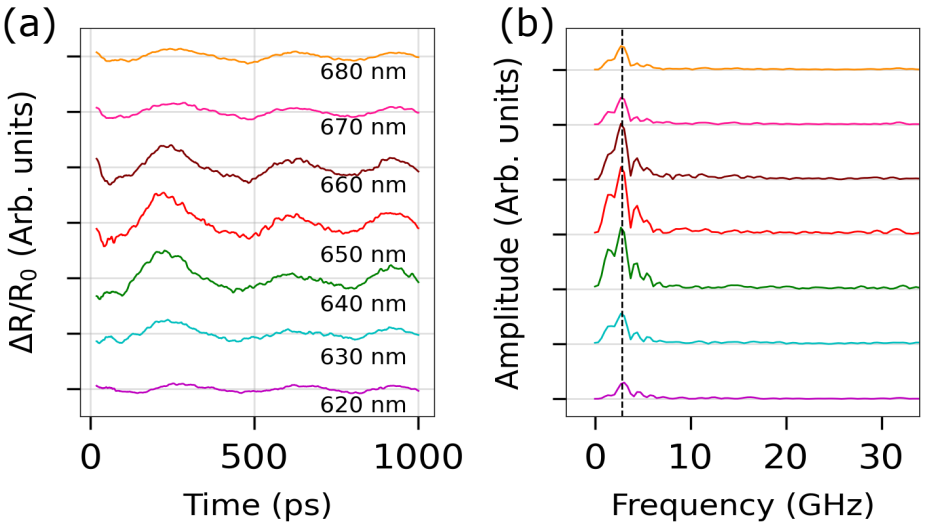


Figure 6.8: (a) Probe reflection change as a function of the pump-probe time delay on the 100 nm thick grating measured at different probe wavelengths indicated in the figure. (b) The amplitude of the FFT calculated from the measured signals. A peak at $\approx 2.8$ GHz is present for all the measurements, which we tentatively attribute to the SAW.

(SAW) with a wave vector determined by the grating period [124]. As we will show later, the phase of the SAW seems to gradually vary between 0 to $0.7\pi$, for different wavelengths. The oscillations are superimposed on a slow increase in signal intensity due to the Au layer heating. we note that our interest lies mostly in the oscillations observed between 50 and 1000 ps. The heating contribution is a fairly well known function of time. Therefore, we subtracted the thermal contribution from the overall signal by subtracting an exponential function. In Fig. 6.8 (a) we show the same results, now leaving out the electronic peak and after removing the slowly varying background due to the heating of the Au layer. We then performed a Fast Fourier Transform (FFT) of these signals in order to see which frequencies are present in the signal. In Fig. 6.8 (b) we show the signal amplitude as a function of the frequency of the oscillatory part of the signal. As can be clearly seen, the main frequency present is at 2.8

GHz, which we attribute to a SAW and which will be discussed further in Section 6.5.1. We also observe a shoulder around 1.5 GHz and a multitude of smaller peaks after the SAW peak, of (mostly) unknown origin.

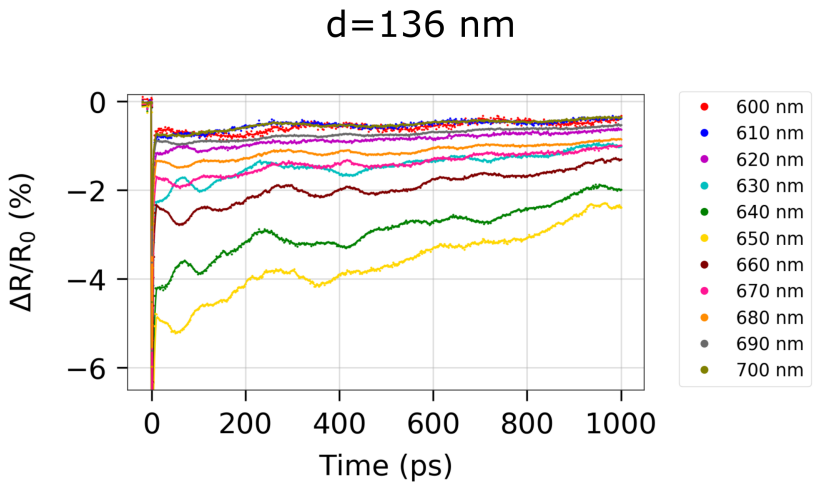


Figure 6.9: Probe reflection change as a function of the pump-probe time delay, measured on the 136 nm thick Au grating for 11 different wavelengths ranging from 600 to 700 nm.

In order to check if the thickness of the Au layer affects the acoustic wave generation, we deposited a thicker layer of Au onto the same grating. The previous Au layer was removed with a wet etchant and a 136 nm thick Au layer was subsequently thermally evaporated on top of the bare grating.

Fig. 6.9 shows the measured reflection changes as a function of time delay between pump and probe for this sample at different wavelengths. As in the previous case, we first observe a peak at zero delay due to the increase of the electron gas temperature in the first few ps. It is followed by an oscillatory signal which is composed of more than one oscillation, in contrast with the single oscillation observed in Fig. 6.7. We can clearly distinguish a slow oscillation with a periodicity of about 350 ps, again, presumably due to the SAW. Faster oscillations are superimposed on the SAW which are more or less visible in all the measurements.

In Fig. 6.10 (a) we show the measured reflection changes as a function

of the pump-probe time delay with the exponential trend removed. A FFT was performed on the data, to better characterise both the nature and the number of oscillations. In Fig. 6.10 (b), the amplitude of the FFT as a function of the frequency is plotted. Here, we can clearly see that at

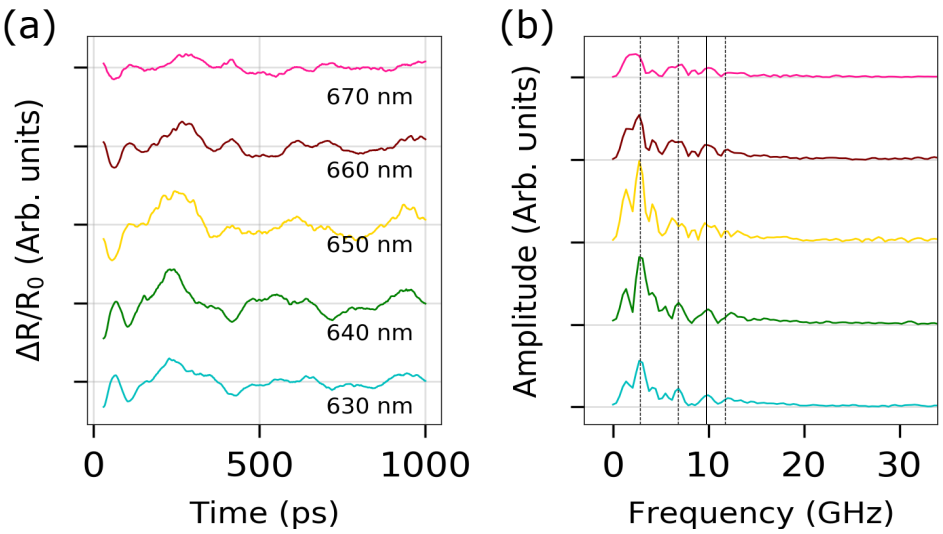


Figure 6.10: (a) Probe reflection change as a function of the pump-probe time delay on the 136 nm thick grating measured at different probe wavelengths indicated in the figure. (b) The amplitude of the FFT of the measured signals. Three peaks at $\approx$ 2.8, 6.9 and 12.1 GHz are present for all the measurements, which we attribute to SAW, NM and LW, respectively.

least three frequencies are present. We have a first main peak at around 2.8 GHz which we attribute to the SAW. A second peak at 6.9 GHz is observed. Finally, two smaller peaks at around 9.8 (indicated by the black solid line) and 12.1 GHz are observed. The 12.1 GHz peak most likely corresponds to the oscillation frequency of the whole Au layer, which we call the *longitudinal wave* (LW). In fact, it can be calculated as $T = 2l/v$, where $l$ is the layer thickness and $v$ is the speed of sound in the metal. Assuming a longitudinal velocity of 3.2 km/s [53], the round-trip time is expected to be $\approx$ 85 ps, which correspond to a frequency of $\approx$ 11.8 GHz. We will discuss the nature of these oscillations in more detail in the next section. Note that these faster oscillations are opposite in phase when going from below to above the SPP resonance. This can be clearly seen in the

first 100 ps. The nature of the oscillation at 9.8 GHz is still not understood. As in the previous sample, we see a shoulder around 1.5 GHz.

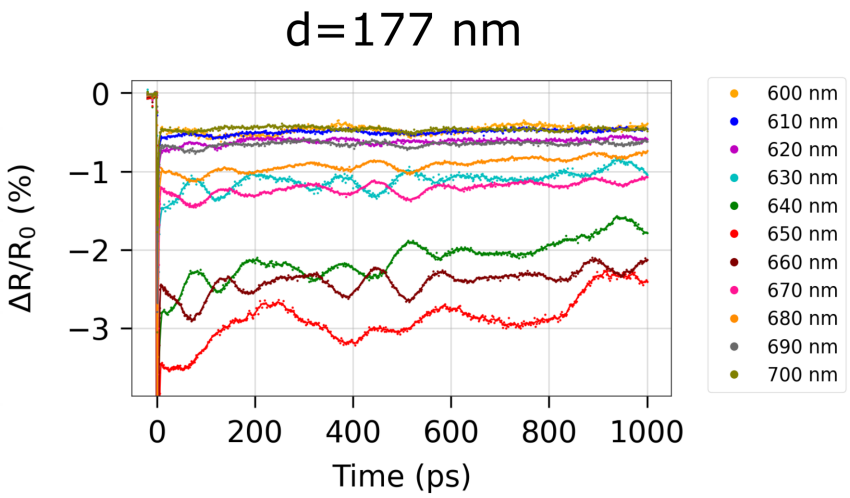


Figure 6.11: Probe reflection change as a function of the pump-probe time delay, measured on the 177 nm thick Au grating for 11 different wavelengths ranging from 600 to 700 nm.

In order to confirm the nature of the oscillation at 6.9 GHz, we decided to make a third thicker sample. By using the same technique, a 177 nm Au layer was deposited onto the bare grating. Fig. 6.11 shows the reflection changes as a function of the time delay between pump and probe measured for the 177 nm sample at different wavelengths. As in the previous case, we can clearly see that the signal is composed of more than one oscillation. In Fig. 6.12 (a) we show the results for different probe wavelengths, after removing the decaying thermal background.

From the FFT shown in 6.12(b), we see that the signal is composed of three main different oscillations. We have again the 2.8 GHz peak, due to the SAW, and a 6.9 GHz peak, most likely corresponding to the NM, which is a vibration of the grating line along a direction parallel to the surface and perpendicular to the line. The third peak at around 9.3 GHz is most probably due to the longitudinal oscillation of the 177 nm Au layer. It can be calculated as $T = 2l/v$, where $l$ is the layer thickness and $v$

is the speed of sound in the metal. Assuming a longitudinal velocity of

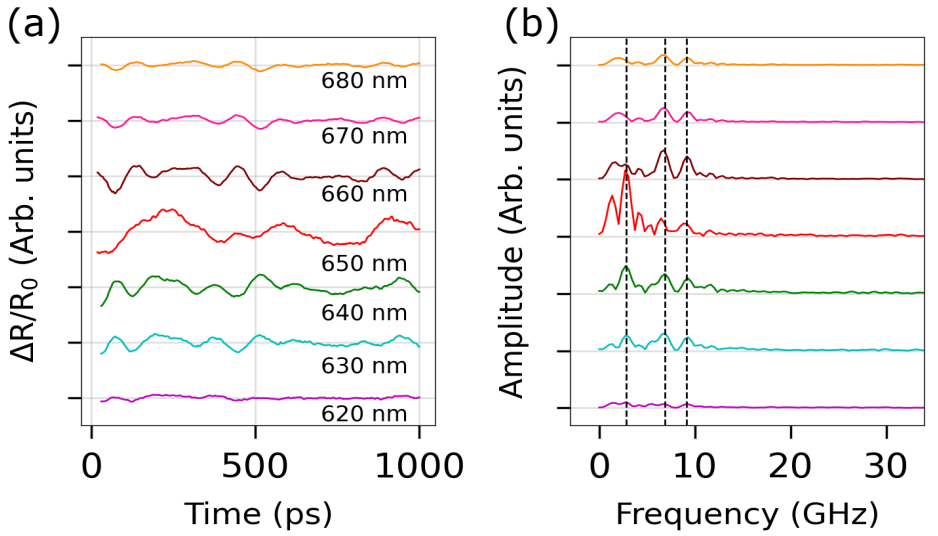


Figure 6.12: (a) Probe reflection change as a function of the pump-probe time delay on the 177 nm thick grating, measured at different probe wavelengths indicated in the figure. (b) The amplitude of the FFT of the measured signals. Three peaks at $\approx$ 2.8, 6.9 and 9.3 GHz are present for all the measurements, corresponding to the a SAW, a NM and a LW, respectively.

3.2 km/s [53], the round-trip time is expected to be $\approx$ 110.6 ps, which corresponds to a frequency of $\approx$ 9.1 GHz. As in the previous cases, a shoulder around 1.5 GHz and a multitude of smaller peaks are present. It is immediately clear in Fig. 6.12 (a) that the fast oscillations are opposite in phase for wavelengths above the plasmonic resonance (650 nm, red curve) when compared to wavelengths below the plasmonic resonance.

## 6.5 Discussion

### 6.5.1 Laser induced-acoustic wave generation on plasmonic gratings

If the surface of an absorbing material is illuminated by a short laser pulse, both bulk and surface waves can be generated by thermal expansion of the material. From Figs. 6.8 (b), 6.10 (b) and 6.12 (b), we are able to attribute tentatively 3 oscillation frequencies to just as many acoustic modes. In what follows, we will treat the measured signals as consisting of the sum of three sine waves, each with a frequency corresponding to that of the three oscillations observed in the measured signals.

We have investigated the frequencies of these oscillations and their dependence on the sample thickness, which we will discuss next.

**Surface Acoustic Waves**

The strongest contribution to the acoustic signal is the oscillation present at 2.8 GHz. We attribute this oscillation to a surface acoustic wave (SAW). When an intense laser pulse is focused on a modulated surface, it can generate a kind of SAW called a *Rayleigh surface wave* [127]. They are waves which propagate at the surface of the sample and their influence extends into the substrate. The frequency of this SAW is determined by the grating spatial period $D$ and the surface sound velocity (or Rayleigh velocity), $v_s$ [23]. The oscillation period can be expressed as

$$T_s = D/v_s. \tag{6.5}$$

For Au, $v_s$= 1172 m/s [128] and the period of our grating is 440 nm. Thus, the period of the SAWs excited on our sample is calculated to be T $\approx$ 375ps. This value is in reasonable agreement with the experimental value that we can extract from our measurements of T = 350 $\pm$ 20ps. Moreover, many studies have been performed on SAWs generated by periodic structures in picosecond ultrasound experiments [96, 116]. In particular, they show that Rayleigh SAWs are observed when the loss of acoustic energy into the substrate is low.

In our case, the substrate is Au itself since the Au layer covers both the valleys and the ridges of the grating. This causes only a low radiation loss into the substrate and the Rayleigh wave can be observed.

It is important to notice that the observed oscillations are caused by two counter propagating waves which form a standing wave in the area excited by the pump. These waves can propagate into the regions adjacent to the spot. In this work, we have not measured the change in optical reflectivity in a position some distance away from the pump spot.

**Normal Modes**

Besides surface waves, the normal modes of the individual metallic bars can be also excited. The displacements associated with these modes, their amplitude, and their frequencies depend both on the cross section of the bars and on the excitation process but they do not depend on the period of the grating. We consider the case where the length $L$ of the grating line greatly exceeds its cross section $a$, thus $L/a \gg 1$. We also assume, for simplicity, that the metallic bars are suspended in air and are not in contact with the substrate. In this case, when the grating line is excited by a thermal pulse, only two modes are excited: the extensional and breathing modes of the line [129]. The extensional modes are well studied [52, 116, 125] and consist of an expansion along the length of the line. In contrast, the breathing modes consist in an expansion along the short side of the line. We show a schematic representation of the two modes in Fig. 6.13.

We can get some idea of the frequency of these modes by looking at the well-known modes of *cylindrical* metal bars. It is important to realise that the model described in [129] refers to gold cylindrical nanorods in solution. In our case, the gold lines are rectangular and attached to a substrate. These differences may significantly change the nature and the period of the breathing modes. The periods of the extensional and breathing modes are given by the following formulas [129]:

$$T_{ext} = \frac{2L}{(2n+1)\sqrt{E/\rho}}, \tag{6.6}$$

$$T_{br} = \frac{2\pi R}{\psi v_l}. \tag{6.7}$$

Here, $L$ is the length of the line, $E$ is the Young's modulus of Au, which describes the stiffness of a solid material [130]. $\rho$ is the density of the material and $R$ is the radius of the cylinder. $\psi$ depends on the Poisson ratio for Au, which is the ratio between the axial and the lateral strain at

the same point in the material [130]. $v_l$ is the longitudinal speed of sound in the metal. Now, knowing that the length of our grating lines is $L \approx 2$

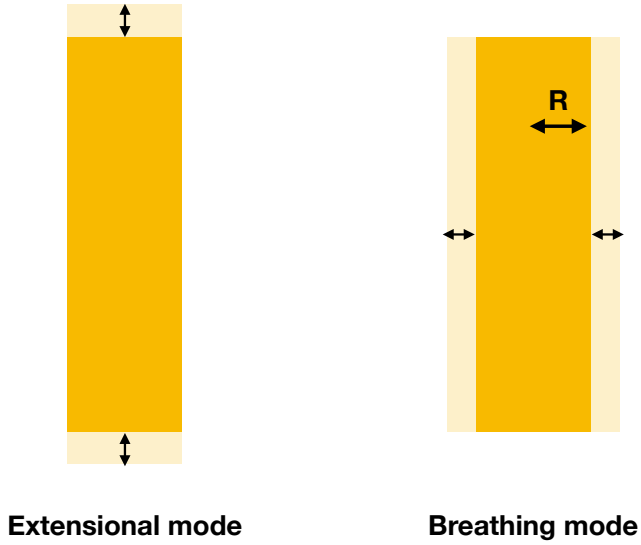


Figure 6.13: Schematic representation of the extensional and breathing modes of a grating line.

mm, by inserting the Au constants' values in Eq. 6.6, we get a period of $T_{ext} \approx 3.2\,\mu s$. This period is too long to be detected on the time scale of our experiments ($\approx 1$ ns).

As for the "breathing" mode, considering a linewidth of $l = DC \times D \approx 312.4$ nm, where $DC$ is the duty cycle of the grating expressed as a ratio and $D$ is the period of the grating, we can calculate a period $T_{br} \approx 143.3$ ps by using Eq. 6.7. The calculated value is in good agreement with the oscillation frequency at 6.9 GHz present in all our measurements, which corresponds to a period of $T = 148$ ps. However, this agreement might be fortuitous due to the obvious differences between cylinders and rectangular bars.

Nonetheless, some support for the interpretation of the oscillation as a quasi-normal mode is given in [125], where they show that for Au bars on

top of a fused quartz substrate, the normal mode for a 40 nm amplitude, 400 nm period grating should oscillate with a frequency of 7.8 GHz. In our case, if we extrapolate from their data to a grating amplitude of 47 nm, we find an normal mode frequency of 7.1 GHz. This is close to the measured frequency (6.9 GHz) of our normal mode. However, in our case the substrate is the same material as the grating lines and so again, care should be taken not to over-interpret the agreement.

**Longitudinal waves**

As we already explained in Chapter 5, Au has a relatively small electron-phonon coupling constant [59, 94]. In Au, the electron gas energy rapidly diffuses deeper into the metal before the electron gas has had the time to significantly cool through heating of the lattice. In fact, when a single thin layer (less than 200 nm) of Au is illuminated by an ultrashort pulse, the whole layer is rapidly and more or less homogeneously heated up. Rapid heating of the lattice leads to an oscillatory expansion and contraction of the layer in a direction perpendicular to the surface. Such an expansion/contraction of the lattice can be seen as a standing acoustic wave formed by the addition of two counter propagating acoustic waves, each having a wavelength corresponding to twice the thickness of the layer. Thus, the frequency of these longitudinal oscillations is related to the thickness of the Au layer $d$. We can calculate the period of these oscillations as the ratio between the distance travelled by the acoustic wave and the longitudinal speed of sound in Au, $v_l$:

$$T_l = \frac{2d}{v_l}. \tag{6.8}$$

For Au, $v_l$=3.24 km/s. We can now calculate the oscillation frequency corresponding to the longitudinal echoes for each of the samples discussed in this work. For the 100 nm thick Au layer, we have an oscillation period of $T_l \approx 61.7$ ps, corresponding to an oscillation frequency of 16.2 GHz. These oscillations are not observed in the FFT analysis, as shown in Fig. 6.8(b). We think that this is because the amplitude of this oscillation is too small when compared to the amplitude of the surface wave. In fact, by carefully looking at the curves away from the plasmonic resonance in 6.8(a), such as 630 (cyano curve), 640 (green curve) and 660 (brown curve) nm, the hint

of an oscillation with a period of about 60 ps period is visible in the first 100 ps.

For the 136 nm thick Au layer, we expect an oscillation with a period of $T_l \approx 82.4$ ps, corresponding to an oscillation frequency of 12.1 GHz. This oscillation is present in the FFT analysis, as shown in Fig. 6.10(b).

The same applies for the 177 nm thick Au layer, where an oscillation with a period of $T_l \approx 107.3$ ps is expected. This period corresponds to an oscillation frequency of 9.3 GHz, which we can clearly see in Fig. 6.12(b) for all the wavelengths.

**Other acoustic modes**

By looking at the FFT analysis of the measured signals, it is clear that those signals are composed of more than three oscillations. In fact, aside from the three main peaks described before, a small, low frequency peak is present at $\approx 1.5$ GHz, for all the samples (see Fig.s 6.7(b), 6.9(b) and 6.11(b)). At this time of writing, we have not yet been able to determine if this is a real oscillation or perhaps a numerical artefact. Moreover, this oscillation seems to display a small frequency shift as a function of the wavelength, which we can currently not explain.

Finally, several small peaks are present in the FFT analysis as well. Their origin is currently not understood but they may be related to more complicated acoustic (eigen) modes of the system.

### 6.5.2 Shift in plasmonic resonance due to change in density

From Eq. 6.2, we can rewrite the condition to excite a SPP at the metal/air interface which propagates in the opposite direction to the horizontal component of the wave vector of the incident light as,

$$\lambda = D\left(sin\theta + \sqrt{\frac{\epsilon_1}{\epsilon_1 + 1}}\right), \tag{6.9}$$

where $D$ is the period of the grating, $\theta$ is the angle of incidence, $\epsilon_1$ is the dielectric constant of the metal, $\epsilon_2 = 1$ is the dielectric constant of the air. From the Drude model [69], the real part of the dielectric function, $\epsilon_1(\omega)$, of the free electron gas in a noble metal can be expressed as:

$$\epsilon_1(\omega) = \epsilon_\infty - \frac{\omega_p^2}{\omega^2 + \gamma^2}. \tag{6.10}$$

Table 6.1: Au Optical Constants.

| Constant | Description | Unit | Value |
|---|---|---|---|
| $\epsilon_\infty$ | Contribution to $\epsilon$ by bound electrons | - | $9.84$[132] |
| $\epsilon_0$ | Vacuum permittivity | $\mathrm{Fm}^{-1}$ | $8.85 \times 10^{-12}$ |
| $\gamma$ | Electron collision frequency | eV | $0.072$[132] |
| n | Electron density | $\mathrm{m}^{-3}$ | $5 \times 10^{28}$ |
| e | Electron charge | C | $1.60 \times 10^{-19}$ |
| m | Effective mass | kg | $9.11 \times 10^{-31}$ |

Here $\epsilon_\infty$ is the contribution to the dielectric constant that contains the contribution of the bound electrons [69, 70, 131, 132]. $\gamma$ is the electron collision frequency. It can be written as $\gamma = 1/\tau$, where $\tau$ is the time between collisions of the free electron gas. $\omega_p$ is the so-called *plasma frequency* of the free electrons and is given by

$$\omega_p = \sqrt{\frac{ne^2}{\epsilon_0 m}}, \tag{6.11}$$

where $n$ is the electron gas density, $e$ is the electron charge, $m$ is the effective electron mass, $\epsilon_0$ is the vacuum permittivity.

When an acoustic wave travels through a material, a change in the density of the material is observed. The density change results in a change in the electron density which leads to a change of the dielectric function of the material and a shift of the plasmon resonance wavelength.

We can use the Drude-model to estimate $\epsilon_1$ as a function of electron density $n$ by using 6.10. In fact, using the numerical model described in [92], it is possible to calculate the total expansion of the Au layer when, for example, a longitudinal acoustic wave passes through it. Under these conditions, we can calculate the new electron density $n'$ as $n' = n\frac{d}{d+\Delta d}$. For a Au layer of thickness d = 177 nm a maximum expansion/contraction of the layer $\Delta$d = $\pm$ 250 pm is expected.

We can now calculate $\epsilon_1$ and the changed permittivity $\epsilon_1'$ by using the values for the Au optical constants shown in Tab. 6.1. Then, from Eq. 6.9, the maximum shift in the plasmonic resonance wavelength due to the

acoustic wave can be calculated. We find,

$$\Delta\lambda_{max} = \lambda(n') - \lambda(n) = 0.051\,\text{nm} \;\; \text{(Contraction)},$$

$$\Delta\lambda_{max} = \lambda(n') - \lambda(n) = -0.051\,\text{nm}\,\text{(Expansion)}.$$

In order to achieve the measured reflection change of $\Delta R = 0.5\,\%$, we calculate that a shift in the plasmonic resonance wavelength of approximately 0.059 nm in both directions is needed. This value is in good agreement with the one we derive from Eq. 6.9. This makes it plausible that the reflection changes we observe can be attributed to acoustic-wave-induced electron-density changes that lead to a shift of the SPP resonance.

### 6.5.3 SAW signal enhancement under plasmonic resonance conditions

As we can see in Figs. 6.8(b), 6.10(b) and 6.12(b), the amplitude of the SAW peak is biggest at 650 nm, thus, when the probe is resonant with the plasmonic resonance. To better visualise this behaviour, we analyse one of the three samples where the three oscillations are clearly present, namely the 177 nm thick Au grating. In Fig. 6.14 we plot the amplitude of the FFT peaks as a function of the probe wavelength for the three frequencies. The figure clearly shows how the amplitude of the optical response to the SAW is enhanced under SPP resonance conditions. The optical response to the other two modes, the LW and the NM, is instead suppressed at the plasmonic resonance wavelength. In fact, at this wavelength the signals change sign which means that, at the resonance, the magnitude becomes very small. On the other hand, the LW and the NM show an enhancement on the wings of the plasmonic curve. A similar behaviour has been observed in the past. In [108], Chen et al. performed an angle-dependent study around the plasmon resonance angle on a thin Bismuth layer in the Kretschmann geometry. They also found that the longitudinal acoustic echoes are strongest in the wings of the plasmon resonance.

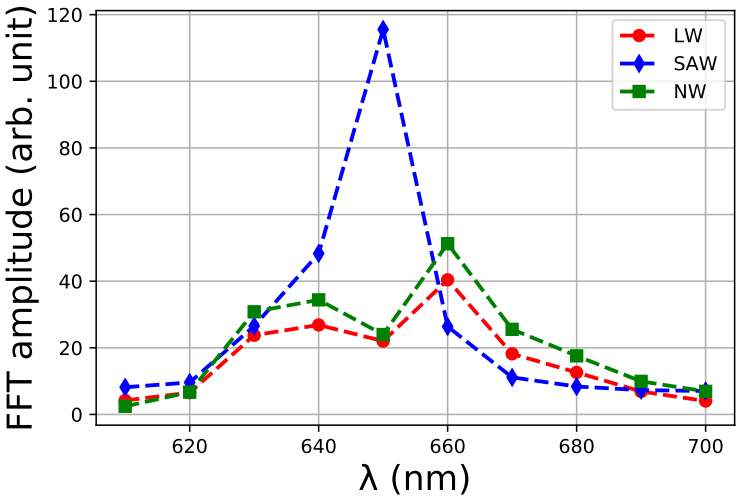


Figure 6.14: Amplitude of the main FFT peaks (2.8, 6.9 and 9.3 GHz) as a function of the probe wavelength for the 177 nm thick Au grating.

### 6.5.4 Phase shift

In Fig. 6.15 we plot the phase of the SAW, the NM and the LW signals measured for the 177 nm thick grating as a function of the probe wavelength.

We observe a phase difference of approximately $\pi$ for both the LW and the NM on opposite sides of the longitudinal plasmon band. This agrees with the assumption that the signal arises from a time-dependent, oscillatory shift in the position of the plasmon band [129]. As we have shown in Section 6.5.2, the electron density changes due to the acoustic waves in the metal grating. This change in electron density results in a change of the plasma frequency and, thus, of the dielectric function and, ultimately, a reflection change that is positive or negative depending on whether the probe wavelength is above or below the SPP resonance. For the SAW, the phase of the measured photoacoustic signals shows a more complicated behaviour as a function of the probe wavelength. This behaviour is currently not understood.

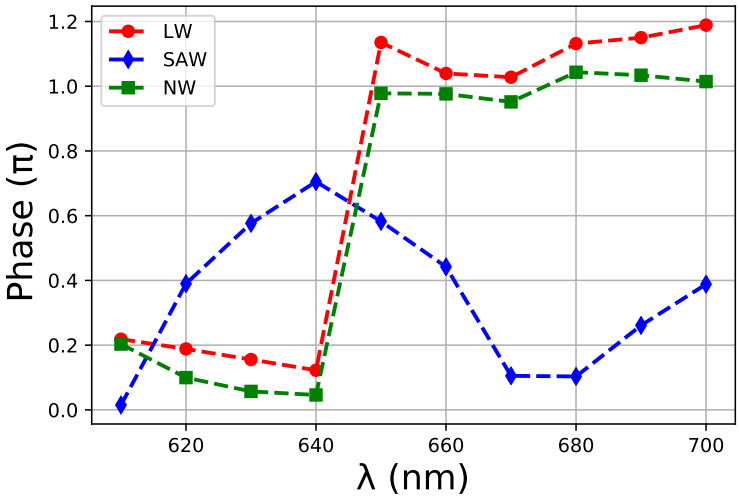


Figure 6.15: Phase of the SAW, the NM and the LW generated onto and into the 177 nm thick grating as a function of the probe wavelength.

## 6.6 Summary

We have shown how a SPP resonance can be used to enhance the strength of photoacoustic signals. In our experiments, a SAW, NM and LW were excited simultaneously in a plasmonic Au grating. As a consequence, density variations caused by the acoustic waves lead to an electron density change which can shift the SPP resonance of the grating. We see that the amplitude of the optical response to the SAW reaches a maximum at the SSP resonance wavelength. At this wavelength the optical response to the NM and LW shows a minimum instead but its amplitude is higher at the wings of the plasmonic curve, where the reflection changes the most. Although the results are interesting, it is clear that more work must be done on the interpretation of the data. For example, the current interpretation of the measured shift of the plasmonic resonance is based on the assumption that this is caused by changes in the electron density. However, acoustic wave-induced changes in the dimensions of the grating (e.g., a change in grating line width) as a mechanism for the shift of the SPP resonance cannot be ruled out. This should be a topic for further studies. Nevertheless, we were able to detect photoacoustic signals via reflection changes on the or-

der of $10^{-2}$. In addition, our technique may be used to suppress one of the other modes by choosing the right wavelength. We believe that this technique may be used to enhance the detection sensitivity in photo-acoustics experiments.

# Bibliography


[1] G. E. Moore, "Cramming more components onto integrated circuits, Reprinted from Electronics, volume 38, number 8, April 19, 1965," *IEEE Solid-State Circuits Society Newsletter* **11** (2006) 33–35.

[2] G. E. Moore, "Progress in digital integrated electronics," *IEEE Solid-State Circuits Society Newsletter* **11** (2006) 36–37.

[3] Wikipedia contributors, "Transistor count — Wikipedia, The Free Encyclopedia." `https://en.wikipedia.org/w/index.php?title=Transistor_count&oldid=902539140`, 2019. [Online; accessed 19-June-2019].

[4] H. J. Levinson, *Principles of lithography*. SPIE, Bellingham, WA, 2005.

[5] P. Naulleau, "2.17 - Optical Lithography," in *Comprehensive Nanoscience and Nanotechnology (Second Edition)*, D. L. Andrews, R. H. Lipson, and T. Nann, eds., pp. 387 – 398. Academic Press, Oxford, second edition ed., 2019.

[6] K. B. Gylfason, A. C. Fischer, B. Gunnar Malm, H. H. Radamson, L. M. Belova, and F. Niklaus, "Process considerations for layer-by-layer 3D patterning of silicon, using ion implantation, silicon deposition, and selective silicon etching," *Journal of Vacuum Science & Technology B* **30** (2012) 06FF05.

[7] A. J. M. Mackus, A. A. Bol, and W. M. M. Kessels, "The use of atomic layer deposition in advanced nanopatterning," *Nanoscale* **6** (2014) 10941–10960.

[8] N.-T. Nguyen, "Chapter 4 - Fabrication technologies," in *Micromixers (Second Edition)*, pp. 113 – 161. William Andrew Publishing, Oxford, second edition ed., 2012.

[9] C. A. Mack, *Fundamental Principles of Optical Lithography.* Wiley, 2007.

[10] G. R. Fowles, *Introduction to Modern Optics.* Dover Publications, Inc., New York, 1989.

[11] M. Dusa, B. Arnold, J. Finders, H. Meiling, K. van Ingen Schenau, and A. C. Chen, "The lithography technology for the 32 nm HP and beyond,".

[12] K. Ronse, "Optical lithography—a historical perspective," *Comptes Rendus Physique* **7** (2006) 844 – 857.

[13] P. A. Zimmerman, B. J. Rice, E. C. Piscani, and V. Liberman, "High index 193 nm immersion lithography: the beginning or the end of the road," *Optical Microlithography XXII. Ed. Harry J. Levinson & Mircea V. Dusa. San Jose, CA, USA: SPIE* (2009) .

[14] A. B. F. C. Bruce W. Smith, Hoyoung Kang and Y. Fan, "Water immersion optical lithography for the 45-nm node," *Proc. SPIE* **5040** (2003) .

[15] C. Wagner and N. Harned, "Lithography gets extreme," *Nature Photonics* **4** (2010) 24.

[16] V. Y. Banine, K. N. Koshelev, and G. H. P. M. Swinkels, "Physical processes in EUV sources for microlithography," *Journal of Physics D: Applied Physics* **44** (2011) 253001.

[17] T. W. Barbee, S. Mrowka, and M. C. Hettrick, "Molybdenum-silicon multilayer mirrors for the extreme ultraviolet," *Appl. Opt.* **24** no. 6, (1985) 883–886.

[18] J. Chen, *Characterization of EUV induced contamination on multilayer optics.* PhD thesis, University of Twente, 2011.

[19] S. Keij, I. Setija, G. van der Zouw, and E. Ebert, "Advances in phase-grating-based wafer alignment systems," *Proc. SPIE* **5752** (2005) .

[20] B. Jacobs and P. Kramer, "Apparatus for aligning a mask with respect to a semiconductor substrate," 1974. US Patent 3, 811, 779.

[21] A. J. den Boef, "Optical wafer metrology sensors for process-robust CD and overlay control in semiconductor device manufacturing," *Surface Topography: Metrology and Properties* **4** (2016) .

[22] M. M. Waldrop, "The chips are down for Moore's law," *Nature* **530** (2016) .

[23] O. Matsuda, M. C. Larciprete, R. Li Voti, and O. B. Wright, "Fundamentals of picosecond laser ultrasonics," *Ultrasonics* **56** (2015) 3–20.

[24] M. Kouyaté, T. Pezeril, V. Gusev, and O. Matsuda, "Theory for optical detection of picosecond shear acoustic gratings," *J. Opt. Soc. Am. B* **33** no. 12, (Dec, 2016) 2634–2648.

[25] P. Ruello and V. E. Gusev, "Physical mechanisms of coherent acoustic phonons generation by ultrafast laser action," *Ultrasonics* **56** (2015) 21 – 35.

[26] K. A. Nelson, R. J. D. Miller, D. R. Lutz, and M. D. Fayer, "Optical generation of tunable ultrasonic waves," *Journal of Applied Physics* **53** (1982) 1144–1149.

[27] C. Thomsen, H. T. Grahn, H. J. Maris, and J. Tauc, "Surface generation and detection of phonons by picosecond light pulses," *Phys. Rev. B* **34** (1986) 4129–4138.

[28] O. B. Wright and K. Kawashima, "Coherent phonon detection from ultrafast surface vibrations," *Phys. Rev. Lett.* **69** (1992) 1668–1671.

[29] V. Gusev, "On generation of picosecond inhomogeneous shear strain fronts by laser-induced gratings," *Applied Physics Letters* **94** no. 16, (2009) 164105.

[30] O. B. Wright and V. E. Gusev, "Acoustic generation in crystalline silicon with femtosecond optical pulses," *Applied Physics Letters* **66** (1995) 1190–1192.

[31] H. Maris, "Picosecond Ultrasonics," *Scientific American* **278** (1998) .

[32] T. F. Crimmins, A. A. Maznev, and K. A. Nelson, "Transient grating measurements of picosecond acoustic pulses in metal films," *Appl. Phys. Lett.* **74** (1999) 1344–1346.

[33] R. M. Slayton and K. A. Nelson, "Picosecond acoustic transmission measurements. Part I. Transient grating generation and detection of acoustic responses in thin metal films," *Journal of Chemical Physics* **120** no. 8, (2004) 3908–3918.

[34] A. Huynh, N. D. Lanzillotti-Kimura, B. Jusserand, B. Perrin, A. Fainstein, M. F. Pascual-Winter, E. Peronne, and A. Lemaître, "Subterahertz Phonon Dynamics in Acoustic Nanocavities," *Phys. Rev. Lett.* **97** (2006) 115502.

[35] T. Saito, O. Matsuda, and O. B. Wright, "Picosecond acoustic phonon pulse generation in nickel and chromium," *Phys. Rev. B* **67** (2003) 205421.

[36] F. Pérez-Cota, R. J. Smith, E. Moradi, L. Marques, K. F. Webb, and M. Clark, "High resolution 3D imaging of living cells with sub-optical wavelength phonons," *Scientific reports* **6** (December, 2016) 39326.

[37] B. C. Daly, N. C. R. Holme, T. Buma, C. Branciard, T. B. Norris, D. M. Tennant, J. A. Taylor, J. E. Bower, and S. Pau, "Imaging nanostructures with coherent phonon pulses," *Applied Physics Letters* **84** no. 25, (2004) 5180–5182.

[38] T. Saito, O. Matsuda, M. Tomoda, and O. B. Wright, "Imaging gigahertz surface acoustic waves through the photoelastic effect," *J. Opt. Soc. Am. B* **27** (2010) 2632–2638.

[39] T. W. Murray, M. Haltmeier, T. Berer, E. Leiss-Holzinger, and P. Burgholzer, "Super-resolution photoacoustic microscopy using blind structured illumination," *Optica* **4** no. 1, (Jan, 2017) 17–22.

[40] C. J. K. Richardson, M. J. Ehrlich, and J. W. Wagner, "Interferometric detection of ultrafast thermoelastic transients in thin films:theory with supporting experiment," *J. Opt. Soc. Am. B* **16** no. 6, (1999) 1007–1015.

[41] M. Lejman, V. Shalagatskyi, O. Kovalenko, T. Pezeril, V. V. Temnov, and P. Ruello, "Ultrafast optical detection of coherent acoustic phonons emission driven by superdiffusive hot electrons," *J. Opt. Soc. Am. B* **31** (2014) 282–290.

[42] Z. Ge, D. G. Cahill, and P. V. Braun, "AuPd Metal Nanoparticles as Probes of Nanoscale Thermal Transport in Aqueous Solution," *The Journal of Physical Chemistry B* **108** no. 49, (2004) 18870–18875.

[43] A. A. Maznev, K. A. Nelson, and J. A. Rogers, "Optical heterodyne detection of laser-induced gratings," *Opt. Lett.* **23** no. 16, (Aug, 1998) 1319–1321.

[44] V. E. Gusev and P. Ruello, "Advances in applications of time-domain Brillouin scattering for nanoscale imaging," *Applied Physics Reviews* **5** (2018) 031101.

[45] W. S. Fann, R. Storz, H. W. K. Tom, and J. Bokor, "Direct measurement of nonequilibrium electron-energy distributions in subpicosecond laser-heated gold films," *Phys. Rev. Lett.* **68** (May, 1992) 2834–2837.

[46] W. S. Fann, R. Storz, H. W. K. Tom, and J. Bokor, "Electron thermalization in gold," *Phys. Rev. B* **46** (Nov, 1992) 13592–13595.

[47] J. L. Hostetler, A. N. Smith, D. M. Czajkowsky, and P. M. Norris, "Measurement of the electron-phonon coupling factor dependence on film thickness and grain size in Au, Cr, and Al," *Appl. Opt.* **38** no. 16, (Jun, 1999) 3614–3620.

[48] A. N. Smith and P. M. Norris, "Influence of intraband transitions on the electron thermoreflectance response of metals," *Applied Physics Letters* **78** no. 9, (2001) 1240–1242.

[49] P. E. Hopkins and P. M. Norris, "Substrate influence in electron-phonon coupling measurements in thin Au films," *Applied Surface Science* **253** no. 15, (2007) 6289 – 6294.

[50] A. Chen, L. Sui, Y. Shi, Y. Jiang, D. Yang, H. Liu, M. Jin, and D. Ding, "Ultrafast investigation of electron dynamics in the gold-coated two-layer metal films," *Thin Solid Films* **529** (2013) 209 – 216.

[51] C. Grünsteidl, T. Berer, M. Hettich, and I. Veres, "Using zero-group-velocity lamb waves to determine thickness and bulk sound velocities of isotropic plates," *AIP Conference Proceedings* **2102** no. 1, (2019) 050016.

[52] B. Bonello, B. Perrin, E. Romatet, and J. Jeannet, "Application of the picosecond ultrasonic technique to the study of elastic and time-resolved thermal properties of materials," *Ultrasonics* **35** no. 3, (1997) 223 – 231.

[53] O. B. Wright, "Ultrafast nonequilibrium stress generation in gold and silver," *Phys. Rev. B* **49** (Apr, 1994) 9985–9988.

[54] D. Yarotski, E. Fu, L. Yan, Q. Jia, Y. Wang, A. J. Taylor, and B. P. Uberuaga, "Characterization of irradiation damage distribution near TiO2/SrTiO3 interfaces using coherent acoustic phonon interferometry," *Applied Physics Letters* **100** no. 25, (2012) 251603.

[55] C. Klieber, E. Peronne, K. Katayama, J. Choi, M. Yamaguchi, T. Pezeril, and K. A. Nelson, "Narrow-band acoustic attenuation measurements in vitreous silica at frequencies between 20 and 400 GHz," *Applied Physics Letters* **98** (2011) 211908.

[56] C. Suárez, W. E. Bron, and T. Juhasz, "Dynamics and Transport of Electronic Carriers in Thin Gold Films," *Phys. Rev. Lett.* **75** (1995) 4536–4539.

[57] M. Bonn, D. N. Denzler, S. Funk, M. Wolf, S.-S. Wellershoff, and J. Hohlfeld, "Ultrafast electron dynamics at metal surfaces: Competition between electron-phonon coupling and hot-electron transport," *Phys. Rev. B* **61** (2000) 1101–1105.

[58] S. Anisimov, B. Kapeliovich, and T. Perel'man, "Electron emission from metal surfaces exposed to ultrashort laser pulses," *Sov. Phys. JETP* **39** (1974) 375–377.

[59] J. Hohlfeld, S.-S. Wellershoff, J. Güdde, U. Conrad, V. Jähnke, and E. Matthias, "Electron and lattice dynamics following optical excitation of metals," *Chemical Physics* **251** no. 1, (2000) 237 – 258.

[60] J. Hohlfeld, J. Müller, S.-S. Wellershoff, and E. Matthias, "Time-resolved thermoreflectivity of thin gold films and its dependence on film thickness," *Applied Physics B* **64** no. 3, (1997) 387–390.

[61] P. J. S. van Capel and J. I. Dijkhuis, "Time-resolved interferometric detection of ultrashort strain solitons in sapphire," *Phys. Rev. B* **81** (2010) 144106.

[62] A. Devos and C. Lerouge, "Evidence of Laser-Wavelength Effect in Picosecond Ultrasonics: Possible Connection With Interband Transitions," *Phys. Rev. Lett.* **86** (Mar, 2001) 2669–2672.

[63] O. Matsuda, M. Tomoda, T. Tachizaki, S. Koiwa, A. Ono, K. Aoki, R. P. Beardsley, and O. B. Wright, "Ultrafast ellipsometric interferometry for direct detection of coherent phonon strain pulse profiles," *J. Opt. Soc. Am. B* **30** (Jul, 2013) 1911–1921.

[64] J. W. Goodman, "Fresnel and Fraunhofer Diffraction," in *Introduction to Fourier Optics, Third Edition*. Roberts & Company Publishers, 2005.

[65] D. R. Lide, *Handbook of Chemistry and Physics, 84th Edition*. CRC Press, LLC, 2003.

[66] Y.-C. Chang, P. Zhou, and J. H. Burge, "Analysis of phase sensitivity for binary computer-generated holograms," *Appl. Opt.* **45** no. 18, (2006) 4223–4234.

[67] P. Drude, "Zur Elektronentheorie der Metalle," *Annalen der Physik* **306** (1900) 566–613.

[68] H. Raether in *Surface Plasmons on Smooth and Rough Surfaces and on Gratings*. Springer-Verlag Berlin Heidelberg, 1988.

[69] S. A. Maier, "Plasmonics: Fundamentals and Applications," Springer US, 2007.

[70] L. Novotny and B. Hecht, "Principles of Nano-Optics," Cambridge University Press, 2012.

[71] A. Otto, "Excitation of nonradiative surface plasma waves in silver by the method of frustrated total reflection," *Z. Physik* **216** (1968) 398–410.

[72] E. Kretschmann and H. Raether, "Radiative Decay of Nonradiative Surface Plasmons Excited by Light," *Zeitschrift für Naturforschung A* **23** (1968) 2135–2136.

[73] G. H. Welsh, N. T. Hunt, and K. Wynne, "Terahertz-Pulse Emission Through Laser Excitation of Surface Plasmons in a Metal Grating," *Phys. Rev. Lett.* **98** (Jan, 2007) 026803.

[74] G. Ruffato, G. Zacco, and F. Romanato, "Innovative Exploitation of Grating-Coupled Surface Plasmon Resonance for Sensing," in *Plasmonics Principles and Applications*. IntechOpen, 2012.

[75] V. Verrina, S. Edward, H. Zhang, A. Antoncecchi, S. Witte, and P. Planken, "Role of scattering by surface roughness in the photoacoustic detectionof hidden micro-structures," *Appl. Opt.* **59** no. 30, (Oct, 2020) 9499–9509.

[76] V. Verrina, S. Edward, H. Zhang, S. Witte, and P. C. M. Planken, "Photoacoustic detection of low duty cycle gratings through optically opaque layers," *Applied Physics Letters* **117** no. 5, (2020) 051104.

[77] B. A. Movchan, "Inorganic materials and coatings produced by EBPVD," *Surface Engineering* **22** (2006) 35–46.

[78] B. J. Griffin, "A comparison of conventional Everhart-Thornley style and in-lens secondary electron detectors—a further variable in scanning electron microscopy," *Scanning* **33** (2011) 162–173.

[79] B. Cappella and G. Dietler, "Force-distance curves by atomic force microscopy," *Surface Science Reports* **34** (1999) 1 – 104.

[80] V. Gusev, "Generation of inhomogeneous bulk plane acoustic modes by laser-induced thermoelastic grating near mechanically free surface," *Journal of Applied Physics* **107** no. 11, (2010) 114906.

[81] A. Devos, "Colored ultrafast acoustics: From fundamentals to applications," *Ultrasonics* **56** (2015) 90 – 97.

[82] P. van Capel, E. Péronne, and J. Dijkhuis, "Nonlinear ultrafast acoustics at the nanoscale," *Ultrasonics* **56** (2015) 36 – 51.

[83] T. Pezeril, P. Ruello, S. Gougeon, N. Chigarev, D. Mounier, J.-M. Breteau, P. Picart, and V. Gusev, "Generation and detection of plane coherent shear picosecond acoustic pulses by lasers: Experiment and theory," *Phys. Rev. B* **75** (May, 2007) 174307.

[84] S. Edward, H. Zhang, I. Setija, V. Verrina, A. Antoncecchi, S. Witte, and P. Planken, "Detection of Hidden Gratings through Multilayer Nanostructures Using Light and Sound," *Phys. Rev. Applied* **14** (Jul, 2020) 014015.

[85] S. Edward, A. Antoncecchi, H. Zhang, H. Sielcken, S. Witte, and P. C. M. Planken, "Detection of periodic structures through opaque metal layers by optical measurements of ultrafast electron dynamics," *Opt. Express* **26** no. 18, (2018) 23380–23396.

[86] X. Yu, Y. Shi, T. Wang, and X. Sun, "Dust-concentration measurement based on Mie scattering of a laser beam," *Plos One* **12** no. 8, (08, 2017) 1–15.

[87] S. O. Rice, "Reflection of electromagnetic waves from slightly rough surfaces," *Communications on Pure and Applied Mathematics* **4** no. 2â3, (1951) 351–378.

[88] T. V. Vorburger, E. Marx, and T. R. Lettieri, "Regimes of surface roughness measurable with light scattering," *Appl. Opt.* **32** no. 19, (Jul, 1993) 3401–3408.

[89] S. Schröder, A. Duparré, L. Coriand, A. Tünnermann, D. H. Penalver, and J. E. Harvey, "Modeling of light scattering in different regimes of surface roughness," *Opt. Express* **19** no. 10, (May, 2011) 9820–9835.

[90] T. D. B. Jacobs, T. Junge, and L. Pastewka, "Quantitative characterization of surface topography using spectral analysis," *Surface Topography: Metrology and Properties* **5** no. 1, (Jan, 2017) 013001.

[91] P. Benjamin and C. Weaver, "The Adhesion of Evaporated Metal Films on Glass," *Proceedings of the Royal Society of London. Series A, Mathematical and Physical Sciences* **261** no. 1307, (1961) 516–531.

[92] H. Zhang, A. Antoncecchi, S. Edward, I. Setija, P. Planken, and S. Witte, "Unraveling Phononic, Optoacoustic, and Mechanical Properties of Metals with Light-Driven Hypersound," *Phys. Rev. Applied* **13** (2020) 014010.

[93] A. Devos, R. Côte, G. Caruyer, and A. Lefèvre, "A different way of performing picosecond ultrasonic measurements in thin transparent films based on laser-wavelength effects," *Applied Physics Letters* **86** (2005) 211903.

[94] S.-S. Wellershoff, J. Güdde, J. Hohlfeld, J. Muller, and E. Matthias, "Role of electron-phonon coupling in femtosecond laser damage of metals," *Proc. SPIE* **3343** (1998) .

[95] H. N. Lin, R. J. Stoner, H. J. Maris, and J. Tauc, "Phonon attenuation and velocity measurements in transparent materials by

picosecond acoustic interferometry," *Journal of Applied Physics* **69** (1991) 3816–3822.

[96] H. Lin, H. J. Maris, L. B. Freund, K. Y. Lee, H. Luhn, and D. P. Kern, "Study of vibrational modes of gold nanostructures by picosecond ultrasonics," *Journal of Applied Physics* **73** no. 1, (1993) 37–45.

[97] O. Matsuda, T. Pezeril, I. Chaban, K. Fujita, and V. Gusev, "Time-domain Brillouin scattering assisted by diffraction gratings," *Phys. Rev. B* **97** (Feb, 2018) 064301.

[98] G. G. Kozlov, V. S. Zapasskii, and P. Y. Shapochkin, "Heterodyne detection of scattered light: application to mapping and tomography of optically inhomogeneous media," *Appl. Opt.* **57** no. 7, (Mar, 2018) B170–B178.

[99] P. Barna and G. Radnóczi, "Structure formation during deposition of polycrystalline metallic thin films," in *Metallic Films for Electronic, Optical and Magnetic Applications*, K. Barmak and K. Coffey, eds. Woodhead Publishing, 2014.

[100] J. A. DeSanto, *Overview of Rough Surface Scattering*. Springer US, Boston, MA, 2007.

[101] J. Güdde, J. Hohlfeld, J. Müller, and E. Matthias, "Damage threshold dependence on electron–phonon coupling in Au and Ni films," *Applied Surface Science* .

[102] D. Colton and R. Kress, *Inverse Acoustic and Electromagnetic Scattering Theory*. Springer-Verlag, New York, 2013.

[103] C. Thomsen, H. T. Grahn, H. J. Maris, and J. Tauc, "Surface generation and detection of phonons by picosecond light pulses," *Phys. Rev. B* **34** (1986) 4129–4138.

[104] R. I. Tobey, M. E. Siemens, M. M. Murnane, H. C. Kapteyn, D. H. Torchinsky, and K. A. Nelson, "Transient grating measurement of surface acoustic waves in thin metal films with extreme ultraviolet radiation," *Applied Physics Letters* **89** no. 9, (2006) 091108.

[105] V. V. Temnov, "Ultrafast acousto-magneto-plasmonics," *Nature Photonics* **6** no. 11, (2012) 728–736.

[106] L. E. Kreilkamp, I. A. Akimov, V. I. Belotelov, B. A. Glavin, L. V. Litvin, A. Rudzinski, M. Kahl, R. Jede, M. Wiater, T. Wojtowicz, G. Karczewski, D. R. Yakovlev, and M. Bayer, "Terahertz dynamics of lattice vibrations in Au/CdTe plasmonic crystals: Photoinduced segregation of Te and enhancement of optical response," *Phys. Rev. B* **93** (Mar, 2016) 125404.

[107] I. Katayama, S. Koga, K.-i. Shudo, J. Takeda, T. Shimada, A. Kubo, S. Hishita, D. Fujita, and M. Kitajima, "Ultrafast Dynamics of Surface-Enhanced Raman Scattering Due to Au Nanostructures," *Nano Letters* **11** no. 7, (07, 2011) 2648–2654.

[108] Z. Chen and M. F. DeCamp, "Measuring optical phonon dynamics in a bismuth thin film through a surface plasmon resonance," *Journal of Applied Physics* **112** no. 1, (2012) 013527.

[109] J. Wang, J. Wu, and C. Guo, "Resolving dynamics of acoustic phonons by surface plasmons," *Opt. Lett.* **32** no. 6, (Mar, 2007) 719–721.

[110] J. Wang and C. Guo, "Effect of electron heating on femtosecond laser-induced coherent acoustic phonons in noble metals," *Phys. Rev. B* **75** (May, 2007) 184304.

[111] G. V. Hartland, "Coherent vibrational motion in metal particles: Determination of the vibrational amplitude and excitation mechanism," *The Journal of Chemical Physics* **116** no. 18, (2002) 8048–8055.

[112] G. V. Hartland, "Coherent excitation of vibrational modes in metallic nanoparticles," *Annual Review of Physical Chemistry* **57** no. 1, (2006) 403–430.

[113] J. H. Hodak, I. Martini, and G. V. Hartland, "Observation of acoustic quantum beats in nanometer sized Au particles," *The Journal of Chemical Physics* **108** no. 22, (1998) 9210–9213.

[114] J. H. Hodak, A. Henglein, and G. V. Hartland, "Size dependent properties of Au particles: Coherent excitation and dephasing of acoustic vibrational modes," *The Journal of Chemical Physics* **111** no. 18, (1999) 8613–8621.

[115] N. Khokhlov, G. Knyazev, B. Glavin, Y. Shtykov, O. Romanov, and V. Belotelov, "Interaction of surface plasmon polaritons and acoustic waves inside an acoustic cavity," *Opt. Lett.* **42** no. 18, (Sep, 2017) 3558–3561.

[116] B. Bonello, A. Ajinou, V. Richard, and S. M. Che, "Surface acoustic waves in the GHz range generated by periodically patterned metallic stripes illuminated by an ultrashort laser pulse," *Acoustical Society of America* **110** no. October, (2001) 1943–1949.

[117] R. I. Tobey, E. H. Gershgoren, M. E. Siemens, M. M. Murnane, H. C. Kapteyn, T. Feurer, and K. A. Nelson, "Nanoscale photothermal and photoacoustic transients probedwith extreme ultraviolet radiation," *Applied Physics Letters* **85** no. 4, (2004) 564–566.

[118] D. H. Hurley and K. L. Telschow, "Picosecond surface acoustic waves using a suboptical wavelength absorption grating," *Phys. Rev. B* **66** (Oct, 2002) 153301.

[119] Q. Li, K. Hoogeboom-Pot, D. Nardi, M. M. Murnane, H. C. Kapteyn, M. E. Siemens, E. H. Anderson, O. Hellwig, E. Dobisz, B. Gurney, R. Yang, and K. A. Nelson, "Generation and control of ultrashort-wavelength two-dimensional surface acoustic waves at nanoscale interfaces," *Phys. Rev. B* **85** (May, 2012) 195431.

[120] J. J. Kasinski, L. Gomez-Jahn, K. J. Leong, S. M. Gracewski, and R. J. D. Miller, "Optical generation of coherent surface acoustics: an optically based probe of surface structure and dynamics," *Opt. Lett.* **13** no. 9, (Sep, 1988) 710–712.

[121] D. Nardi, M. Travagliati, M. E. Siemens, Q. Li, M. M. Murnane, H. C. Kapteyn, G. Ferrini, F. Parmigiani, and F. Banfi, "Probing Thermomechanics at the Nanoscale: Impulsively Excited

Pseudosurface Acoustic Waves in Hypersonic Phononic Crystals," *Nano Letters* **11** no. 10, (2011) 4126–4133.

[122] C. Rossignol, J. M. Rampnoux, M. Perton, B. Audoin, and S. Dilhaire, "Generation and Detection of Shear Acoustic Waves in Metal Submicrometric Films with Ultrashort Laser Pulses," *Phys. Rev. Lett.* **94** (Apr, 2005) 166106.

[123] Q. Li, K. Hoogeboom-Pot, D. Nardi, M. M. Murnane, H. C. Kapteyn, M. E. Siemens, E. H. Anderson, O. Hellwig, E. Dobisz, B. Gurney, R. Yang, and K. A. Nelson, "Generation and control of ultrashort-wavelength two-dimensional surface acoustic waves at nanoscale interfaces," *Phys. Rev. B* **85** (May, 2012) 195431.

[124] D. H. Hurley, R. Lewis, O. B. Wright, and O. Matsuda, "Coherent control of gigahertz surface acoustic and bulk phonons using ultrafast optical pulses," *Applied Physics Letters* **93** no. 11, (2008) 113101.

[125] H. N. Lin, H. J. Maris, L. B. Freund, K. Y. Lee, H. Luhn, and D. P. Kern, "Study of vibrational modes of gold nanostructures by picosecond ultrasonics," *Journal of Applied Physics* **73** no. 1, (1993) 37–45.

[126] H. K. Bennemann, *Non-linear optics in metals.* Oxford University Press, 1998.

[127] M. R. Cherry, S. Sathish, and R. Grandhi, "A numerical method for predicting Rayleigh surface wave velocity in anisotropic crystals," *Journal of Computational Physics* **351** (2017) 108 – 120.

[128] G. W. Farnell and E. L. Adler, "2 - Elastic Wave Propagation in Thin Layers," vol. 9 of *Physical Acoustics*, pp. 35 – 127. Academic Press, 1972.

[129] M. Hu, X. Wang, G. V. Hartland, P. Mulvaney, J. P. Juste, and J. E. Sader, "Vibrational Response of Nanorods to Ultrafast Laser Induced Heating: Theoretical and Experimental Analysis," *Journal of the American Chemical Society* (2003) 14925–14933.

[130] J. M. Gere and B. J. Goodno, *Mechanics of Materials*. Gengage Learning, 2009.

[131] A. Derkachova and K. Kolwas, "Size dependence of multipolar plasmon resonance frequencies and damping rates in simple metal spherical nanoparticles," *The European Physical Journal Special Topics* **144** no. 1, (May, 2007) 93–99.

[132] A. Derkachova, K. Kolwas, and I. Demchenko, "Dielectric Function for Gold in Plasmonics Applications: Size Dependence of Plasmon Resonance Frequencies and Damping Rates for Nanospheres," *Plasmonics* **11** no. 3, (Jun, 2016) 941–951.

# Summary

## Laser-induced ultrasound for the detection of buried micro- and nano-structures

The biggest challenge for the semiconductor industry nowadays is to reduce the size of the electronic components on a chip, to keep Moore's law going. In order to fabricate as many components as possible on a chip, important technological steps have been made. For example, recently manufactures decided to stack memory cells vertically on top of each other, giving rise to the so called 3D-NAND memory. During the fabrication of a 3D-NAND chip by means of photolithography, wafer alignment makes it often necessary to detect micro- and nano-structures, usually gratings buried underneath many layers. One of the techniques used for probing these structures is to illuminate the gratings with a laser and measure the diffracted beams. By looking at the optical phase-difference between the $+n^{th}$ and $-n^{th}$ (n = 1, 2, 3,...) diffracted beams, it is possible to retrieve the position of the gratings with sub-nanometer accuracy. However, when optically opaque layers cover the grating, light cannot be used to detect the gratings. Fortunately, layers that are opaque to light are often transparent to sound waves.

In this thesis the use of laser-induced ultrasound is described to detect gratings buried underneath optically opaque materials. The experimental setups used are based on a pump-probe scheme. When an opaque material is illuminated at the surface by a femtosecond pump pulse, an acoustic wave is generated that can travel deeper into the material, also through layers

that are opaque to light. When the sound wave reaches the hidden grating, the acoustic wave is reflected back with a wavefront resembling the shape of the hidden grating. When the "acoustic replica" of the grating returns to the surface, it spatially and periodically displaces the atoms or changes the optical properties of the material near the surface. These changes can be detected by a second, delayed probe pulse which is diffracted off the acoustic grating. Thus, the measurement of a diffracted signal indicates the presence of a buried grating.

The results of this work can be divided in two parts, one described in Chapters 4 and 5 and one described in Chapter 6. In Chapter 4, laser-induced ultrasound was used to probe micro-gratings buried underneath metallic layers by using two different laser systems, namely a low-fluence femtosecond laser and a high-fluence femtosecond laser. Buried gratings with 10 nm amplitude and 6 µm period were detected by measuring diffraction from an acoustic replica with an amplitude in the picometer range. We find an important difference between the experiments done in the two different setups. When measuring with the low fluence laser system, we observe that the measured diffracted signal is strongly influenced by the presence of a coherent background optical field generated by random scattering of the probe beam by interface roughness. Added to the weak optical field diffracted by the acoustic replica, the background optical field "amplifies" the originally weak signal, facilitating the detection process. This makes the low fluence laser system a better candidate to be used for detection of hidden structures. In Chapter 5, we analyse the limits of the technique by reducing the size of the grating lines and, thus, the duty cycle of the gratings. The grating line width was reduced by keeping the period and the amplitude of the grating fixed. We find that grating lines as narrow as 75 nm can still be detected by using the low-fluence laser system. In fact, the weak signal diffracted off a low duty cycle acoustic grating can be amplified by the presence of the scattered optical background field mentioned above. Moreover, we find that the background field causes the diffracted signal strength to show a linear dependence on the grating duty cycle rather than the quadratic one expected from literature. In the second part of the thesis, described in Chapter 6, plasmonic gratings were used in the detection of laser-induced acoustic waves. Pump-probe measurements were performed on a plasmonic grating, by tuning the probe wavelength around

the SPP resonance of about 650 nm. It was shown that at least three different acoustic waves were induced simultaneously, namely a surface acoustic wave (SAW), a quasi-normal mode (NM) and longitudinal acoustic waves (LWs). Moreover, an enhancement of the optical response of the grating to acoustic waves was observed for the SAW at the plasmonic resonance. In contrast, the optical response to the other two acoustic modes is lower at the resonance and reaches a maximum on the slopes of the resonance. Thus, it is clear that a plasmonic resonance may be used to enhance the detection of laser-induced acoustic waves.

In summary, this work shows that laser-induced acoustic waves can be used as a non-invasive, non-contact method to detect micro- and nanostructures buried underneath optically opaque materials. We also show that the photoacoustic signal strength, which is usually very small, can be enhanced by either optical scattering by interface roughness, or by employing plasmonic structures.

# Samenvatting

## Laser-geïnduceerd ultrasoon geluid voor detectie van verborgen micro- en nano-structuren

Momenteel is een van de grootste uitdagingen voor de halfgeleiderindustrie het verkleinen van de elektronische componenten op een computer chip, om zo de wet van Moore in stand te houden. Om zoveel mogelijk componenten op een chip te laten passen, zijn er veel belangrijke technologische vorderingen gemaakt. Een van de recente ontwikkelingen is bijvoorbeeld het verticaal stapelen van geheugencellen. Dit heeft geleid tot de zogeheten 3D-NAND geheugenchips. Tijdens de fabricage van een 3D-NAND chip door middel van fotolithografie, maakt waferuitlijning het vaak noodzakelijk om micro- en nanostructuren te kunnen detecteren. Deze structuren zijn meestal tralies en liggen begraven onder meerdere lagen. Een van de technieken om deze structuren waar te nemen, maakt gebruik van belichting van het tralie met een laser, waarna de gediffracteerde bundels gemeten worden. Door te kijken naar het optische fase-verschil tussen de +n-de en -n-de gediffracteerde bundel (n = 1, 2, 3...), is het mogelijk om de positie van het tralie te bepalen met een sub-nanometer nauwkeurigheid. Echter, als optische niet-transparante lagen bovenop het tralie liggen, kan licht niet gebruikt worden om het tralie te detecteren. Desalniettemin zijn lagen die niet transparant zijn voor licht vaak wel transparant voor geluid.

In dit proefschrift wordt het gebruik van laser-geïnduceerd ultrasoon

geluid voor de detectie van optisch verborgen tralies beschreven. De experimentele geometrie die gebruikt wordt om dit voor elkaar te krijgen, is een pomp-probe geometrie. Wanneer een niet-transparant materiaal belicht wordt aan het oppervlak met een femtoseconde pomp-puls, wordt er een akoestische golf gegenereerd die diep in het materiaal kan doordringen. Deze akoestische golf gaat bovendien door de optische niet-transparante lagen heen. Zodra de geluidsgolf het verborgen tralie bereikt, zal de geluidsgolf reflecteren met een golffront dat overeenkomt met de vorm van het verborgen tralie. Wanneer de "akoestische kopie" van het tralie het oppervlak bereikt, zal het ruimtelijk periodiek het oppervlak verplaatsen en/of de optische eigenschappen van het materiaal veranderen in de buurt van het oppervlak. Deze veranderingen kunnen gedecteerd worden door een tweede vertraagde probe-puls die gediffracteerd wordt aan het akoestische tralie. Kortom, het meten van een gediffracteerd signaal geeft de aanwezigheid van een verborgen tralie aan.

De resultaten van het hier gepresenteerde werk kunnen verdeeld worden in twee delen: een deel daarvan is beschreven in hoofdstuk 4 en hoofdstuk 5, en een deel is beschreven in hoofdstuk 6. In hoofdstuk 4 wordt er besproken hoe laser-geïnduceerd ultrasoon geluid gebruikt wordt voor het onderzoeken van micro-tralies verborgen onder metaallagen door middel van twee verschillende lasersystemen. Dit zijn een lage- en een hoge-fluentie femtoseconde laser. Tralies met een amplitude van 10 nm en een periode van 6 µm worden gedetecteerd door het meten van diffractie aan de akoestische kopie van het tralie met een amplitude van tientallen picometers. Er is een belangrijk verschil ontdekt tussen de metingen die gedaan zijn met beide systemen. Wanneer er gemeten wordt met het lage-fluentie lasersysteem, wordt er geobserveerd dat het gemeten gediffracteerde signaal sterk beïnvloed wordt door de aanwezigheid van een coherent optisch achtergrond veld gegenereerd door het willekeurig verstrooien van de probe bundel aan de oppervlakteruwheid. In aanwezigheid van de aan de akoestische kopie gediffracteerde probe bundel zal het optische achtergrondveld het originele zwakke signaal "versterken". Dit faciliteert de detectie hiervan. Hierdoor is het lage-fluentie laser systeem een betere kandidaat voor de detectie van verborgen structuren. In hoofdstuk 5 worden de limieten van deze techniek geanalyzeerd door middel van het verlagen van de dikte van de tralielijnen. Dit verlaagt ook de zogeheten "duty cycle". De tralielijnen zijn dunner ge-

maakt terwijl de periode en de amplitude van de tralie gelijk zijn gebleven. We vonden dat tralielijnen zo dun als 75 nm nog steeds gedetecteerd kunnen worden met behulp van het lage-fluentie systeem. Het zwakke signaal, gediffracteerd aan het lage duty cycle akoestische tralie wordt versterkt door de aanwezigheid van een verstrooid optisch achtergrondveld, zoals hierboven uitgelegd. Bovendien is er gemeten dat het achtergrondveld ervoor zorgt dat de gediffracteerde signaalsterkte een lineair verband laat zien met de tralie duty cycle, in tegenstelling tot het kwadratische verband dat voorspeld wordt in de literatuur. In het tweede deel van het proefschrift, zoals beschreven in hoofdstuk 6, zijn er plasmonische tralies gebruikt voor de detectie van laser-geïnduceerde akoestische golven. Er zijn pomp-probe metingen gedaan aan een plasmonisch tralie, door de probe golflengte te variëren rondom de SPP resonantie bij een golflengte van ongeveer 650 nm. Hier laten we zien dat we tenminste drie akoestische golven tegelijk lanceren, namelijk een akoestische oppervlakte golf (*Surface Acoustic Wave*, SAW), een quasi-normale modus golf (*Quasi-Normal mode*, NM) een een longitudinale akoestische golf (*Longitudinal wave*, LW). Verder is een versterking van de optische respons van het tralie als gevolg van de akoestische golf gemeten voor de SAW op de plasmonische resonantie. De optische respons voor de andere twee akoestische golven is verzwakt op resonantie en bereikt een maximum op de flanken van de resonantie. Het is duidelijk dat een plasmonische resonantie gebruikt kan worden voor het versterken van de detectie van laser-geïnduceerde akoestische golven.

# Acknowledgements

All good things must come to an end...but what a journey it has been! As I look back on the past 5 years I spent in Amsterdam, I only see good memories that will stay with me for a lifelong time. PhD life is never easy, especially when you decide to start from scratch in a new country, being away from home and friends. Soon you have to get to grips with yourself and your limits. But it also gives you the opportunity to grow a lot, meet new people, face different cultures and visit new places.
For all these reasons, it has been a wonderful period of my life and this is mostly thanks to the people I have met on my way.

Paul, this journey started thanks to you. With your joyful and friendly personality, you made me feel welcome in the group since the first day. You were a good supervisor, believing in me even when I did not and helping me finding the motivation when I felt lost. I have always admired your enthusiasm and your willingness to learn. I felt free to walk into your office at any moment to discuss my results, to ask for help, to cry or to burst into cheers when things were finally working. I never felt judged and I have learned a lot from you. I will never forget our long chats during lunch breaks or personal meetings, where we could discuss of anything, from physics to politics, from religion to green energy. For all this, I would like to thank you.
Nishant and Nick, you were the first two people I met when I arrived in AR-CNL and you made me feel part of the group immediately. Nishant, your kindness and your willingness to help were really precious to me. Nick, you are one of the smartest people I have ever met. It was quite easy to become your friend. Thanks for all the dinners at your place!

Stephen, you started your PhD just few months after me. We bonded right away and then we also ended up working on the same project. We spent a lot of time together, both on the optical table (where you helped me a lot!) and outside ARCNL. You were a really good friend, someone I could always count on when I needed. Not a great games player though!
Guido, you were the youngest member of the group, where you brought kindness and cheerfulness. Thank you for "borrowing" me your setup during the last part of my PhD and for translating my Samenvatting, of course. Working together was really funny and super efficient, despite all the Justin Bieber...
Thomas, you helped me a lot with any practical matter while building my setup and during the move. It was always fun to spend time with you, while working or organizing some PV events.

I joined the ARCNL family when it was in its embryonic state and I proudly saw it growing and becoming what it is now. Working here allowed me to closely collaborate and discuss science with many people.
Hao, the numerical model you created was of crucial importance for my work and for better understanding the physics behind my experiments. Thank you for your will to share it with us and for your availability whenever I was asking you to try some crazy ideas for me.
Stefan, you were my co-supervisor and, despite we were in different groups, I always felt we were one. Thank you for your help in writing my manuscripts and for all the insightful inputs.
Irwan, you were my direct scientific ASML contact. When my setup was chosen as the best candidate for subsurface inspection of customers' samples, it was a bit "scary" at the beginning. But thanks to you and your explanations everything went smoothly. It was a pleasure to work with you and to learn to see things from "the other side".
Joost, I would like to thank you for always answering my questions whenever I knocked on your door. Our discussions helped me a lot in better understanding surface physics.
I spent my first PhD year almost entirely in AMOLF, working in the NanoLab and with the FT-IR. I spent a lot of time finding the right recipe for fabricating my samples. This would have been a nightmare without you, Andries, Dimitri and Bob. Thank you for all the trainings, the tips,

the hours you spent with me in cleanroom and to always answering my (sometimes really weird) questions.
I would like to thank also the AMOLF ICT, electronics and software engineering departments for the help and the support provided in these years. In particular, thank you Duncan for building many electronic devices for me. Marco, thank you for creating the software Venus for me. And a general thanks to all the people in the HR, purchase, finance, facilities departments for always helping me when needed.
One of nicest activity I undertook during my period in ARCNL was undoubtedly being part of the PV. It was a pleasure to organize so many social activities for all the ARCNLlers and so satisfying to see you all enjoying our crazy parties and outings. A big thanks to all the PV members that helped me in making all this possible. Thanks to the ARCNL secretarial office for helping in the organization.
Marjan, thank you for giving us this opportunity and for your supervision. But thank you also for helping me with any practical matter and for your kindness and support when I faced some difficulties.
Life in Amsterdam wouldn't have been so great without my friends, many of which I met in or thanks to ARCNL.
Ale, we met for the first time on the cleanroom phone, as we were both spending a lot of time in there. You introduced me to all your AMOLF friends, many of which became my friends too. I will always be grateful to you for facilitating my social life in Amsterdam, which was not an easy task at the beginning. We shared a lot during these years, including the optical setup! We were housemates for 4 years and I really felt home with you. Thank you for always being kind to me, for involving me in your activities, for all the parties and for all the beers :). You are a great friend!
Maisie, my Asian half. Despite women are still a minority in ARCNL, I was so lucky to meet you and to become so close. You thought me that there are no distances, no differences that can stop a friendship to glow! Thank you for being always there when I needed, for you cheerfulness, your intelligence and your funny way to do things. I will miss you a lot.
Randy, my closest Dutch friend. Thank you for showing me your softer side, something you do not do often. Thanks to you and your open mind, I could break down so many prejudices against Dutch culture. And thank you for your persistent will to correct my English pronunciation: not sure

it worked but never give up!
Gorsel, despite you ignored us for the first years (regretting it afterwards), you were a really good friend, someone I could talk to whenever I needed, my cinema guru, a bit sexist but with a big heart. Thank you for your help with the AFM too!
Cristina, quoting Boris: "thank you for being so not Italian". I always appreciated your elegance and kindness and your strength, two sides of the same coin.
I think it is thanks to all my ARCNL colleagues if my time there was so funny and memorable. Victor and our karaokes, Lars "the first" and the balfolk, John and his traps, Fiona and her politeness, Ruben and his composure, Zeudi and her explosiveness.
Reinout and his smile. I will never forget your joyful personality, your pure heart and your love for nature.
But also: Lucas, Tiago, Lars B., Lars L. and Lea, Ale T., Sylvianne, Neha, Zoey, Najmeh, Joris, Amelie, Ivan, Sonia, Jan, Filippo, Marteen, Feng-Chun, Yu and Lianjia. Thank you all for the time we spent together in front of a beer (maybe more), in the park, during PV events or playing board games. It was a lot of fun hanging out with you, guys!
Many of the friends I met in Amsterdam where somehow related to AMOLF.
Lorenzo, I guess we became friends the first time we met on the bus for the AMOLF outing, even if we didn't know yet :) You were always inspiring for me, it was always a pleasure to discuss with you about any topic and also living with you for few months was one of the funniest periods! Moreover, you are yet the only one who have visited me in Calabria...Hope to meet you soon and share many more adventures!
Giulia, I enjoyed a lot the dinners at your place, talking about Italian politics or finding together the best fruit and vegetables supplier during quarantine. And thanks to you I met Giuditta, one of those people that it is always a pleasure to spend time with.
Valeria, my Italian culture soulmate. You were the one I could always count on whenever I wanted to go to theatre, concerts or cinema, talk about books or just walk in the city trying the most delicious restaurants. You were there when I needed, wiping my tears or listening to me and to my complains. I never felt alone with you.
'Mbare Giorgio and Andrea, you were one of the funniest couples and it

was always a pleasure to spend time with you. Looking forward to see you in Sicily!
Carolyn, thank you for making my life in Amsterdam sweeter with all your amazing cakes!
Masha, we spent a lot of time together at home and outside, drinking beer or having interesting conversations about books, movies and series.
Marco, Nicola, Tzeni, Agata, Federica, Andrea C., Mario and Olga, Laura and Moritz: thank you for all the parties and to make my social life in Amsterdam more exciting.

I need to thank my first housemates in Amsterdam too, Filippo in particular, and the help and support they provided when living with the "underground" lady. Thanks to her too to give me some unbelievable stories to tell!

Thanks to Amsterdam and his openness. I have always felt welcome and safe in this city. I have loved her canals, her darkness at night, the green areas, the flowers, the cheese, biking around without problems, the art, the hundreds types of different cultures that live together in such a small part of the world. For all this, thank you. But not for all that rain!

A big thanks to my friends from all over the world: Sofie, Dominik, Sungmin, Fernando and Naima. The love I feel for our 121 crew will never end. You visited me in Amsterdam and we took a lot of trips together during these 5 years. The quality of the time we spent together confirmed every time that true friendship does not know barriers, distances or differences of any kind. Hope we'll meet again soon.

Oltre alle persone incontrate durante questi 5 anni, questo viaggio è stato reso possibile grazie soprattutto agli affetti cardini della mia vita e alle persone che mi hanno fatto appassionare alla fisica. Questo traguardo lo dedico a voi.
Ai miei genitori, Natale e Maria, che hanno sempre appoggiato le mie scelte e sostenuta in ogni modo possibile, devo il ringraziamento più grande. Con il vostro silente orgoglio, mi avete fatto sempre sentire importante e sono sicura questo ennesimo traguardo sia una grande gioia anche per voi. La

lontananza in questi anni è stata dura, lasciare casa ogni volta, tra i pianti e gli abbracci, era sempre come una pugnalata al cuore. Ma il vostro affetto ed i valori trasmessimi sono stati il motore che mi ha sempre permesso di andare avanti.
A mia sorella Jessica, così diversa da me eppure così vicina. La tua tenacia e la tua voglia di fare sono ammirabili. Non smetterò mai di essere al tuo fianco e di aiutarti in ogni cosa tu decida di fare.
Alla mia grande famiglia, gli zii vicini e lontani, i cugini tutti che sono un po' come fratelli e sorelle più grandi. A Leonardo che dice di essere il mio preferito.
A zio Angelo, che ci ha lasciato troppo presto. I mille ricordi insieme a te riempiono il vuoto che hai lasciato nel mio cuore.
A nonna Rosina che non smette mai di mancarmi.

Al Prof. Umeton ed al Prof. De Sio che, fin dalla laurea triennale, mi hanno trasmesso la passione per la fisica dei laser e per la ricerca.
Ai miei ex colleghi ed amici che, nonostante le diverse strade intraprese, mi fanno sentire sempre a casa. A te, Mauro ed alla tua immensa forza.

Agli amici di una vita, Daniele e Savina. Da sempre inseperabili, abbiamo passato insieme i migliori anni della nostra vita e tanti ancora ci aspettano. La lontananza e le assenze non volute non hanno scalfito in nessun modo la nostra amicizia. Voi per me siete casa, famiglia. Avervi avuto ad Amsterdam è stata una delle gioie più grandi. Il vostro sostegno è stato e sarà sempre luce sul mio cammino.
Ad Annalisa, la mia pazzerella amica sin dai tempi del liceo. Alle nostre avventure e alle mille chiacchierate. Alla tua freschezza e purezza d'animo.
A Simone, Sofia, Andrea, Gerry, Luca, Miriam, Francesco, Alberto ed Angela, amici di più "recente data" ma con cui ho trascorso momenti indimenticabili in Calabria ed in giro per l'Europa.

Ad Enrico, Mariella, Gaia e Marta, la mia seconda famiglia. A tutti i momenti trascorsi insieme, ai viaggi indimenticabili ed al supporto ed alla stima sempre mostratimi.
Alla famiglia Trotta-Spadafora tutta, i nonni, gli zii e i cugini e ai tanti momenti di allegra spensieratezza passati insieme.

Ed infine a te, Domenico, che sei la persona più bella che la vita poteva regalarmi. A te che sei il mio compagno, il mio migliore amico, il mio complice in tutto. A te che hai saputo insegnarmi cosa vuol dire amare liberamente e profondamente una persona. A te che sei un vulcano di idee, alla tua energia, alla tua allegria contagiosa ed alla tua pazienza. Ai nostri viaggi in capo al mondo ed ai tanti che dobbiamo ancora intraprendere. Ai 5 anni di distanza che non hanno fatto che rafforzare il nostro rapporto. A Londra e a tutti gli estenuanti viaggi affrontati, ripagati dal sorriso stampato in faccia non appena ci rivedevamo. Alla casa DiVa tanto sognata e ad ogni singolo momento passato insieme. Grazie per aver sempre creduto in me, anche quando io non lo facevo. Grazie per darmi la forza quando sto per arrendermi e per essere d'ispirazione sempre.

"So Long, and Thanks for All the Fish."